THE EFFECTS OF COMPOSITION AND THERMAL PATH ON HOT DUCTILITY OF FORGING STEELS

by

Brendan M. Connolly

BS MSE, University of Pittsburgh, 2006

MS MSE, University of Pittsburgh, 2009

Submitted to the Graduate Faculty of

Swanson School of Engineering in partial fulfillment

of the requirements for the degree of

Doctor of Philosophy

University of Pittsburgh

2016

UNIVERSITY OF PITTSBURGH

SWANSON SCHOOL OF ENGINEERING

This dissertation was presented

by

Brendan M. Connolly

It was defended on

November 3, 2016

and approved by

Ian Nettleship, Ph.D., Associate Professor

John Oyler, Ph.D., Adjunct Associate Professor

Jorg Wiezorek, Ph.D., Professor

Scott Mao, Ph.D., Professor

Dissertation Director: Anthony DeArdo, Ph.D., Professor

THE EFFECTS OF COMPOSITION AND THERMAL PATH ON HOT DUCTILITY OF FORGING STEELS

Brendan Connolly, Ph.D.

University of Pittsburgh, 2016

This work examines the effects of composition and thermal path on the hot ductility of several forging steels with varied aluminum and nitrogen content. The primary mechanisms and controlling factors related to hot ductility are identified with a focus on the role of precipitates and segregation. The unique thermal paths and solidification structures of large cross-section forging ingots are discussed. Hot ductility testing is performed in a manner that approximates industrial conditions experienced by large cross-section forging ingots. A computer model for precipitation of aluminum nitride and vanadium nitride in austenite is presented. Industrial material is examined for comparison to experimental findings. It is found that increased aluminum and nitrogen content coarsens the as-solidified structure. The combined effects of microsegregation and uphill diffusion during deformation allow for carbide precipitation at prior austenite grain boundaries which reduces the hot ductility.

TABLE OF CONTENTS

LIST OF TABLES

LIST OF FIGURES

ACKNOWLEDGEMENTS

First and foremost I would like to thank Ellwood Group, Inc. and the Forging Industry Educational & Research Foundation for funding this work.

I am grateful to my Dissertation Director, Dr. Anthony DeArdo, for his guidance, mentoring and encouragement throughout this research and during my undergraduate years at the University of Pittsburgh. I am also thankful for support from the entire BAMPRI team, especially Dr. Ming Jian Hua, Bing Ma and Yu Gong, and for the helpful contact of Dr. Li at Clarion University.

There are so many people within the Ellwood Group that helped me with various parts of this work. I am certain that I do not have room on this page to name every person that assisted me, you all know who you are. With that said, I would like to explicitly acknowledge John Paules for his time, effort and support of this research.

To my family, friends and particularly my parents - thank you all for allowing me the time to complete this work without disowning me. Last but not least I want to thank my wife, Leeann, for her constant support and unending patience.

1.0 INTRODUCTION

Steel ingots remain a leading raw material for forging facilities producing critical large cross-section components in the energy, mining, defense and aerospace industries. Since the 1960's, continuous casting has largely replaced ingot casting due to increased yields and an improved as-cast structure. However, continuous casting is currently limited in cross-section to approximately 800 mm diameter maximum which precludes the material from use in heavy section products. Steel ingots, however, can be cast in weights up to 600 T and cross sections up to 4.2 meters. Steel ingots are also frequently used for specialty steel grades that are not conducive to continuous casting due to either the chemical composition or low tonnage requirements.

The gradual shift in the steel industry over the past half-century from ingot making to continuous casting has carried with it a change in the markets being serviced by steel ingots. As continuous casting absorbed the bulk tonnage of plain carbon steels, which accounts for more than 90% of steel production in the United States[1], ingot producers have found themselves servicing niche markets typically requiring specialized compositions with strict quality requirements. It is not correct to imply that continuous casting processes produce only low quality plain carbon steel, however the ingot products are generally of a higher alloy content and are therefore metallurgically quite complex compared to those produced in mass tonnage by the continuous casting method. The point to consider here is that a large portion of the research

funding in the steel industry shifted from ingot making to continuous casting as it was a newer and less understood process, while at the same time the ingot products were shifting to more complicated compositions which required more sophisticated processing.

Steel ingots are produced by pouring liquid steel into cast iron molds for solidification. High quality ingots are typically either bottom poured through a refractory-lined trumpet and runner system or top poured through an evacuated atmosphere as shown in Figure 1. Vacuum top pouring is more commonly used on very large cross-section ingots, which may weigh well over 100 tons, in order to minimize the hydrogen content and prevent hydrogen flaking. Once the steel has solidified it is removed from the mold, given a prescribed thermal handling cycle and brought to forging temperature for hot working operations.

There are three primary types of cracking phenomena that may be experienced during the production of steel ingots:

1. Solidification cracking – this type of cracking occurs during the ingot casting and solidification process. The cracks are typically longitudinal and readily visible to the naked eye upon removing the ingot from the mold.
2. Low-temperature stress cracks – these transgranular cracks occur due to inadequate stress relief or inadequate tempering of ingots that have transformed into a brittle microstructure and contain significant residual stresses due to thermal contraction and transformation-related volume changes.
3. Hot ductility cracks – this type of cracking is typically intergranular failure that occurs at higher temperatures. There are various causes for the reduction in ductility. The cracks may form in conjunction with or in the absence of deformation processes.

Within the very general hot ductility cracking category there are various causes for the intergranular failure. It is often difficult to verify with certainty a single particular cause of a hot ductility crack because the fracture surfaces are oxidized during the processing steps when cracking is identified. Furthermore the microstructure present when the cracking occurs is typically lost during cooling of the material to temperatures appropriate for metallurgical analysis.

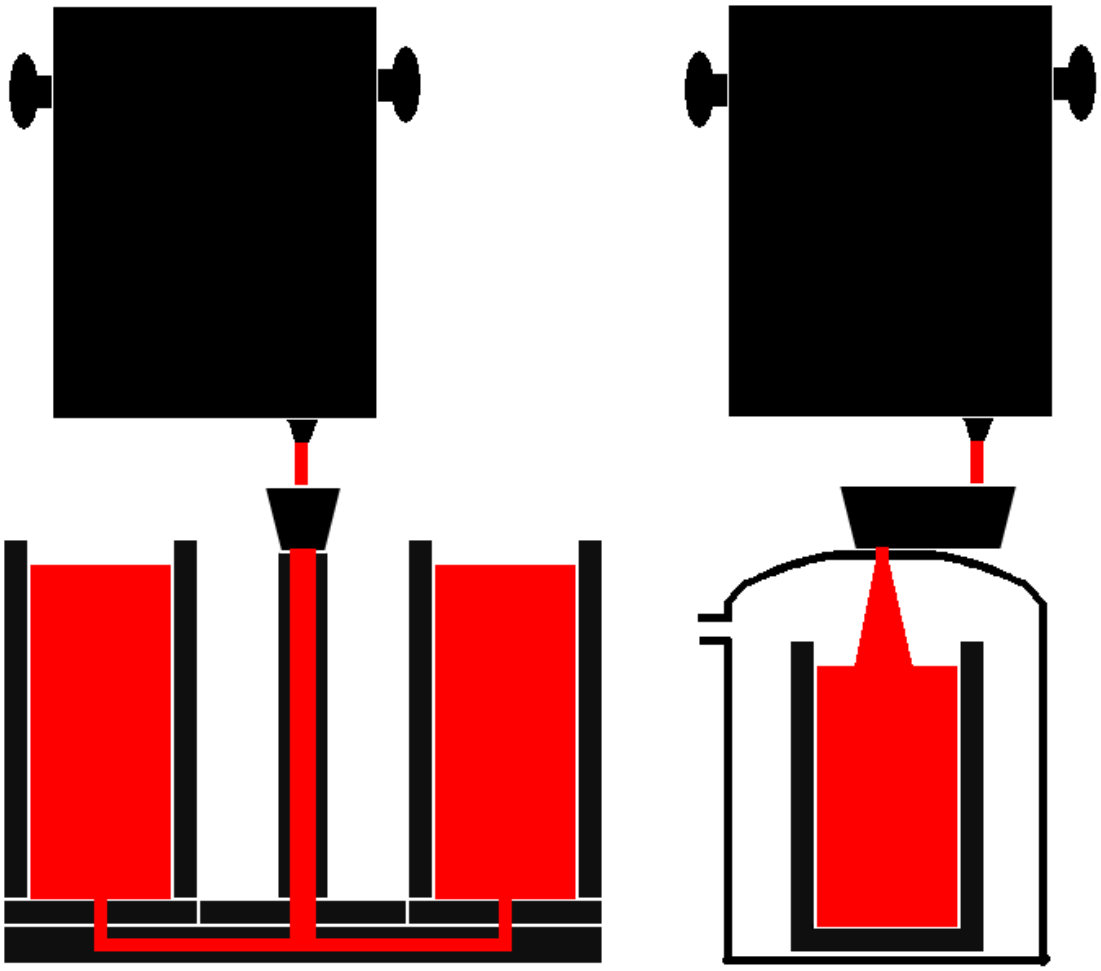

Figure 1: Ingot bottom pouring (left) and ingot vacuum pouring (right)

2.0 BACKGROUND

Steel ingots of various compositions can experience poor hot ductility that leads to cracking during or prior to the forging process. Hot ductility troughs have been identified and analyzed by many researchers[2,3,4,5,6,7,8,9,10,11,12,13] in the temperature range of 700˚ - 1200˚C, with the exact temperature range and severity of the trough varying by investigator, composition and experimental conditions. The ductility trough is often depicted by plotting hot tension percent reduction of area at failure (%RA) against test temperature for multiple samples. Figure 2 shows an example of typical hot ductility trough behavior from the work of Nachtrab et al.[3]. In this example, steels E2 through E4 contain increased levels of tin, aluminum and nitrogen, leading to deeper and wider hot ductility troughs.

A rapid drop in %RA values is commonly shown at some point within the temperature range noted above, while ductility is higher both above and below the trough. This loss in ductility has been attributed to many factors including precipitation of nitrides and/or carbides, segregation of impurities to austenitic grain boundaries and formation of ferrite at austenitic grain boundaries. At temperatures well below the Ar_3 temperature, the ductility usually returns to high %RA values due to the presence of a significant volume fraction of soft ferrite. At higher temperatures ductility is recovered by increased grain boundary mobility, dissolution and/or coarsening of grain boundary precipitates and an increased ability to recrystallize. At temperatures approaching the solidus, ductility drops sharply due to incipient melting.

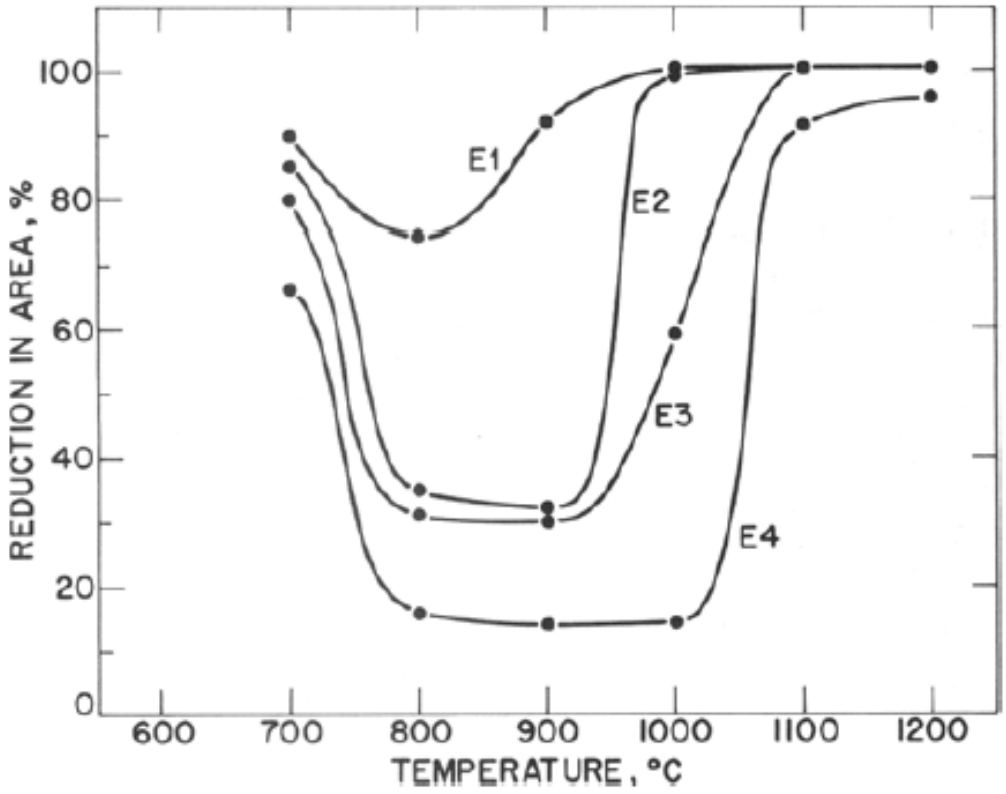

Figure 2: Typical hot ductility curves for various steels, from [3]

The subject of ductility loss is of great importance to the forging industry as it brings about multiple financial and quality burdens. First and foremost, crack formation due to low ductility causes yield loss. Beyond the obvious costs of material defects, many steel grades require strict thermal handling procedures to prevent such cracking and therefore additional furnace time is often necessary. The frequent occurrence of hot ductility issues on a specific product may also force changes to the chemical composition, possibly lowering the allowable nitrogen content and the allowable aluminum range, or adding less detrimental scavenger elements to control carbide and nitride formation, which may have associated costs. In recent years nitrogen is used more often as an alloying element for achieving increased strength while

maintaining low carbon equivalent values for weldability. This can present significant problems to the steelmaker and forger in developing new thermal handling procedures to avoid hot ductility issues in materials that had historically been problem free with respect to forgeability. The increased nitrogen content raises the precipitation temperature of nitrides that can be deleterious to the hot ductility.

This section will provide the necessary background information related to hot ductility loss as well as review the results of some previous investigators. Furthermore, the specific concerns of hot ductility loss as they relate to large cross-section ingots will be identified.

2.1 HOT DUCTILITY

Steel ingots are typically either forged or rolled into the near final shapes required for the components being produced. Deformation at high temperature allows recovery and recrystallization to take place dynamically during the working process and/or statically between working operations; otherwise a very sharp increase in hot strength would occur at the early stages of deformation and preclude further work due to hardening.

Ductility, in general, is the ability of a material to undergo deformation without fracture. At high homologous temperatures, T_H, it is common to refer to the hot ductility due to the very different material behavior when compared to room temperature steel. For the purposes of this work, the temperature range of interest is 700˚C - 1250˚C corresponding to T_H of 0.55 – 0.85. Some reasonable degree of hot ductility is necessary for the production of steel forgings. When steel is in a low ductility state, deformation may cause cracks or tears to form in the work piece. These defects may be shallow enough to remove by scarfing or they may be so deep that the

intended part can no longer be produced from the work piece. Even in cases where the steel is not forged or rolled, such as in steel castings, intergranular fracture due to nitride embrittlement at austenite grain boundaries has been documented[14] to occur when thermal and transformation stresses are present within the parts. Steel ingots can exhibit similar defects in the as-cast state, often referred to as panel cracks.

Crowther[9] identified several regions of the ductility trough for the case of continuously cast materials, namely I) Incipient melting, IIa) Second phase particles (sulfides), IIb) Second phase particles (carbides/nitrides) and III) Transformation (ferrite films), as shown in Figure 3. Such regions could be a reasonable starting point for defining the different factors causing ductility loss in ingots. The temperatures of regions IIa, IIb and III may overlap within the ductility trough, but the source of low ductility may be distinguished using electron microscopy on the fracture surfaces. While Crowther identified several contributing factors to ductility loss for various steels and conditions, these factors themselves do not thoroughly define the mechanisms which become active due to their presence. Defining such mechanisms is the most appropriate place to begin for understanding the effects of different processing variables on hot ductility.

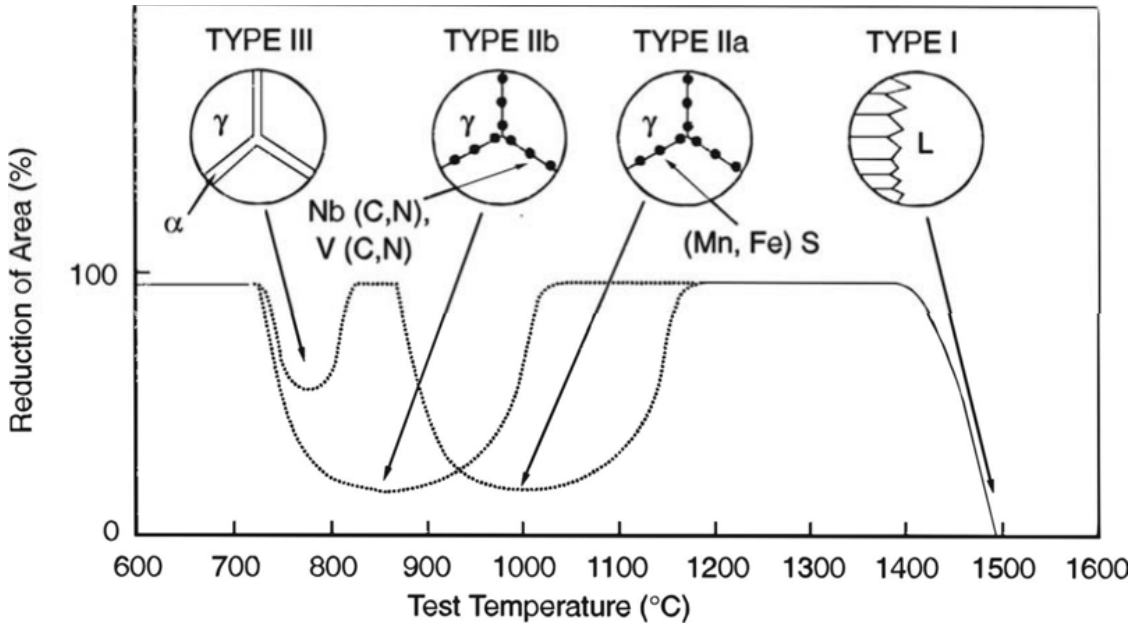

Figure 3: Types of hot ductility troughs, from [9]

2.2 MECHANISMS OF DUCTILITY LOSS

There are several mechanisms which have been shown to cause a significant loss in ductility. This section will address the fundamental mechanisms responsible for hot ductility loss and in some cases discuss the factors that affect whether a mechanism becomes active. It is worth noting at this point that the mechanisms are not mutually exclusive but can occur simultaneously. Furthermore, the activation of one mechanism can have an influence on parameters that control another.

2.2.1 Strain Concentration

There are two basic phenomena whereby strain concentrations may reduce the hot ductility of steel: 1) inadequate local strain to achieve recrystallization and 2) localized strains that cannot be accommodated, and these phenomena may occur simultaneously.

During hot deformation, the ability of steel to recover and/or recrystallize prevents a rapid increase of work hardening. When strain is unevenly distributed to small volumes within the work piece, the majority of the material is unable to achieve the critical strain necessary to initiate recrystallization. In addition to this, the very large strain in concentrated areas occurs more rapidly and can cause nucleation and growth of microvoids or crack propagation.

At normal forging temperatures, typically well above 1100°C, low alloy steels are fully austenitic. When the material is strained, the stress distribution is fairly uniform (on a micro-scale) across the austenite grains. Researchers[15,16,17] have demonstrated that a significant loss in ductility occurs when the austenite to ferrite transformation begins. Ferrite nuclei preferentially form at austenitic grain boundaries due to the higher energy and diffusion rates as compared to the austenite grain interiors[18]. Ferrite nuclei grow into thin films that surround the austenite grains. The soft ferrite films bear the majority of deformation and are able to quickly recover due to the high level of strain and thermal energy. Some research[15] suggests that the ferrite may even recrystallize at low strain rates. Thus, either through recovery or recrystallization, the ferrite films remain soft in comparison to the austenite. Further straining with dynamic softening of ferrite eventually results in microvoid growth and coalescence at the ferrite-austenite boundary. This type of failure is often characterized by the presence of small dimples (microvoids) covering the facets of austenite grains. At very low magnifications, this type of failure can easily be mistaken as brittle intergranular fracture because the relative size of the

readily visible austenite grains is very large in comparison to the tiny dimples that can be found at higher magnifications. While failure is brittle on the macroscopic scale, the actual failure mechanism on the microscopic scale is ductile. A micrograph presenting this type of failures is shown in Figure 4, where the prior austenite grains are clearly visible but the fracture mode at the grain boundaries is microvoid coalescence. This micrograph is from the work of Cowley et al.[19] where the sample was tested at a temperature between the Ar_3 and the Ae_3 which allowed ferrite to form at the austenite grain boundaries during the deformation process.

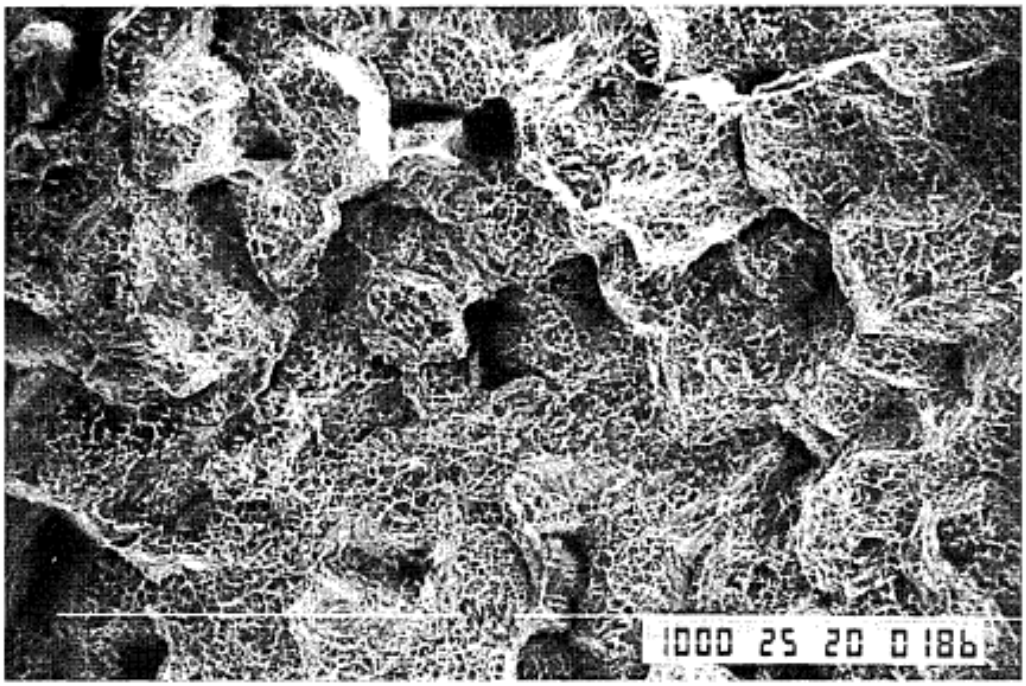

Figure 4: Microvoid coalascence along prior austenite grain boundaries, from [19]

During hot working, ferrite is able to precipitate at grain boundaries very near to, or even greater than[20] the Ae_3 temperature. This is known as deformation induced ferrite. The precipitation occurs on austenite grain boundaries due to the lower free energy barrier to

nucleation compared to the austenite grain interiors. The separation between Ae_3 and Ar_3 can be severe, nearing 150˚C in some cases[16,19], and so it is quite an important phenomenon to consider while discussing strain concentrations in the ferrite. The precipitation of deformation induced ferrite has been attributed[21] to an increase of nucleation sites by grain boundary bulging, subgrain formation, and an increased dislocation density. Thin films of deformation induced ferrite are detrimental to the steel ductility. It is clear[15] that at temperatures well below the Ar_3, where ferrite constitutes a higher volume fraction (approximately 50%[19]) the ductility recovers due to a more uniform distribution of strain. The stress distribution uniformity arises from the higher volume fraction of ferrite available to accommodate the strain and also from the more sluggish recovery of ferrite at lower temperatures which allows the flow stress of work hardened ferrite to approach that of the austenite[21].

Strain concentrations at austenite grain boundaries can also occur in the absence of ferrite. Precipitation of some carbides and nitrides occurs preferentially at the austenite grain boundaries due to lower volumetric misfit and faster diffusion coefficients as compared to the grain interior[22]. As precipitates nucleate and grow, they deplete the interstitials in the area near the austenite grain boundary region and thereby further hinder the nucleation and growth of precipitates near to the grain boundary. Thus, the grain boundary becomes strengthened or weakened by precipitates while the near-grain-boundary area remains precipitate free. These precipitate free zones (PFZ's) are softer than the surrounding steel and are therefore preferentially deformed, similar to the softer ferrite surrounding austenite grains discussed in the previous section[23,24]. This enhances grain boundary sliding and the fracture appearance is intergranular[25].

2.2.2 Grain Boundary Weakening

When grain boundary cohesion strength is low, the grain boundaries are a preferential area for propagation of cracks and voids. Grain boundaries may be weakened by the presence of undesirable elements or by precipitation at grain boundaries.

Several researchers have shown the negative effects of tramp elements such as P, Sn, Cu, Sb and As on the hot ductility of steel[4,26,27,28,29,30,31]. The loss in ductility has been demonstrated to be caused by segregation of these elements to the austenite or austenite/ferrite grain boundaries. The reduced grain boundary bonding strength in the presence of several tramp elements is due to the charge that is drawn from neighboring atoms to the embrittling element atoms, decreasing the metal-metal bond strength at the grain boundaries[32].

The effect of tramp elements on hot ductility is increasingly important for modern steel making because EAF steel accounts for well over 50% of total steel production in the United States[33]. Although the EAF process has many advantages and is quite efficient for melting scrap metal, there are some inherent disadvantages in using this method for the production of high quality steels. Of concern for this work are the elevated nitrogen levels of EAF steels compared to steels produced in the Basic Oxygen Furnace (BOF), and the effect of continuously recycling scrap steel. Steels produced by the EAF process typically range in nitrogen content from 50 – 120 ppm, while those produced in BOFs range from 10 – 40 ppm. The arc heating method during EAF melting is able to ionize nitrogen in the air (~78% N_2) so that it is readily absorbed by the steel bath. In the BOF process, large volumes of oxygen gas are injected into the liquid bath. The CO gas bubbles that are produced initially contain no nitrogen and thereby are able to further decrease the bath nitrogen content beyond what is supplied in the hot metal charge.

Continuous scrap recycling causes a slow increase in the undesirable residual elements over time. Iron yield from the EAF is not 100% due to oxidation during the melting process, so the final steel products usually will have a slightly higher content of Cu, Sn and other residual elements that are not readily oxidized during EAF melting. In the future, when the materials produced today have performed their duty and are recycled as scrap material once again, the residual content of the scrap will be slightly higher than it was previously. Many steel products also become contaminated with foreign materials that are undesirable in steel. For example, the copper wiring in used automobiles is often not completely removed during the shredding and subsequent non-ferrous metal separation processes. Steel produced from virgin ore by integrated steel mills will have residual impurity levels based solely on the purity of the ore and alloying additions.

The effects of several individual impurity elements on hot ductility have been examined by researchers. Martin[4] states that Cu causes a lower nucleation and growth rate of ferrite on austenitic grain boundaries. This extends the minimum of the ductility trough to much further below the Ar_3 temperature than other steels tested in his work because the ferrite films remain thin to lower temperatures. Guo et al.[28] suggest that phosphorus has little or no effect on the mechanism causing a ductility loss because the temperature range of the trough is unchanged by high phosphorus levels; however its presence at high concentration causes lower ductility values within the same trough boundaries. Cowley et al.[19] note that phosphorus segregation to vacancies formed during the deformation process may in fact improve ductility in samples where the ductility loss by Nb(C,N) would normally occur. In this case it is noted that phosphorus may occupy vacancy sites and hinder the precipitation of carbonitrides.

Nachtrab and Chou[34] examined grain boundary composition using an Auger microprobe and found that Cu, Sn and Sb do not segregate to the grain boundaries during a normal

austenitization heat treatment but segregate heavily when the samples are deformed. A summary of the extent of segregation in deformed samples is given below in Table 1. Nitrogen values are included in the table although they were not explicitly discussed by Nachtrab and Chou; it is unclear whether or not nitrogen was segregated in the undeformed austenitized samples.

Table 1: Grain boundary segregation due to deformation, from [34]

Heat-Sample	wt%Cu	wt%Sb	wt%Sn	wt%N	wt%C	wt%Mn
A - Bulk composition	0.059	0.0008	0.005	0.0159	0.17	1.40
A - Grain boundary	N/A	2.72	1.05	1.81	0.45	8.77
B - Bulk composition	0.178	0.0021	0.031	0.0109	0.12	1.43
B - Grain boundary	4.27	2.44	6.75	1.09	0.78	2.66
D - Bulk composition	0.263	0.0035	0.036	0.0096	0.19	1.32
D - Grain boundary	4.12	2.67	5.15	1.19	0.52	2.90

The samples in their work were deformed by hot tension testing. Unfortunately, Nachtrab and Chou did not examine the grain boundary composition in the heat which experienced no ductility loss (heat C in their work) due to the lack of grain boundary failure for examination. If the segregation levels were similar to those seen in the steels exhibiting ductility loss, this would suggest that segregation of the noted residuals in and of itself does not necessarily affect the hot ductility.

It has been proposed[35] that failure by grain boundary sliding is aided by the presence of fine precipitates both within the grains and along the austenitic grain boundaries. Grain boundary sliding is recognized as a mechanism for plastic deformation at high temperatures.

However, the deformation is typically accommodated by neighboring grains plastically deforming to fill the void left behind. When precipitates are present within the grain interior, the strengthening effect makes it more difficult for the neighboring grains to plastically flow into the void left by sliding. Additionally, grain boundary cavitation may occur when precipitates are present at the grain boundaries[28,35]. The precipitates can act as cavity nucleation sites and present a path for easy crack propagation, weakening the overall grain boundary strength.

Other research[3] has indicated that intergranular embrittlement may occur independently from precipitate formation at the grain boundaries. However, the occurrence of grain boundary segregation combined with precipitation of small second-phase particles further decreases the ductility when compared to samples that are free of precipitates.

2.2.3 Recrystallization Impediment

As stated previously, recovery and recrystallization are necessary in order to maintain the workability of forging steel to achieve the large strains necessary to produce useful shapes from cast ingots. The recovery process involves redistribution and annihilation of dislocations. During recovery, thermal and strain energy allow dislocations to become mobile and the dislocations begin to arrange themselves into lower energy configurations. It has been argued that the formation of subgrains may provide nucleation sites for recrystallization, however experimental evidence has shown that recovery processes inhibit the extent of recrystallization by reducing the driving force for growth of the recrystallized grains[36]. The main difference between recovery and recrystallization is that recovery does not involve the nucleation and growth of any new grains, but rather rearrangement of dislocations within the already existing grain structure.

Recrystallization of austenite has been shown to be a key element in maintaining high temperature ductility[5,15,19,29]. When recrystallization is not occurring, small cracks are easily able to propagate through the grain boundary network. Recrystallization presents obstacles to the crack propagation as the strain-free recrystallized grains nucleate on the existing austenite grain boundaries. The cracks that had already formed become isolated from the new grain boundaries and oriented towards the strained axis[28], reducing the stress normal to the crack.

The presence of fine precipitates can delay the recrystallization reaction[29,37]. Fine precipitates can hinder recovery and recrystallization by pinning dislocations and cell walls. Unfortunately, this often leads to a compromise between maintaining adequate hot ductility and achieving grain refinement for the required mechanical properties.

2.3 FACTORS AFFECTING HOT DUCTILITY

In this section, the major factors that have been determined to affect the mechanisms of hot ductility loss are reviewed. It is important to note that while composition will not be addressed specifically, most of the factors described below are significantly impacted by the steel composition due to its effect on precipitate solubilities and transformation temperatures.

2.3.1 Temperature

Thermal energy provides for enhanced diffusion, grain boundary mobility and dislocation mobility. The temperature also dictates the equilibrium distribution of phases present. A linear

equation developed by Andrews showing the effect of alloying elements on the equilibrium lower temperature limit of the austenite phase field, Ae_3, is given[38] as:

$$Ae_3(K) = 1186 - \Delta T - 25Mn - 11Cr - 20Cu + 60Si + 60Mo + 40W + 100V + 700P$$

where the term ΔT (K) is tabulated for carbon and nickel values as shown in Table 2 and all values are in weight percent.

Table 2: Effect of C and Ni on Ae_3

C + 0.1Ni	ΔT (K)	C + 0.1Ni	ΔT (K)	C + 0.1Ni	ΔT (K)
.05	24	.25	93	.45	137
.1	48	.3	106	.5	145
.15	64	.35	117	.6	160
.2	80	.4	128	.7	176

The equation is stated as valid for compositions up to 0.7%C, 3.0%Mn, 0.8%Si and 5.0%Ni. The Ae_3 temperature is decreased when Mn, Cr, Ni, C and Cu are increased in the steel. Kirkaldy and Baganis[39] developed a thermodynamic computer model that gives reasonable results for the Ae_3 temperature up to 7.0wt% alloying additions and is very accurate up to 2.5wt% alloying additions. Many forgers and steelmakers now use commercially available computer software to calculate transformation temperatures as in reality it is not possible to account for all of the compositional variations in modern steels using a mostly linear empirical equation. Knowledge of the transformation temperature for a given steel is critical in order to avoid straining the material while a two-phase structure of austenite grains surrounded by a thin

ferrite film is present. In the present work, dilatometry is the primary method for evaluating the transformation temperatures of the steel examined.

Thermal energy is a critical part of the recovery process. The kinetics of the recovery process can be described by a form of the Arrhenius equation[18]:

$$\frac{dX}{dt} = Ce^{\frac{-Q}{RT}}$$

where X represents the proportion of recovery, Q is the activation energy, R is the gas constant, T is absolute temperature in Kelvin and C is a constant. The rate of recovery is affected by the amount of recovery that has already occurred, and a more accurate form of the equation is given as[36]:

$$\frac{dX}{dt} = C_2 X e^{\frac{-(Q-mX)}{RT}}$$

where C_2 and m are constants, and the term mX accounts for the amount of recovery which has already occurred. It is readily seen that an increase in temperature increases the rate at which recovery can proceed.

The Johnson-Mehl-Avrami-Kolmogorov (JMAK) model provided the early foundations for recrystallization kinetics. The general form of the JMAK equation is given as[40]:

$$X_V = 1 - e^{(-Bt^n)}$$

where X_v is the fraction of recrystallized material, n is the Avrami exponent, t is time and B accounts for the shape factor (*f*), nucleation rate (N) and rate of grain growth (G). Temperature is again in the denominator of the exponent for both the nucleation rate and growth rate[40]:

$$N = C_1 e^{\left(-\frac{Q_N}{kT}\right)}$$

$$G = C_2 e^{\left(-\frac{Q_G}{kT}\right)}$$

where C_1 and C_2 are constants, Q_N and Q_G are activation energies and k is the Boltzmann constant. Therefore, the nucleation rate and growth rate of recrystallized grains is increased as temperature is increased.

When mechanisms which inhibit recovery and recrystallization are present, the thermal energy must be increased to overcome such barriers. In pure metals, the recrystallization temperature can be 150K less than that in metals with only 0.01 at% impurity element[18]. The amount of energy necessary for grain boundary motion increases due to the elastic field of the solute atom. Similarly, small precipitates may retard or even stop recrystallization[36] at a given temperature.

The thermal history is also a very important aspect of steel hot ductility as it impacts the size and distribution of precipitates and the austenitic grain size. Upon solidification and cooling, carbides and nitrides precipitate according to their local supersaturation. Some precipitates form preferentially on the austenite grain boundaries or within nucleated ferrite films between austenitic grains. Hot ductility is often improved in industrial materials that undergo transformation from austenite to ferrite and are subsequently re-austenitized then strained[13].

This is believed to be caused at least in part by precipitation of carbides and nitrides in the ferrite that is formed near the Ar_3. Upon reheating, the carbides and nitrides are no longer located at the newly formed austenitic grain boundaries. A schematic of this process from Thomas et al.[41] is shown in Figure 5, with aluminum nitride as the precipitate.

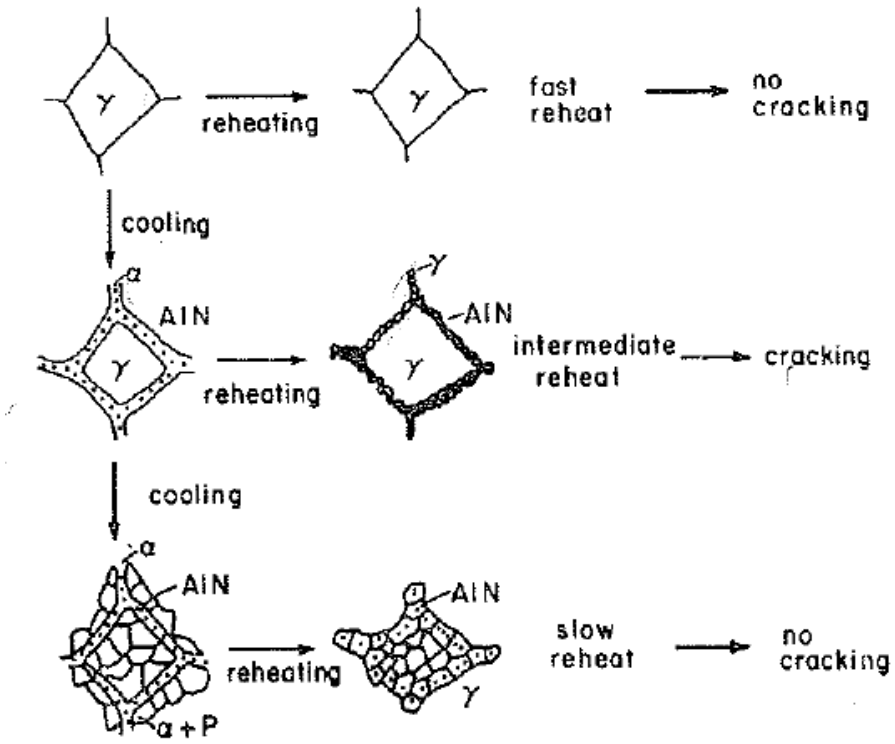

Figure 5: Effect of transformation and re-austenitization on grain boundary AlN, from [41]

2.3.2 Precipitates

Precipitates interact with the steel in various ways depending on their size, distribution and morphology. Historically, sulfide precipitation has been an important factor in hot ductility studies. Wilber et al.[13] showed that as Mn/S ratios increased in the range from ~20 – 80, the

%RA values in hot ductility tests increased correspondingly. The steel grades of interest in the present work are high quality, low sulfur steels (<0.003% sulfur with Mn/S ratios greater than 100) where sulfide precipitation should be expected to play only a minimal role, if any, in the hot ductility[42]. Additionally, the steels examined in this work are calcium-treated. Calcium has been noted[43] to raise the sulfide solution temperature relative to the pure MnS inclusions that form in non-calcium-treated steels. This has the effect of decreasing the amount of sulfur in solution at forging temperatures and therefore decreases the amount of sulfur available for re-precipitation as fine particles which would be detrimental to ductility.

One concern for this work is the effect of aluminum nitride on hot ductility. This is because industrial experience shows that steels with increased aluminum and nitrogen contents have a higher susceptibility to hot ductility cracking. Aluminum nitride has an HCP structure which is often cited as a reason for its sluggish precipitation kinetics in austenite. It has been suggested[36] that AlN may nucleate in FCC form and later develop the HCP structure which would decrease the nucleation barrier. There have been several studies to determine the solubility product of AlN in various steels. Kim et al.[44] determined the solubility product of AlN in liquid iron where at 1500°C, $k_{AlN} = 0.0115$ indicating that even at abnormally high levels of aluminum (>0.05% Al) and nitrogen (>150 ppm N), AlN should remain in solution at liquid steelmaking temperatures. Table 3 and Figure 6 below show the solubility of AlN in austenite as determined by previous investigators. Several of the experimentally determined solubility products are in general agreement with one another, with only moderate variations between experimenters; the larger variations in experimentally determined solubility products are likely caused by differences in chemical composition and analytical equipment. However, thermodynamic calculations[45,46,47] and the thermoelectric power technique used by SiyaSiya[36] have shown a somewhat lower solubility of AlN, possibly due to the inability of many

experimental methods to adequately account for very small (<10 nm) precipitates[48]. SiyaSiya's work shows lower solubility values throughout the entire temperature range, while the thermodynamic calculations do not diverge greatly from the experimental works until lower temperatures. The highest solubilities were found by Darken[49] using Sievert's law and by Shimose and Narita[50] using Beeghly's method on Fe-Al-N alloys.

Table 3: Equilibrium solubility products for AlN

Label	Ref	Log[Al][N]	Method	Comment (compositions in wt %)
A	49	-7400/T+1.95	Sievert's	0.1C, 0.4Mn
B	51	-6770/T+1.03	Beeghly	0.05C, 0.35Mn
C	52	-6180/T+0.725	Beeghly	0.2C, 0.5Mn
D	52	-6015/T+0.309	Beeghly	0.16C, 0.4Mn, 3.4Ni, 1Cr
E	50	-7184/T+1.79	Beeghly	Fe-Al-N
F	53	-7750/T+1.8	Beeghly	0.2C, 0.5Si, 1.5Mn
G	54	-7500/T+1.48	Beeghly	0.1C, 0.24Si, 0.8Mn
H	36	-9710/T+2.6	TEP	0.04C, 0.2Mn
I	55	-10020/T+3.577	Beeghly	Pure Fe
J	55	-9295/T+3.079	Beeghly	0.4C, 1.3Cr, 1.5Ni
K	45	-11568/T+4.5989	Thermodynamic	
L	47	-14356/T+6.4	Thermodynamic	
M	46	-11085/T+4.382	Thermodynamic	
N	56	-6690/T+1.21	Beeghly	0.04C, 0.3Mn
P	57	-5938/T+0.528	Beeghly	0.1C, 0.68Mn

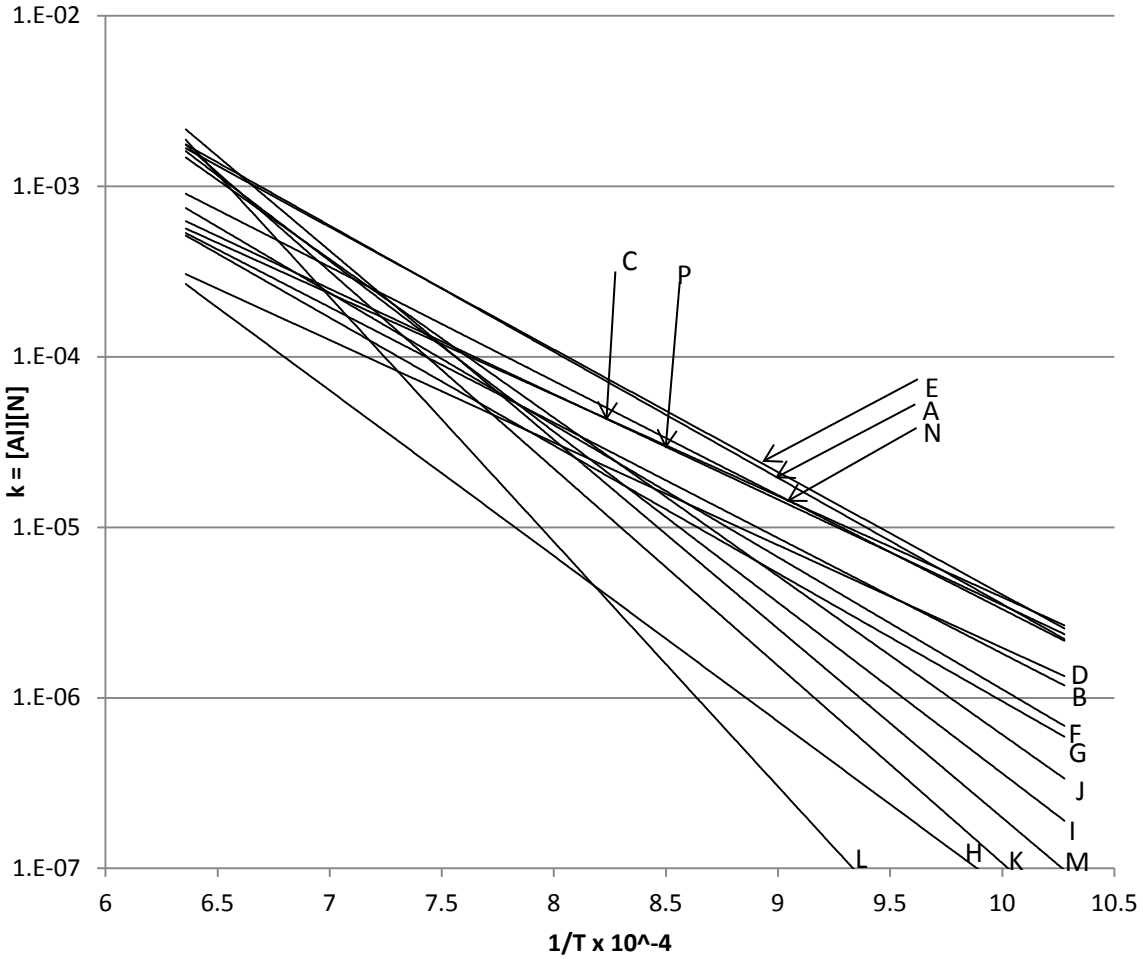

Figure 6: AlN solubility products vs temperature

At forging temperatures of approximately 1200˚C, and assuming bulk aluminum and nitrogen contents of, for example, 0.030% Al and 75 ppm N, the AlN solubility product is 2.25×10^{-4}. This data point is situated such that the AlN could be fully dissolved or precipitated to a significant volume fraction depending on the solubility product chosen. This shows that while the use of these equations may give an indication of the equilibrium solubility of AlN, in general it is not possible to definitively say that AlN will be present at a given temperature without physical or empirical evidence supporting such a claim when the data fall within the

range of the equations given. Furthermore, segregation to grain boundaries may increase the local aluminum concentration by a factor of six[25] which would lead to AlN precipitation even at levels expected to be well below the solubility limit.

Some research [36,58] has shown fast dissolution (<10 minutes) of AlN particles when samples are heated above the solution temperature. This contradicts the results of Cepeda et al.[29] who found large precipitates of approximately 0.1 μm diameter (too large to have been precipitated on cooling) that were present after 1 hour of solution treatment at 1200°C. It remains difficult, however, to definitively say that the steels used in the work of Cepeda et al., with [Al][N] = $2.7x10^{-4}$, were heated to above the true solution temperature. The researchers used the solubility product from Gladman and Pickering[54] where log[Al][N] = -7500/T + 1.48. From this expression, the solubility temperature is in fact 1212˚C and, therefore, even if the solubility product given by Gladman and Pickering was known to be correct, the solution temperature used by Cepeda et al. was inadequate for complete dissolution. It should also be noted that in a separate study[59] Gladman found AlN particle coarsening to greater than 0.2 μm at temperatures above 1250˚C. In that study he showed that the overall number of particles decreased while the typical particle size increased.

Compared to aluminum, nitrogen diffuses very quickly though austenite. The diffusion coefficients have been given in $cm^2\ s^{-1}$ as[36]:

$$D_{Al}^{\gamma} = 5.9e^{\frac{-241000}{RT}}$$

$$D_{N}^{\gamma} = 4.88x10^{-3}e^{\frac{-76780}{RT}}$$

It is seen that at 1000˚C, the diffusion coefficient of N is more than three orders of magnitude larger than that of Al. This implies that the rate of AlN growth is controlled by diffusion of aluminum to the precipitates and diffusion of nitrogen may be assumed infinite. The same is not

necessarily true for the rate of nucleation; as noted previously, it has been suggested that the low nucleation rate is due to the difficulty of forming HCP structures in the FCC matrix. It seems reasonable that the rate of dissolution of AlN may also be controlled by the ability of aluminum atoms to diffuse away from the near precipitate region and thereby lower the local [Al][N] product so further dissolution may occur. The following exercise confirms that dissolution times of even coarse particles should in theory be very fast if controlled by aluminum diffusion away from the precipitates:

Suppose that a mixed AlN distribution is present in iron with the aforementioned [Al][N] product of 2.25×10^{-4}, where a single AlN particle of 20 nm diameter and a single particle of 0.4μm diameter exist in the material. Assume that both particles are spherical and equilibrium solubility dictates that all AlN is in solution at 1049°C according to solubility equation A from Table 3. The small amount of precipitation allows the assumption that the matrix concentrations of aluminum and nitrogen remain unchanged. If the steel is heated to 1050°C, then the undersaturation, S, is very small (approximately -0.00147) because the temperature is only one degree above the solution temperature. Following quasi-static linear diffusion theory[60], the dissolution time is given as:

$$t_{dissolution} = \frac{-R_0^2}{2D_{Al}^{\gamma} S}$$

where R_0 is the initial particle radius and D_{Al}^{γ} is the diffusion coefficient for aluminum in austenite. The calculation shows that a particle 0.4 μm in diameter should fully dissolve within 75 seconds, and the small 20 nm particle should dissolve in less than one second. Even these short times are an overestimate as the shrinking particle/matrix interface was not accounted for. A further increase in temperature will drastically increase the undersaturation as well as the aluminum diffusion coefficient and thereby hasten dissolution.

Aluminum nitride is virtually insoluble in ferrite and precipitation kinetics are accelerated when the austenite to ferrite transformation occurs[61]. As will be discussed in section 2.5, steel ingots of significant cross-section require long solidification times and the surface temperature is typically on the order of ~650°C when the ingot is removed from the mold. For most forging steels at this temperature, a significant amount of ferrite and AlN precipitates can be expected in areas near to the ingot surface.

There are of course additional carbide, nitride and carbonitride forming elements that can greatly influence the hot ductility of steels. Vanadium, titanium and niobium are common microalloying additions to high-strength low alloy (HSLA) steels. Carbides and nitrides of these elements are NaCl-type cubic structures[62] and are therefore more easily nucleated than aluminum nitride in steels. Niobium carbonitrides are documented[9,63] to be extremely detrimental to hot ductility, even more so than aluminum nitride. This is due to the fine precipitate size of the Nb(C,N) particles. Niobium in solution is also credited with segregating to austenite grain boundaries and producing significant solute drag which inhibits grain boundary motion[64]. Grain boundary motion is necessary for recrystallization and therefore even the soluble niobium can have adverse effects on hot ductility. Titanium carbonitrides are not typically linked to hot ductility losses in industrial ingots and the use of titanium is often avoided due to its deleterious effect on certain mechanical properties. However, laboratory results from Spradbery and Mintz[65] found that small titanium additions in rapidly solidified and cooled samples further reduced ductility in C-Mn-Al and C-Mn-Al-Nb steels. The slow cooling conditions of a solidifying steel ingot allow ample time for TiN coarsening and this in effect reduces the soluble N left for precipitation of other fine nitrides[9]. The extremely low solubility of TiN in austenite ensures that dissolution does not occur under normal forging conditions and therefore re-precipitation as fine particles is prevented. In the steels that are of interest for this

work, neither niobium nor titanium are present in any significant amount and therefore further discussion of their effects is not necessary. Vanadium, however, is present as an alloying element for all of the steels tested.

Vanadium carbonitrides are significantly more soluble in austenite compared to aluminum nitride. Solubility data for VC and VN are shown in Figure 7. Vanadium has been stated[62] to have no effect on austenite recrystallization due to its relatively high solubility. However, Medina et al[66] show that strain-induced precipitation is able to inhibit recrystallization progress at least for a short period of time when temperatures are low enough for the recrystallization driving force to be temporarily overcome by the pinning force of V(C,N). Vanadium nitride precipitates have been shown to negatively affect hot ductility, but to a lesser degree than Nb(C,N)[63]. In tests where samples were solution treated and then strained under conditions to simulate the continuous casting thermomechanical path, it was found that the VN precipitate size was on average larger than that of Nb(C,N) as shown in Figure 8.

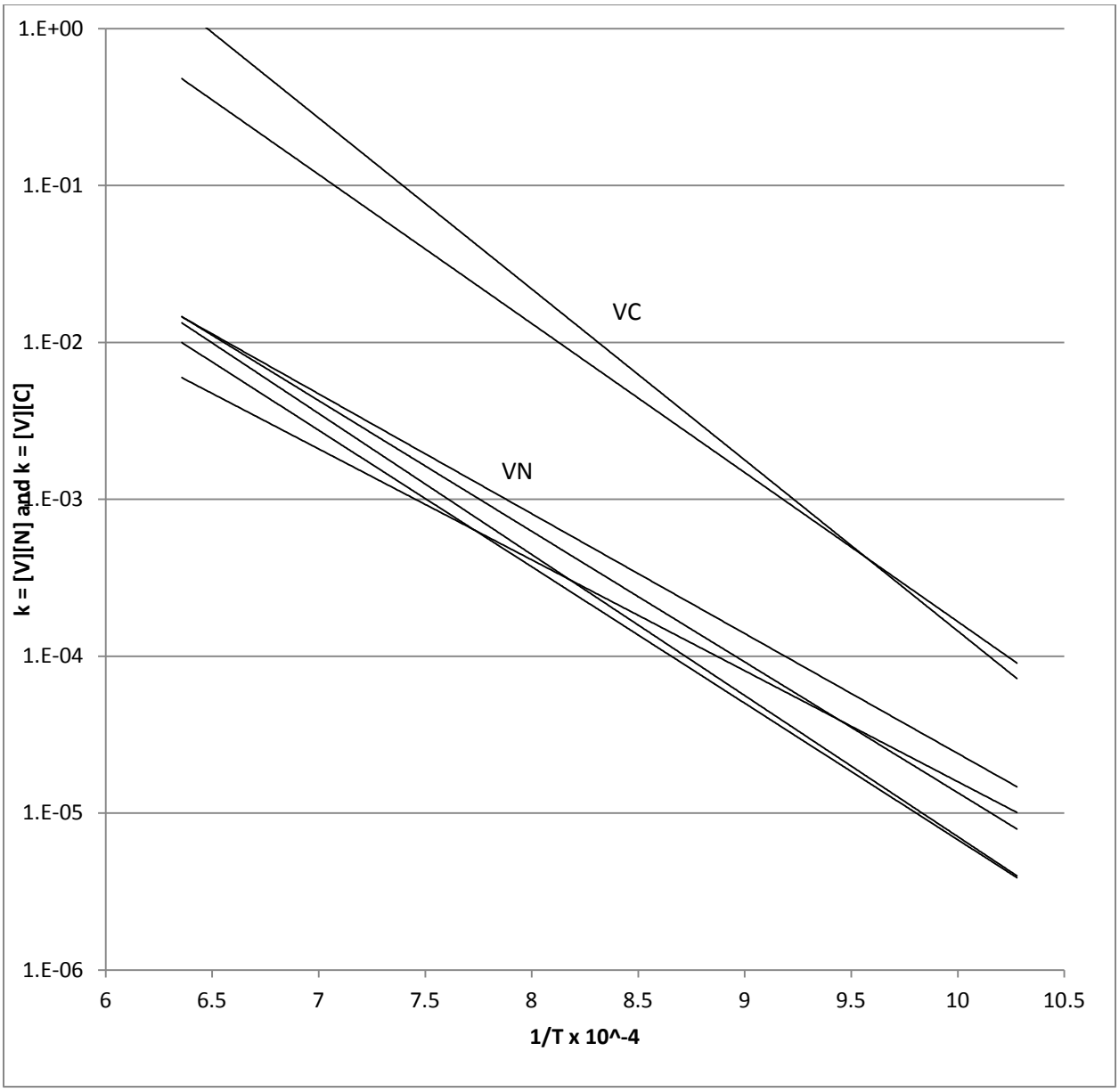

Figure 7: Solubility data for VC and VN, from [62]

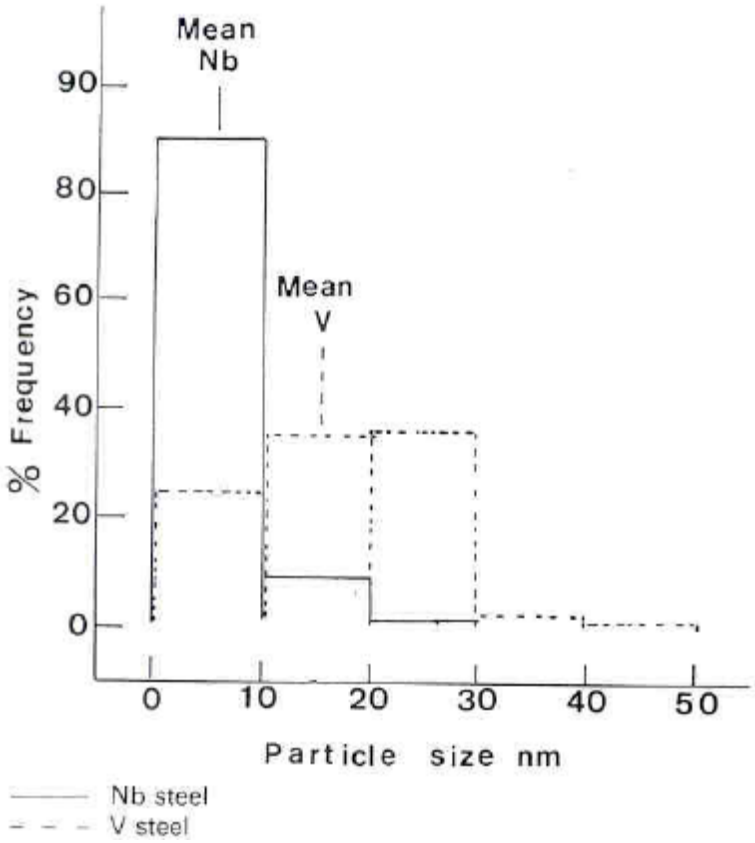

Figure 8: Particle size distribution for VN and Nb(C,N); from [63]

In addition to sulfides and the microalloying element carbides and nitrides, there are several substitutional elements known to form carbides in steel. Chromium and molybdenum are both present in the steels examined in this work. Typically the carbides of substitutional elements have a much higher solubility in steel than the microalloys, but elements such as chromium and molybdenum are often present in much larger quantities than the microalloying elements. The solubility of alloy carbides is significantly lower in ferrite than in austenite, and the carbides often precipitate during tempering of low alloy steels.

Some research[67] has shown that various transitional carbides such as M_7C_3 are present in the microstructure of low alloy steel (2.25Cr-1Mo-0.25V) quenched from austenite temperatures.

The hot ductility reduction of tool steels due to the precipitation of alloy carbides in austenite is well documented[68,69,70]. The tool steel compositions showing this effect vary significantly depending on final commercial application, but normally the carbon content is greater than 0.50% and the total carbide-forming alloy content is in excess of 5%. One well-documented carbide is $M_{23}C_6$. The solubility product for $Cr_{23}C_6$ in austenite is given[71] as:

$$\log([Cr]^{23}[C]^{6}) = 61.81 - \frac{50618.73}{T}$$

In the P20 steel of this work, the $Cr_{23}C_6$ precipitates would be soluble over the full range of austenitic temperatures. This implies that significant segregation would be necessary in order to precipitate the carbide in austenite. Segregation is present to some degree in all steels, but is exacerbated by the slow solidification rate of large cross-section ingots. The work of Basirat and Fredriksson[72] shows that uphill diffusion can occur during deformation of bearing steel, and the carbide forming elements chromium and molybdenum exhibit significant segregation to the banded regions of deformed steels. The slow solidification and cooling of low alloy steels can facilitate segregation banding that is severe enough to allow for carbide formation within the segregation bands, even for steels where such precipitation would not be expected from the bulk composition[73]. There are various transitional carbides that can precipitate under appropriate thermodynamic and kinetic conditions such as MC, M_2C, M_7C_3, M_aC_b, etc., but there are few published data available regarding the solubility products for these carbides as their precipitation is heavily dependent on steel composition and thermal history.

2.3.3 Strain Rate

It is generally shown[15,29,74] that a decrease in strain rate causes an appreciable lowering of hot ductility. Some research has suggested[29] that at low strain rates the amount of strain energy is incapable of reaching the values necessary for recrystallization to fully occur in normal testing conditions. In addition, high strain rates may not provide the necessary time for ferrite formation[74] when testing near the Ae_3, thereby making low strain rates appear to cause an appreciable loss in ductility while in reality it is the high strain rate preventing the ductility loss that would eventually occur.

Mintz et al[15] state that lower strain rates may encourage grain boundary sliding in higher carbon (>0.30%) steels and raise the start temperature of dynamic recrystallization. It was shown that at strain rates of $3x10^{-4}s^{-1}$, dynamic recrystallization began at approximately 900°C, while at lower strain rates of $3x10^{-3}s^{-1}$ dynamic recrystallization occurred at approximately 800°C. It is worth noting that the Ae_3 and Ar_3 temperatures in this steel were calculated to be 774°C and 625°C respectively, well below the temperature of dynamic recrystallization. The ductility at all strain rates appeared to begin improving at temperatures around that of dynamic recrystallization. At the lowest strain rate, $3x10^{-4}$ s^{-1}, there were two levels of ductility loss. The higher temperature ductility loss is associated with loss of dynamic recrystallization, and a further drop in ductility occurs at the Ae_3 temperature where deformation induced ferrite may have started to precipitate. The low strain rate tests did not recover ductility until reaching the Ar_3 temperature. In the samples strained at higher rates, the ductility trough appeared to be more uniform, reaching a minimum ductility just below the Ae_3 temperature and quickly returning to higher ductility as temperature was decreased. The fast ductility recovery at lower temperatures for samples strained at higher rates was understood to be caused by precipitation of deformation

induced ferrite. The ferrite precipitation is a diffusion controlled process so higher strain rates will allow less time for recovery processes to occur, leading to work hardening of the ferrite[75] and an equalization of strain distribution between strong austenite and hardened ferrite. In coarse grained material, as long as the strain rate remains low enough for near full recovery to take place, the deformation induced ferrite never will be able to grow into the grain interiors and reach a volume fraction large enough to accommodate the strain while maintaining ductility[21]. Conversely, in fine grained material the deformation induced ferrite volume fraction may be large even at low strain rates due to the increased work hardening that occurs in fine grained material which provides additional strain energy for deformation induced ferrite precipitation and growth.

2.3.4 Grain Size and Morphology

The effect of grain size on hot ductility of steels was critically analyzed by Moon[76]. Moon's work concluded that an increasing grain size widens the ductility trough and also shifts it toward higher temperatures, as noted by other investigators[15,17,77]. A smaller grain size provides a much larger surface area for nucleation of particles, increasing the average interparticle spacing for a given volume fraction and particle size. However, the increased number of nucleation sites will generally lead to a higher nucleation rate and therefore smaller overall precipitate size due local undersaturation from soft impingement. In this way the smaller grain size ends up providing a finer precipitate distribution. It is interesting to note that the smaller grain size will also provide additional nucleation sites for ferrite. Therefore, the precipitated ferrite film should be much thinner for a given volume fraction due to the larger grain boundary area covered, which is expected to extend the lower end of the ductility trough to lower temperatures.

The austenite grain size is controlled by the temperature, the distribution of precipitates and the thermal history. Fine precipitates cause a drag force on otherwise moving grain boundaries. Grain coarsening often precedes dissolution of AlN particles, however this is understood to be caused by an increase in average particle size at the expense of the number of particles per unit volume[59]. The Zener model describes the pinning action of particles on grain boundary mobility[78]. The classical version of this model is given as

$$R = \frac{4r}{3f_v}$$

where R is the grain radius, r is the particle radius (assumed spherical) and f_v is the volume fraction of precipitates. Several researchers have since proposed various modifications to the Zener model in order to account for known deviations such as abnormal grain growth and grain boundary curvature to particle radius ratio[79]. From the classic Zener model, it can be seen that a large volume fraction of small particles will give a fine austenite grain size. The volume fraction of aluminum nitride, f_{AlN}, can be determined from the relation[79]

$$f_{AlN} = \frac{(AlN)\rho_m}{100\rho_{AlN}}$$

where (AlN) is the weight percent AlN precipitated from the matrix, ρ_m is the density of the matrix (steel) and ρ_{AlN} is the density of aluminum nitride, 3.2 kgm^{-3}. The value for (AlN) is given as

$$(AlN) = \frac{(M_{Al} + M_N)}{2M_N}\left\{\left(N_0 + Al_0\frac{M_N}{M_{Al}}\right) - \left[\left(N_0 + Al_0\frac{M_N}{M_{Al}}\right)^2 - \frac{4M_N}{M_{Al}}(Al_0N_0 - K_{AlN})\right]^{\frac{1}{2}}\right\}$$

where M_X represents the atomic mass of element X and Al_0, N_0 are the bulk concentrations of aluminum and nitrogen in weight percent.

Titanium nitride is the most thermodynamically stable of the common grain-refining precipitates[79]. In some cases where hot ductility is a major processing issue, titanium additions may be used to act as a grain refiner in substitute of aluminum. However, Ti(C,N) precipitates can be detrimental to fatigue and low temperature impact properties of high strength steels and therefore titanium additions are most often avoided for critical cyclically loaded parts such as shafts and rotors. Pickering[80] showed that post solidification cooling rates of less than about 10°C/min will give TiN precipitates that are too coarse for effective grain refinement.

Aluminum nitride is a very efficient grain refiner even at temperatures exceeding 1000˚C. Due to the sluggish precipitation kinetics of AlN in austenite, V(C,N) often precipitates prior to AlN during continuous cooling although the nose of the V(C,N) precipitation curve is at a lower temperature than that of AlN. However, AlN is a more stable precipitate and given enough time will replace existing VN particles when excess nitrogen is not present[48]. This effect is shown in Figure 9. Vanadium carbonitrides also provide effective grain refinement in many steels where the aluminum content must be kept at low levels. The steels to be studied in this work contain a significant amount of vanadium and this must be taken into consideration when interpreting results.

Another important aspect of the grain size is its effect on recrystallization kinetics. A finer grain size allows for a more severe work hardening process to occur during deformation[36]. The additional strain energy shortens the necessary time to reach a given amount of recrystallization and lowers the recrystallization temperature. The enhancement of recrystallization kinetics improves the overall hot ductility for fine grained material.

Although somewhat less studied than grain size as related to hot ductility, the grain morphology plays an important role due to the nature of the as-cast grain structure. During solidification the initial shell formed has an equiaxed grain structure due to the very rapid

cooling and high nucleation rate of solid crystallites in the liquid. Shortly after the shell is formed and supercooling is lessened, the equiaxed crystallite nuclei with fast-growing orientations (i.e. <100> directions) situated nearly parallel to the direction of heat flow begin to grow rapidly opposite the direction of heat extraction. The formation of columnar grains is aided in that the heat of fusion further suppresses the growth of less-favorably oriented crystallites[18]. Towards the center of the ingot where heat extraction is approximately homogenous across all radial directions, the grain structure returns to the equiaxed form but with larger grains than at the surface chill zone due to the low nucleation rate.

Mintz et al.[17] showed that hot ductility is greatly improved at all temperatures when the grain size normal to the tensile axis is decreased, i.e. when the columnar grains are oriented parallel to stress. The research indicated that shear stresses play an important role in nucleating microcracks by grain boundary sliding. In samples tested with columnar grains oriented perpendicular to the stress axis, the shear strains will be highest near the tips of columnar grains where the angle between the normal stress and grain boundary approaches 45°. The cracks then propagate easily through the long dimension of the columnar grains as the normal stress is nearly perpendicular. The hoop stresses present in a cooling steel ingot are unfortunately oriented perpendicular to the long direction of columnar grain growth. Additionally, circumferential tensile forces on the bulging faces of ingots during open die forging are oriented in the same perpendicular direction with respect to the columnar grains.

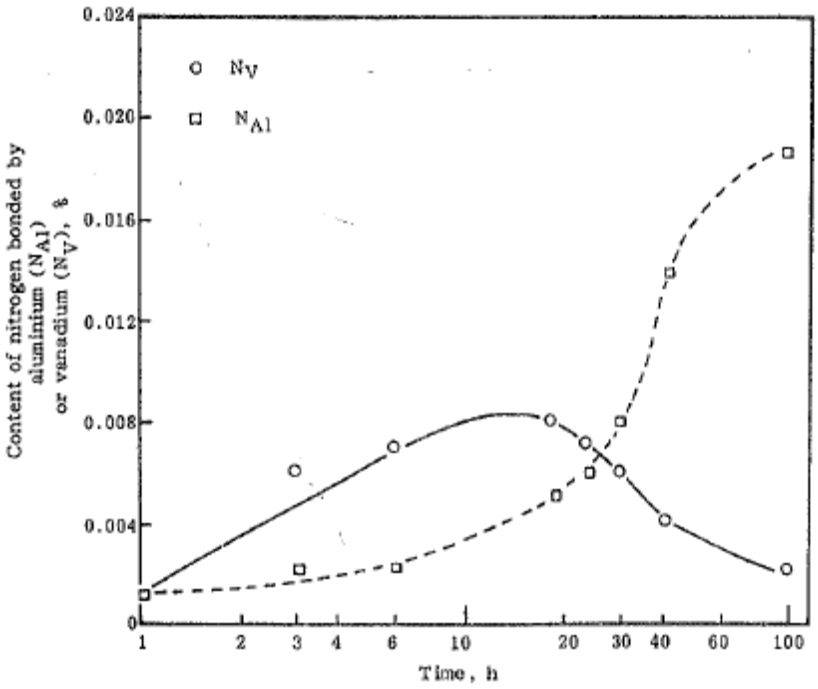

Figure 9: AlN replacing VN in absence of excess nitrogen, from [48]

2.4 HOT DUCTILITY CRACKING

In the forging of steel ingots, there are essentially two distinct cracking phenomena that are experienced during the hot working process. The first is a case where large tears are formed during the initial forging operations at high temperature (~1200˚C). The second case occurs later in the forging process as surface temperatures of work pieces are dropping due to heat transfer to the forging dies and the ambient atmosphere. Another type of ductility crack may appear *after* forging, during post-forge cooling if the as-forged grain size is relatively coarse and precipitation of fine particles occurs on the grain boundaries. All of these cases have been found in industrial practice to be exacerbated by high aluminum and nitrogen levels, and are more common in nickel-containing steels. The effect of nickel on aluminum nitride formation remains somewhat

unclear. The 3.5NiCrMo steels are found through industrial experience to be troublesome in terms of forgeability and the work by Erasmus[52] suggested that higher nickel contents reduce the AlN solubility. However, it was noted[48] that the work done by Erasmus may have been flawed in that the AlN solubility in Ni-Cr steel was tested by the Beeghly method which is not capable of distinguishing AlN from CrN. In the Fe-N-Ni system[81], nickel is shown to lower the solubility of nitrogen in austenitic Fe-Ni alloys but the effect is somewhat unimpressive for the nickel contents of typical low alloy forging steels. For example at 1200°C, an increase from 0.0% Ni to 3.3% Ni only decreases the soluble nitrogen from ~0.0235% to ~0.0210%.

2.4.1 Cracking During Initial Forging

Cracks that form during the initial forging operation are typically large, transverse tears that run deep into the work piece. These cracks are a point of interest for this work as they occur at temperatures around 1200˚C when the work pieces are fully austenitic and most or all of the carbides and nitrides should be dissolved. It is hypothesized that the appearance of these cracks early during the forging process may in some cases be due to propagation of pre-existing subsurface cracks that formed in the ingot during the thermal handling cycle.

Naumann and Spies[82] investigated cracking that occurred during the initial forging steps of a 0.40%C-1.4%Mn-0.3%Mo steel. The steel was cast as an octagonal tapered ingot of approximately 1 m in cross-section and 1.8 m tall. The ingot was stripped from the mold 10.75 hrs after pouring and charged directly into a 1080°C furnace, ramped to 1200°C and held for 10 hours prior to forging. The aluminum and nitrogen contents were 0.022% Al and 0.017% N, respectively, so [Al][N] = 3.7×10^{-4} which is above the solubility limit at 1200°C for several of the equations given in Table 3. Another ingot produced under the same conditions, except with

Al = 0.012% and N = 0.0102%, [Al][N] = $1.2x10^{-4}$ and only 5.25 hours hold time in the mold showed no cracking. It is not clear if the improved hot ductility occurred due to the reduced [Al][N] product, the higher stripping temperature, or the combination of these changes.

When working with crack-prone steels, some forgers use a light pass on the press before truly working the piece in order to "condition" the surface; industry uses the term "saddening" for this process. Saddening has been found beneficial in the forging industry and has also shown good results in hot rolling experiments[83]. The result is a near surface strain that is sufficient to ensure some amount of recrystallization while avoiding the large strains at high strain rates that would allow formation or propagation of cracks. Once recrystallization has occurred at the surface, the steel becomes somewhat desensitized until further embrittling mechanisms such as re-solution and precipitation of nitrides or carbides come into play.

2.4.2 Cracking During Late Stages of Forging

The tight, relatively shallow cracks that form later in the forging process or during post-forge cooling are occurring at lower temperatures than those described in the previous section. Such cracks are expected to be caused by a coarse-grained structure and a widened ductility trough extending to temperatures overlapping those at finish forging. Finish forging temperatures are not normally below ~875˚C, so it is obvious that forgers intend to avoid formation of ferrite which could cause a significant ductility loss. Coarse-grained structures may arise from extended reheat times when forgings are not able to be completed on the first heat, which may contribute to late stage cracking.

These cracks can be tight enough that they are missed by operators examining the as-forged surface and they become visible only upon machining. Adequate stock removal can

sometimes fully remove these shallow defects, however additional stock with the accompanying yield loss may be necessary in the high nickel steels. The high nickel steels form a strong mechanically bonded scale layer[84] which must be accounted for as it decreases the true excess stock amount. Should these cracks originate below the surface but not propagate fully, they are another possible source for the subsurface-type defects to be discussed in the next section.

2.4.3 Subsurface Defects

As noted in section 2.4.1, pre-existing subsurface flaws may be present within the ingot. It is known that as-cast material contains some amount of porosity due to solidification shrinkage. The porosity in an as-cast structure, such as micropores at interdendritic regions and secondary piping at ingot centerlines, is typically closed during forging. When inadequate forge penetration occurs, porosity in the forged product can be located by means of ultrasonic testing and is often found at or near the centerline. The centerline region of the ingot is not only the most porous region of the ingot, but it also receives the least amount of deformation during open-die forging processes. When unhealed defects are isolated and examined microscopically, as-cast dendritic features are typically observed. If MnS inclusions can be located on the defect surface, they remain undeformed confirming the lack of hot work in that region. Figure 10 shows an example of the as-cast structure due to inadequate forging consolidation. Note that the MnS inclusions and grain structure are not deformed. Thermal grooving is present due to the surface tension of the grain boundaries.

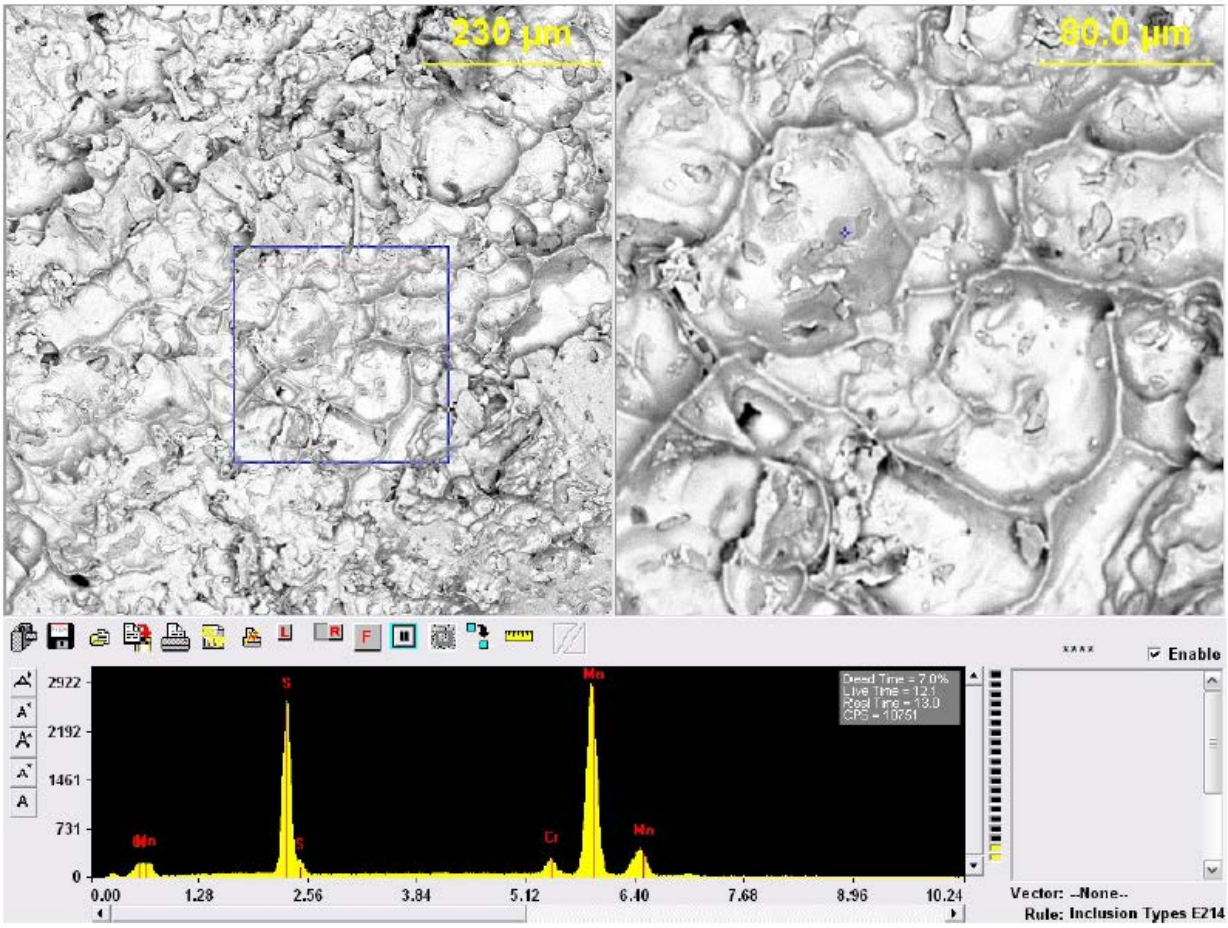

Figure 10: SEM image of as-cast structure and undeformed MnS

It is quite interesting that forgers have found defects similar in appearance to non-consolidation, except located very near to the surface of the forged and rough-machined piece. In order to have remnant porosity in these areas, one would expect to find gross non-metallics that would prevent consolidation during deformation. However, these subsurface defects are found to be free of non-metallic particles. The fracture surface morphology shows smoothed-over features which can easily be mistaken for as-cast structures. Tremaine[85] showed that rounding and smoothing of defect surface features can occur at typical forging temperatures in a reasonably short time. Industrial investigations of defects are often performed using optical or

scanning electron microscopy because of the relative ease of sample preparation and analysis. It is reasonable that if such fracture surfaces were able to be examined at higher magnifications, small precipitates may be found associated with the subsurface flaws. Defects of this type contradict the theory[86] that internal cracks not exposed to the forging surface or oxygen will completely heal during hot working, assuming that these defects are present during forging. This is a reasonable assumption to make when the fracture surface morphology shows no signs of microvoid coalescence, cleavage or grain facets. That said, such defects may also be occurring in the later stages of forging, but the relatively low heat treating temperatures and decreased holding times (due to smaller as-forged cross-sections) would not be expected to have as great an effect in modifying the fracture surface morphology.

2.5 LARGE CROSS-SECTION INGOTS

2.5.1 Solidification and Cooling

Large cross-section forging ingots are solidified in cast iron molds. Unlike in a water-cooled continuous casting mold, solidification of large ingots is a slow process that occurs over a period of hours rather than minutes. During initial filling of the mold and for a short time period afterwards, a solid shell of steel is quickly formed at the inner mold wall due to fast heat extraction from the low temperature mold. The steel shell shrinks away from the mold wall as it thickens and cools further, leaving an air gap between the solidifying ingot and the mold wall. This air gap insulates the solidifying ingot and slows the heat extraction.

Strain rates of approximately $3x10^{-6}$ s^{-1} have been calculated[87] due to thermal contraction during cooling. As previously discussed, low strain rates are detrimental to hot ductility. Thomas et al.[86] showed that a low carbon steel ingot was in compression at the surface during solidification and mold cooling. Tensile stresses were not predicted to occur in ingot surface until the ingot was stripped from the mold when the ingot surface cools and contracts rapidly. The composition used for this modeling fell into the peritectic range as given by Blazek et al.[88], however the δ-ferrite to austenite transformation was stated to have no effect on stress generation due to the active recovery mechanisms at very high temperatures. Peritectic grades are known to be prone to cracking during the solidification process but these types of cracks are not of concern for this work. It should be noted that such cracks are readily visible when they do occur and are not likely be overlooked by operators while an ingot is being stripped from the mold.

Hannerz[89] showed theoretically that high cooling rates may be able to suppress the formation of carbides and/or nitrides that might cause ductility issues. However, the cooling rates necessary are typically not achievable during industrial ingot casting. It is not feasible to quickly through-cool a large cross-section ingot of low alloy steel due to the high thermal stresses that will form on the surface, likely causing stress-relief cracking to occur.

2.5.2 Chemical Segregation

The slow solidification and cooling of large ingots enhances both micro- and macrosegregation effects as compared to continuously cast materials. Solute rejection causes enrichment of the interdendritic liquid during solidification due to the lower solubility of most alloying elements in the solid phase compared to that of the liquid[90]. The compositional differences between

dendrites and the interdendritic regions are referred to as microsegregation. On a larger scale, the growth of the solidification front progressively enriches the remaining liquid causing macrosegregation of solute elements toward the last areas to solidify in the ingot. The partitioning of alloying and residual elements to the liquid phase during solidification can give rise to significant localized compositional differences. The varied compositions can result in localized microstructural inhomogeneities, sometimes referred to as segregation banding. Segregation banding is a direct result of the chemical segregation that occurs during dendritic solidification[91]. The microsegregation can be reduced with increased solidification rates (less time for diffusion) and long equalization times at high temperature, but it is never completely eliminated. The effect is substantial in large ingots. The partition ratio, *k*, is the ratio of the solute concentration in the solid to that of the liquid at some temperature[91]:

$$k = \frac{C_S}{C_L}$$

Lower values of the partition ratio indicate strong segregation into the interdendritic liquid during solidification. The partition ratios for various common elements in steel are given in Table 4.

Partial homogenization of microsegregation may occur at temperatures where atoms are mobile enough to achieve reasonable diffusion distances. However, some elements may further segregate to grain boundaries or other interfaces due to the reduction in overall energy when there is a large size misfit or difference in electronic structure when compared to the matrix[92]. Such cases of segregation occur preferentially at high energy boundaries[93] and are commonly associated with temper embrittlement.

Segregation of carbon and molybdenum to austenite grain boundaries was confirmed by atom probe tomography in the work of Li et al.[94]. Papworth and Williams[95] reported finding segregation of Ni, Mn, Cr, Mo and P at the prior austenite grain boundaries using FEGSTEM.

As stated in section 2.2.2, deformation may enhance segregation of certain elements to interfacial areas such as grain boundaries and can reduce ductility. Janovec et al.[96] reported that deformation accelerates the diffusion of carbon and chromium to prior austenite grain boundaries. In addition to the effects on grain boundary weakening, segregation of strong ferrite formers may contribute to ferrite formation at the grain boundaries even above the Ae_3 temperature of the bulk steel.

Although it should not be considered segregation in the classical sense, non-homogenous composition due to precipitate dissolution has been suggested as a possible mechanism for ferrite formation above the Ae_3 temperature[52]. Both aluminum and vanadium are strong ferrite formers, and during reheating to temperatures where particle dissolution is occurring the concentrations of such elements near the particle interface may be high enough to induce ferrite formation. Knowing that the large strains produced during open die forging generate significant amounts of heat within the steel and that the dissolution time for AlN particles is quite fast, it is reasonable to suppose that some local ferrite formation may occur dynamically due to local thermodynamic conditions. This ferrite formation would be further enhanced by the mechanisms which produce deformation induced ferrite.

Table 4: Equilibrium partition ratios in iron and steel

Element	K	Ref.
P	0.14	91
Cr	0.33	91
Mn	0.71	91
Ni	0.83	91
Al	0.92*	97
C	0.30	97
N	0.48	97
Si	0.50	97
S	0.05	97

*Al value is for liquid/δ-ferrite partitioning rather than liquid/austenite

2.5.3 Thermal Handling Paths

Most steel ingot producers require specific thermal handling paths for a given steel grade and ingot size. The thermal handling cycles are designed mainly to prevent cracking when the steel is not able to be hot charged into a forging furnace. Strain cracking is a term used to describe the cracks that form due to thermal and transformation stresses which exceed the material yield strength during cooling. In certain cases, such as when producing grades prone to low ductility tearing during forging, specially designed thermal handling cycles may be used for the sole purpose of maximizing the hot ductility of the steel.

Direct hot charging of solidified ingots into forging furnaces is by far the most economical and ideal thermal handling path available. The retained heat within the ingot shortens heat-to-forge time and decreases the associated energy costs. Unfortunately for many steel grades such as those containing moderate amounts of nitride and/or carbide forming elements, this path can result in forging tears occurring in the early stages of hot working. The forging tears are often intergranular in nature and presumed to be the result of precipitates present at the austenitic grain boundaries. Although the term "hot charging" is used, it must be remembered that the surface and near-surface areas of the ingot are usually around 600 - 700°C at the time of stripping from the mold. At this temperature a significant amount of ferrite should be present in the microstructure and potentially a significant volume fraction of AlN or other grain boundary precipitates. Sussman et al.[98] showed that panel cracks (a slightly different manifestation of the AlN problem) may be reduced by avoiding holds at the temperature range of 650 - 1100°C. Unfortunately, this temperature range coincides with many of the solidification and forging process temperatures.

In order to minimize the occurrence of crack formation during forging, some steel grades may be air cooled to below the Ar_1 temperature to ensure complete transformation of austenite. Carbides and nitrides precipitate quickly in the ferrite as the austenite begins to transform. Upon reheating to forging temperatures, new austenite grains are formed that now contain the precipitates at the grain interiors rather than on grain boundaries. It is often convenient to apply a surface transformation to large ingots rather than complete transformation due to the long cooling times necessary to reach satisfactory temperatures. Ingots may be placed in a water bath for a short period of time to fully transform a shallow layer at the ingot surface. This process is similar to the in-line quenching used to improve efficiency and prevent cracking in continuously

cast slab steel production[99]. Upon removal from the quench bath, the retained heat from the ingot interior quickly tempers the surface should there be a brittle low-temperature phase present.

In the case where an ingot is charged into the forging furnace hot (shortly after stripping from the mold), heating to forging temperatures requires no special steps to avoid heating bursts. On the other hand, ingots that have been allowed to significantly cool prior to forging require care during the heat-to-forge process. Upon initial charging into a hot furnace, the thermal expansion of the outer surface of the ingot causes tensile stresses to develop on the ingot interior. If not heated slowly or in a stepwise fashion, the tensile stresses may cause a tear to form within the ingot body. The location of this crack is typically towards the center of the ingot, where it will be difficult to close on forging if there is inadequate forging penetration.

3.0 STATEMENT OF PROBLEM, HYPOTHESIS AND OBJECTIVES

3.1 STATEMENT OF PROBLEM

The subject of low ductility in the temperature range from 700˚ - 1200˚C has been thoroughly studied in order to reduce the occurrence of transverse cracking during the unbending process of continuous casting, prevent panel cracking in ingots and provide guidelines for thermal handling and chemical composition that aid in improving the hot ductility of steels. There remain challenges, however, in efficiently and economically producing fine grained, low oxygen, low sulfur, large cross-section forging ingots of high cleanliness that are consistently free of defects related to hot ductility. One such challenge is achieving the proper balance between deoxidation, grain refinement and tearing susceptibility. There are many steel grades where increased aluminum contents would provide improved grain refinement, less complicated liquid steel processing and lower total oxygen content, however the same steel grades are historically prone to ductility cracking or have shown subsurface defects like those discussed in section 2.4.3. Even at relatively low aluminum contents (~0.010 – 0.015%), some ductility issues are occasionally experienced by the forger. This is especially true for steels with increased nitrogen contents.

3.2 HYPOTHESIS

High aluminum and nitrogen content in low-alloyed steels increases the precipitation temperature of aluminum nitride. It is hypothesized that aluminum nitride precipitates nucleate on as-cast austenite grain boundaries causing a reduction in the hot ductility of the steel due to pinning of austenite grain boundaries. The precipitate distribution is not expected to be detrimental during the forging process due to particle dissolution and coarsening at forging temperature. This implies that the tears discovered during the initial forging operations of large ingots are pre-existing defects that propagate to the surface and become visible during forging rather than being caused by forging the steel while it is in a low ductility state.

3.3 OBJECTIVES

Modified P20 steel was chosen as the ideal material for this work. P20 is a low-alloy tool steel that is widely used for plastic injection molding and is known to be occasionally susceptible to hot ductility cracking. The nominal composition of the P20 steel in this work is 0.34C-1.5Mn-2Cr-0.2Mo-1Ni. The objectives of this work are to:

- Evaluate the hot ductility behavior of as-cast P20 steel.
- Identify the role of aluminum and nitrogen content on the hot ductility of as-cast P20 steel.
- Determine the primary cause for hot ductility loss in as-cast P20 steel, which is hypothesized to be due to precipitation of AlN on austenite grain boundaries.

Hot ductility behavior is studied using hot tension testing with in-situ melting in order to preserve the as-solidified structure. P20 steel with varied aluminum and nitrogen contents are tested under identical conditions to study the effects of these elements on hot ductility. The tested samples are then examined using various metallurgical techniques in order to determine the cause of hot ductility loss.

The results of this work are expected to be used by ingot producers and forgers to develop sound guidelines for determining the proper thermal handling procedures and acceptable levels of aluminum and nitrogen.

4.0 EXPERIMENTAL PROCEDURE

4.1 MATERIALS

Four commercial heats of modified P20 tool steel were produced with varied Al and N contents as listed in Table 5 below (in wt%).

Table 5: Compositions of P20 steels examined

Steel	C	Mn	P	S	Si	Ni	Cr	Mo	V	Cu	Al	N
A	0.35	1.45	0.013	0.003	0.29	0.80	1.97	0.22	0.057	0.19	0.008	0.008
B	0.35	1.46	0.008	0.002	0.30	0.81	1.99	0.22	0.055	0.17	0.015	0.009
C	0.34	1.53	0.011	0.003	0.34	0.78	2.03	0.22	0.059	0.19	0.040	0.013
D	0.35	1.46	0.009	0.001	0.29	0.87	1.88	0.19	0.044	0.17	0.008	0.015

The P20 steels were chosen because of tendencies toward poor ductility or subsurface porosity that are experienced by industry. The low sulfur content of all steels examined should reduce the possible influence of Mn/S ratio on hot ductility.

Steel samples were provided by Ellwood Group, Inc. The steel was melted in an electric arc furnace, refined in a ladle furnace, vacuum degassed and bottom poured into ingots. The ingots were open-die forged into commercial slabs and 25 mm thick slices were taken from the

slab bottoms. The slices were of various widths and lengths depending on the final commercial application for the particular slab. 25x25x240 mm bars were cut from the slabs, turned on a lathe to 22 mm diameter rounds and then machined to the specific dimensions described in section 4.2. No samples were taken from within 150 mm of the longitudinal centerline of the slices in order to avoid compositional variations due to macrosegregation, namely for carbon and sulfur.

4.2 HOT DUCTILITY TESTING

Hot ductility can be tested by several methods[100] including hot torsion, compression, tension and bending. A quantitative measure of ductility is provided by the reduction of area in the tension test and by the number of turns to failure in the torsion test. In bending and compression tests, failure does not necessarily occur and often the samples are tested under varying parameters and ductility is deduced from the condition of the sample (e.g. cracks present, extent of cracking, etc.) after testing.

Of the available means for measuring hot ductility, the hot tension test is the most appealing for this work. In a method outlined by Revaux, Bricout and Oudin[2], in-situ solidification may be performed within the tension testing apparatus, as shown in Figure 11. In-situ cast specimens exhibit grain boundary segregation which may reduce the bulk concentrations required to exceed the solubility limit for precipitate formation[101].

In some cases, in-situ solidification introduces a shrinkage cavity into the sample due to the volume contraction that occurs during the liquid to austenite phase transformation. The design of the crucible in the present work maintains soundness in the deformation zone by using

a big-end-up taper of ~7% and by introducing a notch at mid-length of the crucible. The notched area, being of smallest cross-section, bears the strain. The solidification cavity remains above the notched area because as solidification progresses, the higher density solid crystallites tend to fall through the liquid allowing a progression of the solidified front from bottom to top. Revaux, Bricout and Oudin used light pressure to ensure the solidification cavity was moved outside of the deformation zone; the same method was employed in the current work.

A similar tensile sample design was used for the current work, only slight modifications were made. The design of the fused quartz crucible was nearly identical to that used by Revaux, Bricout and Oudin. Figure 12 shows a schematic of the tensile specimen and fused quartz crucible used in the present work.

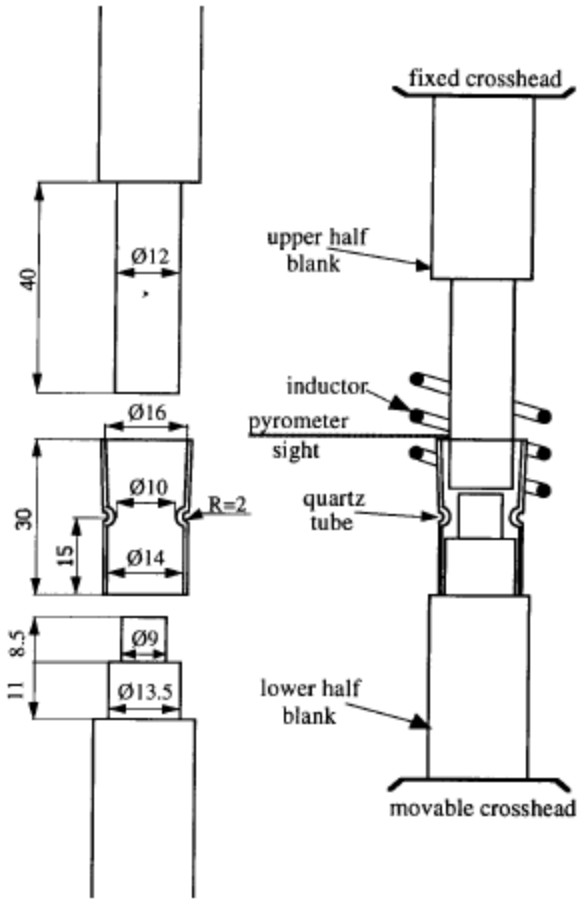

Figure 11: Experimental setup from Revaux, Bricout and Oudin[2], dimension in mm

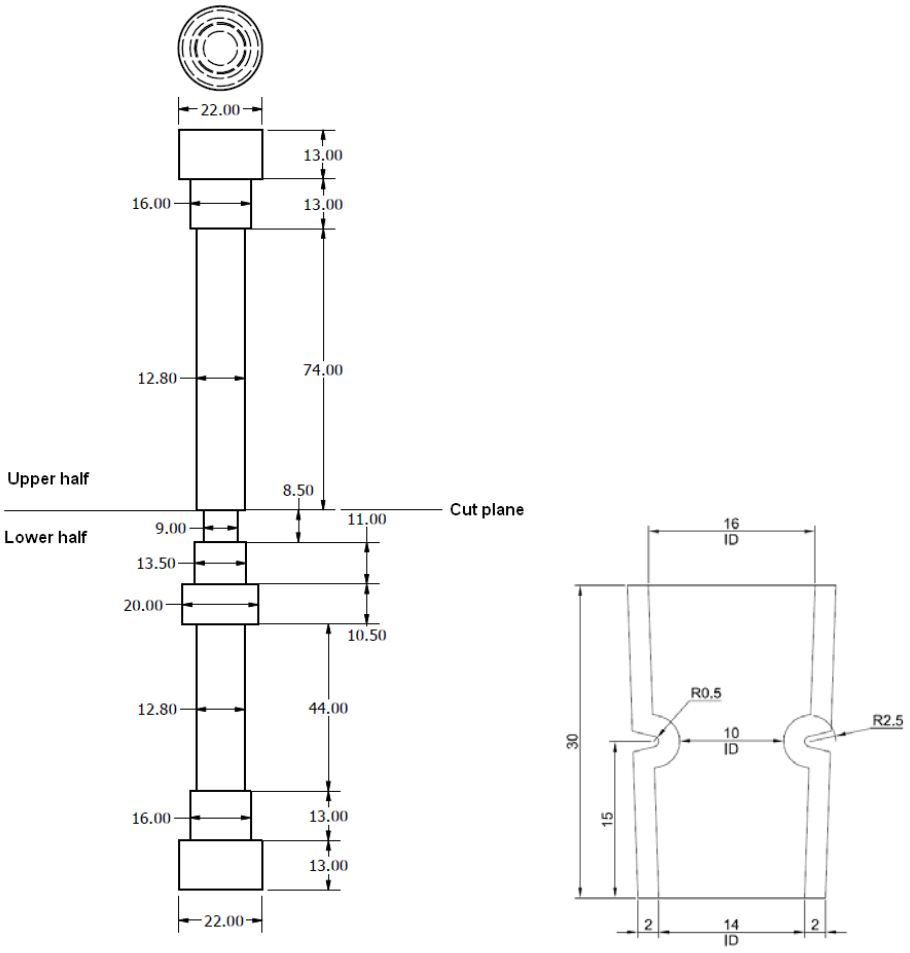

Figure 12: Schematic of specimen and crucible for present work, dimensions in mm

4.2.1 Equipment

An Instron testing frame was fitted with high-temperature alloy grips, insulated heating chamber and inert argon gas purging. The heating chamber was constructed from a 254 mm diameter steel cylinder with 3.2 mm wall thickness. The cylinder is insulated with 25 mm thick refractory fiber and has a 100x100 mm high-temperature glass viewing window for observation during testing. The cylinder is fixed to the upper tensile grip arm and is hinged along its vertical axis for sample access. The heating chamber has ports for inert gas purging, induction coil, optical pyrometer sight and an access port for breaking the melt crucible away from the sample. A rendering of the insulated heating chamber mounted on the tensile frame is shown below in Figures 13 and 14.

The three-turn water-cooled induction coil is connected to a 10 kW Pillar MK-20 computer controlled power supply. The induction coil leads are isolated from the heating chamber shell by electrically insulating cloth. Temperature readings are obtained from an Omega IR2C dual color optical pyrometer. Cold water is supplied at 30°C maximum by a closed-loop pump with a direct-contact heat exchanger.

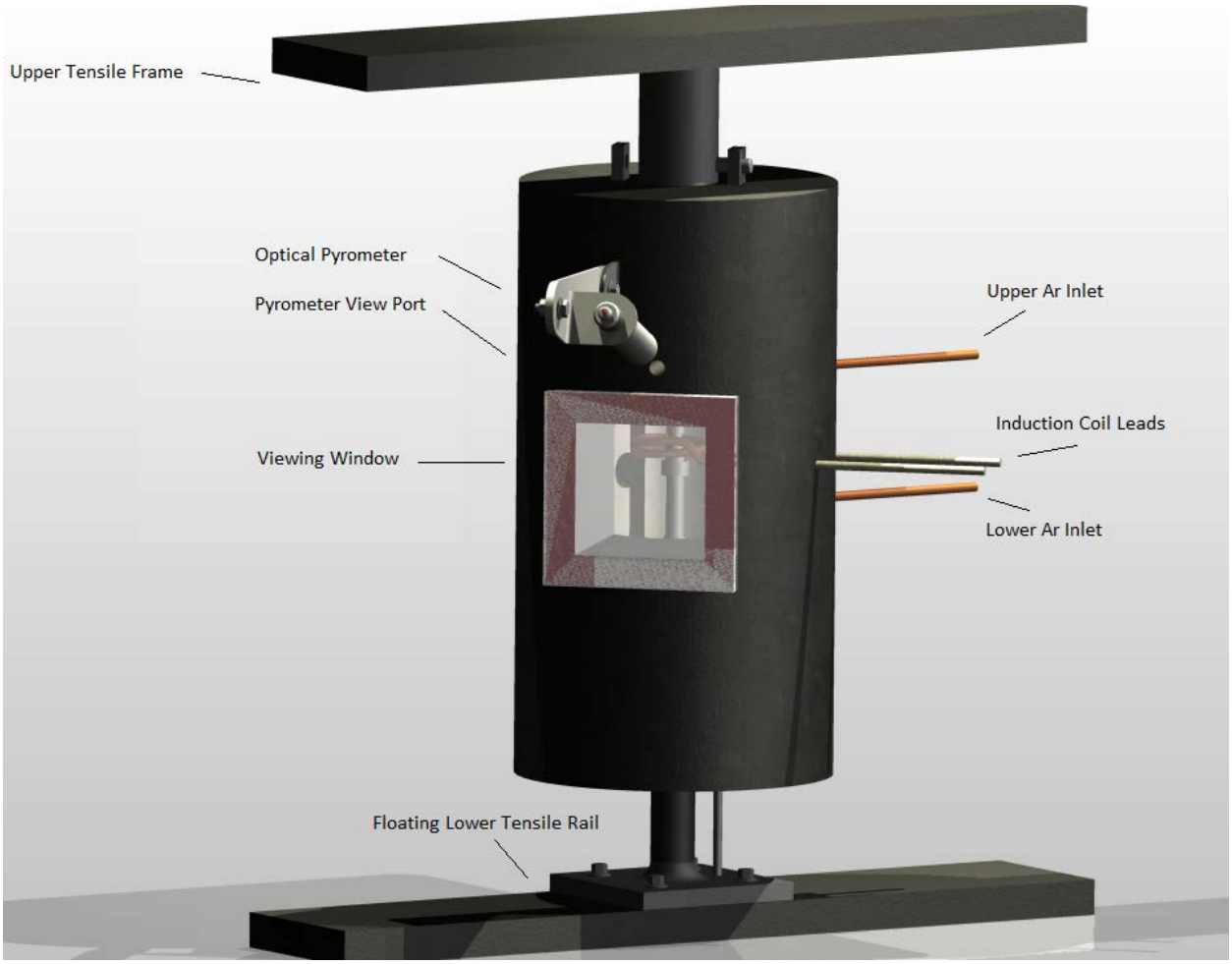

Figure 13: Heating chamber mounted on tensile frame (closed)

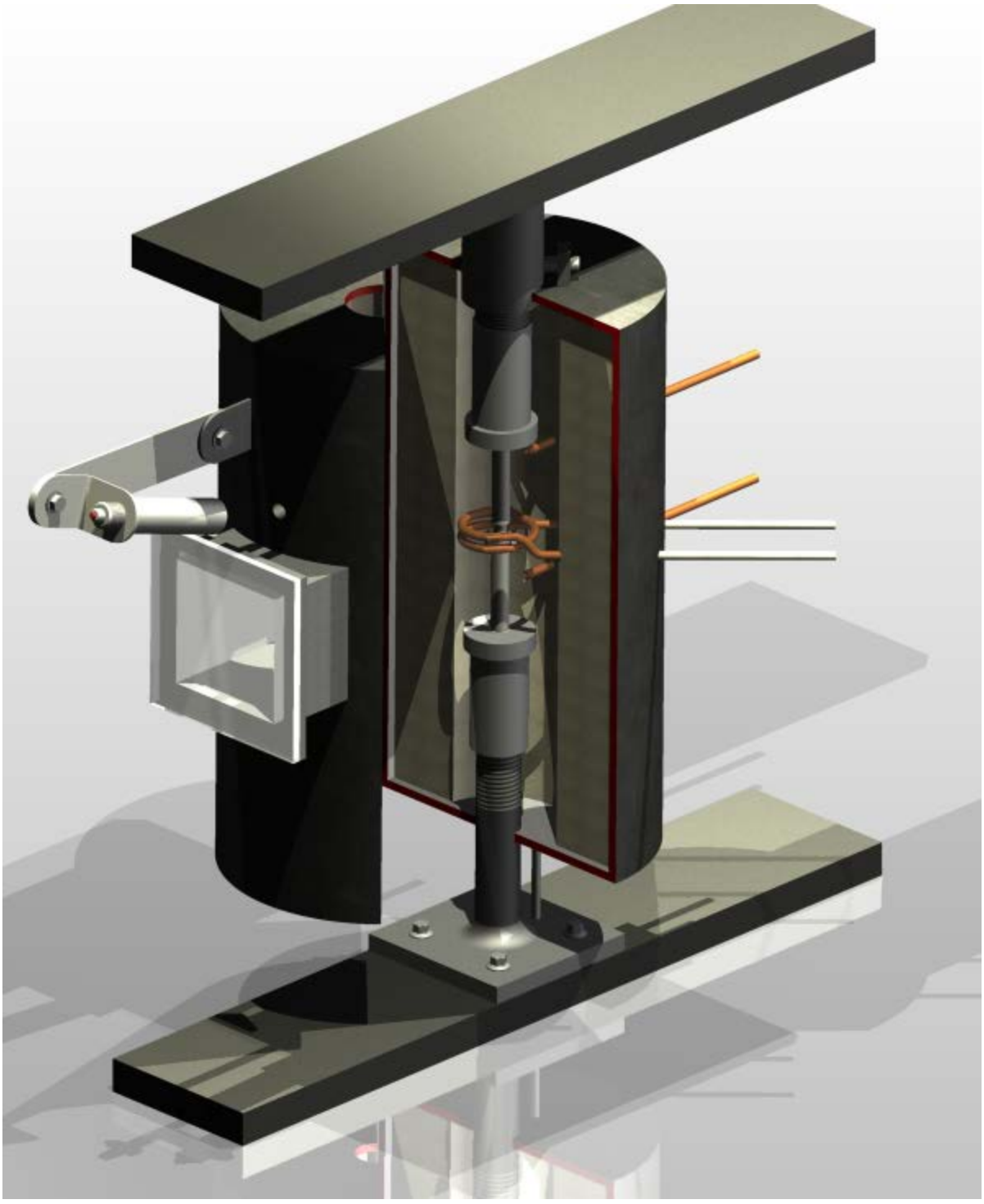

Figure 14: Heating chamber mounted on tensile frame (opened)

4.2.2 Experimental Control

A data recording and temperature control program was written in MATLAB in order to automate the experimental process. The program allows for closed-loop control of the thermal path. The user programs the desired thermal path in a stepwise fashion with each step consisting of a heating/cooling rate, aim temperature and holding time. On starting the automatic thermal control, the program begins reading and recording the optical pyrometer output at a rate of 1 s^{-1}. The temperature data are passed to a PID-based model (also written in MATLAB) that determines the proper 4-20 ma input to the induction power supply.

The temperature values read by the optical pyrometer were verified in an isolated experiment where the upper half of a tensile sample was drilled along its centerline in order to accommodate a thermocouple. The sample was heated in the testing apparatus and the temperature values from the thermocouple and optical pyrometer agreed (+/- 5˚C). The optical pyrometer values agree with the actual temperature only when the pyrometer is positioned at an angle where there was a direct line of sight to behind the induction coil and the pyrometer reading was at a maximum with respect to changes in position. During each actual experiment, the pyrometer was positioned to reach the maximum reading temperature prior to starting the automated thermal path.

During tension testing, the power to the induction coil is held constant in order to avoid potential temperature spikes due to thin layers of scale or crack formation during deformation. The crosshead speed is controlled by a separate computer connected to the Instron testing frame. This computer also records the load-displacement curve during deformation.

The heating chamber atmosphere was verified during an isolated experiment where the chamber was closed and argon was purged into the chamber at a low velocity. Oxygen measurements were taken in 5 minute intervals as shown in Table 6.

Table 6: Oxygen ppm for different argon purge times

Purge time (min)	Oxygen content (ppm)
5	1200
10	297
15+	<100

4.2.3 Testing Procedure

The tensile sample halves are placed into the grips with the upper half in a fixed position. The lower tensile half is given approximately 2 mm of vertical freedom in order to avoid the formation of any tensile stresses due to thermal contraction. The quartz crucible is placed on the shelf of the lower tensile half and a 12.7 mm diameter x 9.5 mm piece of filler is placed in the top of the crucible. This filler material is machined from the same metal as the tensile specimen. The filler metal is necessary to ensure complete filling of the crucible on melting.

The samples are positioned within 2 mm of one another and then the heating chamber is closed. The optical pyrometer is positioned to the approximately correct location using the laser dot sight which is aimed at the sample. The access port of the heating chamber is plugged and

argon is purged for 10 minutes minimum at a flow rate of 20 scfh prior to heating the sample. The argon flow rate is reduced to 10 scfh after this initial purge.

The sample is rapidly heated above the liquidus and the lower crosshead is raised until the liquid metal completely fills the melt crucible. The upper argon inlet is then closed to force the heat extraction mainly in the downward direction and allow the solidification front to move upward. This prevents the shrinkage cavity from forming within the deformation zone. The power input to the induction coil is manually decreased so as to achieve a cooling rate of approximately 0.05˚C/sec through solidification. The lower crosshead is incrementally raised in order to maintain a light compression on the sample and avoid formation of unwanted voids. The temperature values during this solidification step can only be treated as qualitative data due to the presence of the quartz crucible. On reaching a temperature reading of 1300˚C the upper argon inlet is turned on to avoid overheating of the upper tensile grips. On reaching a temperature reading of 1250˚C, the power is turned off completely and the crucible is broken away from the solidified tensile sample via the access port. The process of removing the crucible, from power off to power on, takes less than 30 seconds. The temperature drop during this time is severe, approximately 200˚C. However, because the sample remains in the austenitic range and due to the sluggish precipitation kinetics of AlN in austenite it is reasonable to assume that this brief low temperature period has little or no effect on the overall AlN precipitation.

Once the heating power has been switched back on the pyrometer is adjusted to give the maximum temperature reading, which corresponds to the correct sample temperature as noted in section 4.2.2. The induction coil control is immediately switched to automatic mode and the closed-loop control follows the desired thermal path. On reaching the testing temperature, the power input to the induction coil is set as constant to avoid potential fluctuations during the deformation. The load cell and displacement sensor are zeroed and then tension is applied to the

sample at a constant lower cross-head speed of 0.12 mm/sec until failure occurs. Immediately after failure occurs, the induction coil power is turned off and the sample is quenched via high-velocity helium jet.

4.2.4 Post-solidification Cooling Rate

Solidification modeling was performed using the commercially available software MAGMA. The data obtained from modeling were used in the design of solidification and thermal paths of the experiments in this work. The software was used to model the temperature profiles within the solidifying and cooling ingot after pouring. Figure 15 shows the cooling curves of the ingot at various depths from the surface for a 1750 mm diameter ingot.

At a depth of 150 mm from the surface, the post-solidification temperature profile from ~1400˚C to 600˚C was fitted with a linear profile giving a temperature drop of approximately 0.012˚C/sec as shown in Figure 16. Due to the longest experiment times being in excess of 16 hours at this rate, a cooling rate of 0.02˚C/sec was used to reduce the maximum experiment time to approximately 12 hours. This adjustment was necessary for safe operation of the 10kW induction coil which requires continuous supervision.

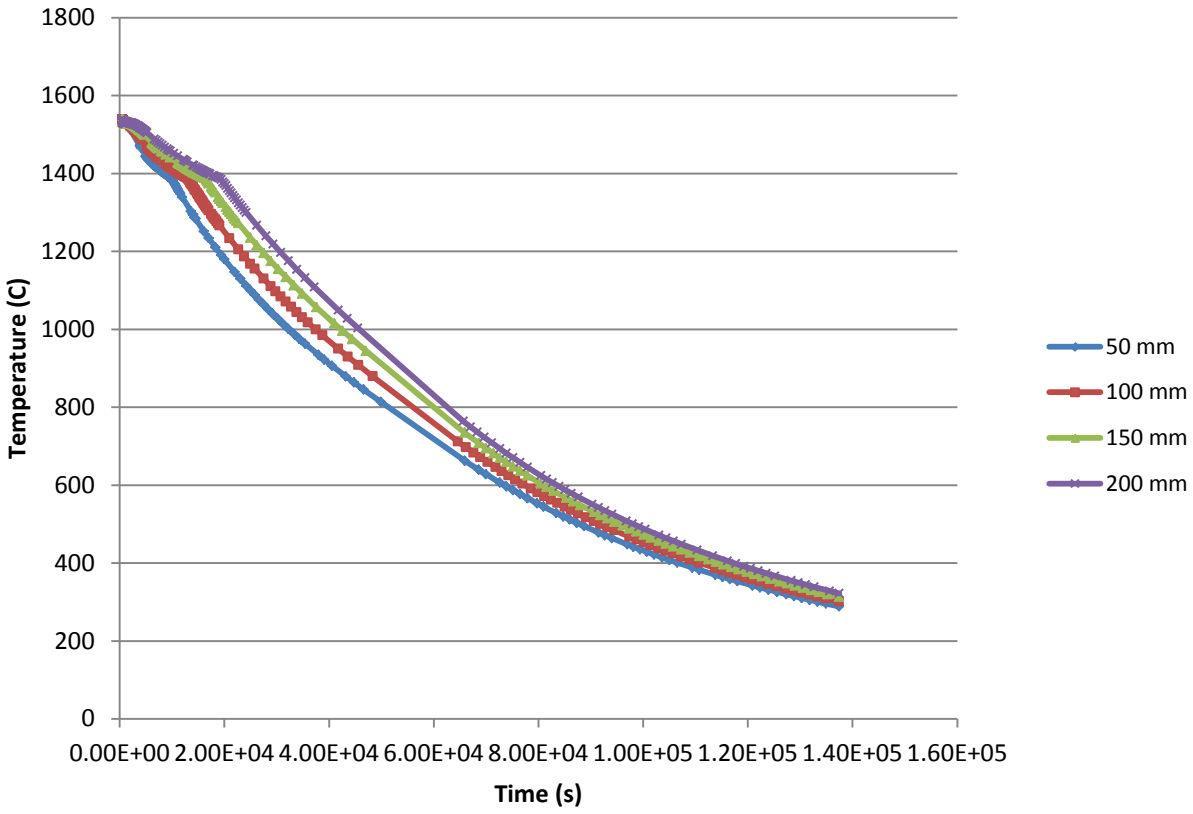

Figure 15: Cooling curves for 50mm – 200 mm distance from ingot surface

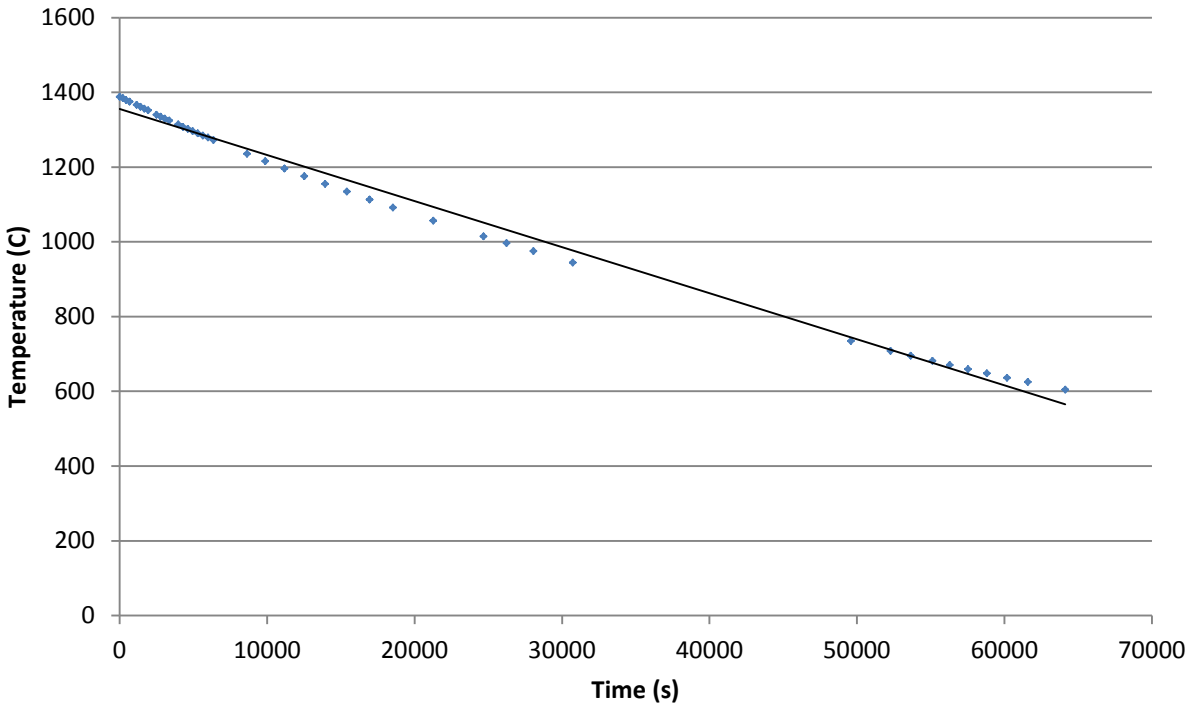

Figure 16: Linearized temperature drop at depth of 6" below ingot surface

4.2.5 Dilatometry

A Linseis L78 RITA dilatometer was used to develop full CCT diagrams for the P20 compositions steels A and C. 3 mm diam x 10 mm height cylindrical pins were machined from the same material as the stated P20 steel compositions. The samples were heated in a helium atmosphere to 1000°C and held for 15 minutes then cooled at various cooling rates to room temperature. The dilatometer records the pin temperature using a type K thermocouple welded to the sample. The pins were sectioned longitudinally after testing, mounted in thermoplastic compound and etched with 2% Nital to reveal the microstructure. The dilation versus

temperature data were used to identify the phase transformation temperatures which were then matched with the observed microstructures to develop the CCT diagram.

4.2.6 Metallurgical Analysis

Various techniques were employed in attempt to isolate the cause of the ductility trough:

- TEM thin foil
- TEM direct carbon extraction replica
- TEM indirect extraction replica
- Electrolytic dissolution with ICP analysis
- SEM
- Optical microscopy

Selected thin foil specimens from experimental and industrial material samples were prepared for TEM analysis. The samples were mounted in thermoplastic compound, ground, polished to 1 μm finish and etched in 2% nital until the as-cast microstructure was easily observed by the naked eye. This required approximately 1.5 minutes in lightly agitated etchant and then the samples were rinsed with alcohol. Slices of roughly 100 μm thickness were taken from the freshly etched surface. Three millimeter disks were punched from the slices at areas of interest (prior austenite grain boundaries) and the disks were manually ground to less than 70 μm thickness. Final thinning of the disks was accomplished by twin-jet using a solution of 1.25 liters acetic acid, 0.08 liters perchloric acid and 0.7 g chromic acid at 20 – 30 V. The disks were thinned and then rinsed thoroughly in ethanol. Several discs were not thinned by the jet-polishing technique and instead were dimpled using a Fischione Model 200 Dimpling Grinder and ion milled using a Fischione Model 1050.

Direct carbon extraction replicas were prepared for analysis by TEM. Selected samples were sectioned longitudinally from the limit of the melting zone to the fracture face and mounted in thermoplastic compound. Samples were then ground and polished with alcohol and alcohol-based lubricant in order to prevent dissolution of the AlN precipitates which are known to be water soluble[102]. The samples were etched in 2% nital until the as-cast microstructure was easily observed by the naked eye, approximately 1.5 minutes in lightly agitated etchant, and then rinsed with alcohol. Approximately 40 nm of carbon was evaporated onto the sample surfaces in a partially evacuated atmosphere. The carbon film was then scored into ~2 mm square sections and extraction of the precipitates was achieved by submerging in 8% nital until the carbon films were lifted from the surface. The carbon extraction replicas were then fished from the nital solution using a 300 mesh nickel grid, rinsed in ethanol and dried.

Direct extraction replicas were largely unsuccessful on the fracture surfaces due to the surface oxidation that occurred even in the protected atmosphere. One low ductility experiment was repeated with approximately ten times the typical argon flow rate in order to preserve the fracture surface. Direct extraction was successful on this sample. This procedure was identical to the previously described direct extraction process apart from the mounting, grinding, and polishing steps. This sample is identified as C-19.

Indirect extraction replicas were prepared from a newly ground, polished and etched surface on the same samples as those used for direct carbon extraction replicas. Acetone dissolvable paper was placed onto the acetone-wetted surface of the sample and allowed to dry. The paper was then removed from the sample and a thin layer of carbon was evaporated onto the surface of the paper which was in contact with the sample. The paper was cut into approximately 2 mm square sections and then dissolved in acetone to free the carbon replica. Replicas were rinsed in alcohol and fished onto 300 mesh nickel grids for TEM analysis.

TEM work was performed on a Tecnai G2 TEM. SEM analysis was performed using an ASPEX PSEM on both fracture surfaces and polished and etched (2% Nital) samples.

Electrolytic dissolution was performed on several samples following the method developed by Rothleutner[103]. This method preferentially dissolves the steel matrix while preserving precipitates such as AlN and V(C,N). The electrolyte was filtered after dissolution and then the filter was digested in acid. The two solutions (dissolved filter and remaining electrolyte) were analyzed for aluminum content via ICP analysis. The dissolution process was repeated one time for each sample without the step of digesting the filter in order to allow for TEM analysis of the extracted precipitates on 300 mesh Ni grids.

Optical microscopy and grain size measurements were performed on a Leica M80 stereoscope and Leica DM6M microscope with image analysis software. Electron Probe MicroAnalysis (EPMA) was performed using a JOEL JXA-8530F using NIST certified reference standard 1763a.

5.0 EMPIRICAL RESULTS

5.1 DIRECT COOLING TO TEST TEMPERATURE

The samples which were cooled directly to the testing temperature are intended to provide information about the ductility of the as-cast ingot during the solidification and cooling period, while in the ingot mold and shortly after removing the ingot from the mold. Samples of steels A, B, C and D were melted then cooled at a rate of 0.02˚C/s to the desired test temperature and then strain was applied until failure. Table 7 gives the sample ID, AlxN product and testing temperature for the samples that followed this thermal path. The thermal path is shown schematically in Figure 17. The ductility results are presented in Figure 18.

It must be noted that sample C-02, which was cooled to 1100°C after solidification and then tested, exhibited intergranular cracking approximately 7 mm below the final fracture surface as shown in Figure 19. The final fracture showed very high %RA but just outside of the induction coil, where the temperature is slightly lower, the sample partially failed in a low-ductility manner.

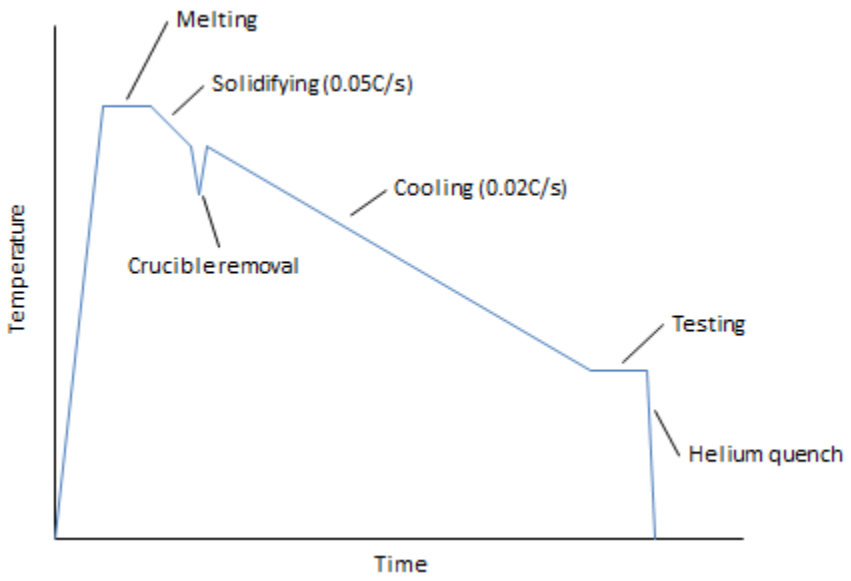

Figure 17: Thermal profile for direct cool to test temperature

Table 7: Samples following the direct cooling to test temperature thermal path

Sample	Test T (C)	%RA	AlxN ($x10^4$)	Sample	Test T (C)	%RA	AlxN ($x10^4$)
A-01	1200	98.5	0.6	C-01	1200	99.3	5.2
A-02	1100	95.0	0.6	C-02	1100	97.9	5.2
A-03	1000	96.4	0.6	C-03	1050	58.0	5.2
A-04	900	98.4	0.6	C-04	1000	8.0	5.2
A-05	800	77.1	0.6	C-05	950	11.0	5.2
A-06	700	50.2	0.6	C-06	900	68.3	5.2
A-07	650	76.6	0.6	C-07	800	66.6	5.2
B-01	1100	99.1	1.3	C-08	700	47.4	5.2
B-02	1000	97.3	1.3	C-09	650	60.2	5.2
B-03	900	86.7	1.3	D-01	1100	98.7	1.2
B-04	800	66.7	1.3	D-02	1000	82.5	1.2
B-05	700	50.6	1.3	D-03	900	79.2	1.2
				D-04	800	72.2	1.2
				D-05	700	60.1	1.2

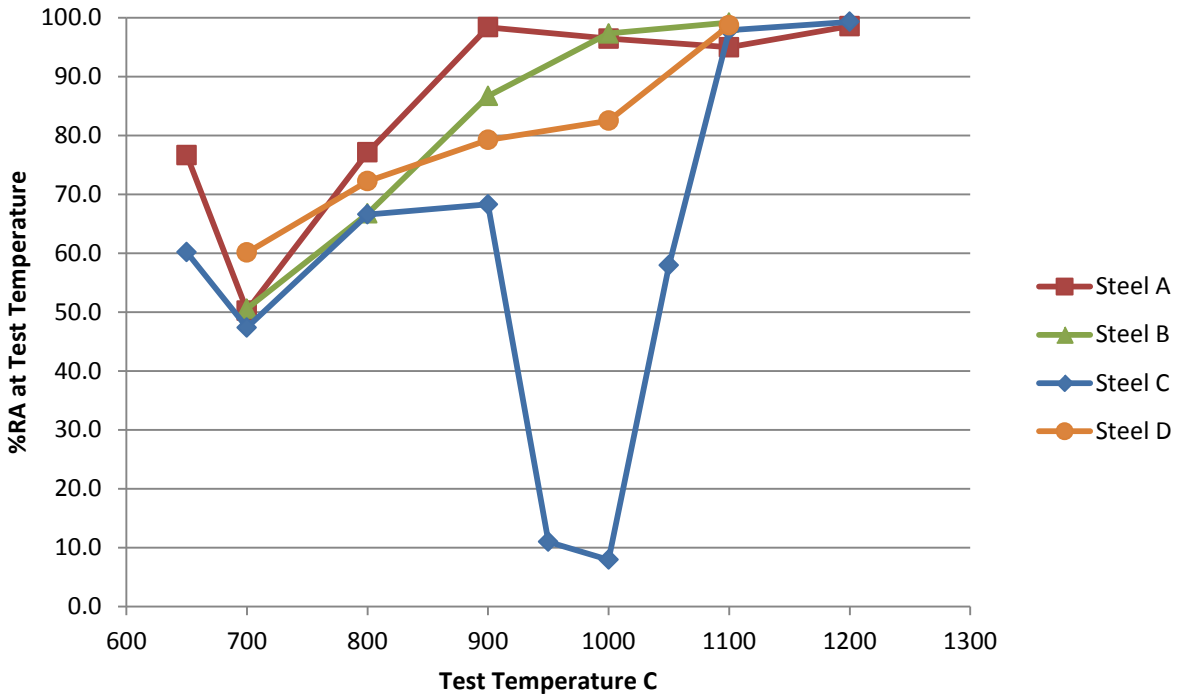

Figure 18: %RA vs test temperature for direct cooling to test temperature thermal path

Figure 19: Stereoscope image of intergranular fracture below final failure, steel C

5.2 UNDERCOOLING TO VARIED TEMPERATURE

The undercooling experiments are intended to provide information on the ductility of the as cast ingot which is being heated to forging temperatures. The varied undercooling temperatures correspond to different "track times" that may be experienced in industry. For these tests, the samples were melted and then cooled at 0.02˚C/s to the desired undercooling temperature and then reheated at 0.2˚C/s to 1000˚C and tested. The samples with the undercooling temperature listed at 300˚C were cooled at a rate of 0.02˚C/s to 680˚C and then the power supply to the induction coil was removed. The minimum controllable temperature of the experimental setup is approximately 680˚C so cooling below this temperature at a controlled rate was not possible. The value of 300˚C for the lowest temperature samples is for representation purposes only. The actual temperature was not measured but the sample was allowed to fully transform. Full transformation was ensured by monitoring the load cell readout; heating to 1000˚C was not started until 10 minutes at constant load was achieved.

The thermal path for the undercooling experiments is shown in Figure 20. Table 8 gives the sample ID's, Min T (undercooling temperature), %RA and [Al][N] product for the samples tested. Figure 21 shows the ductility results graphically for the undercooling experiment.

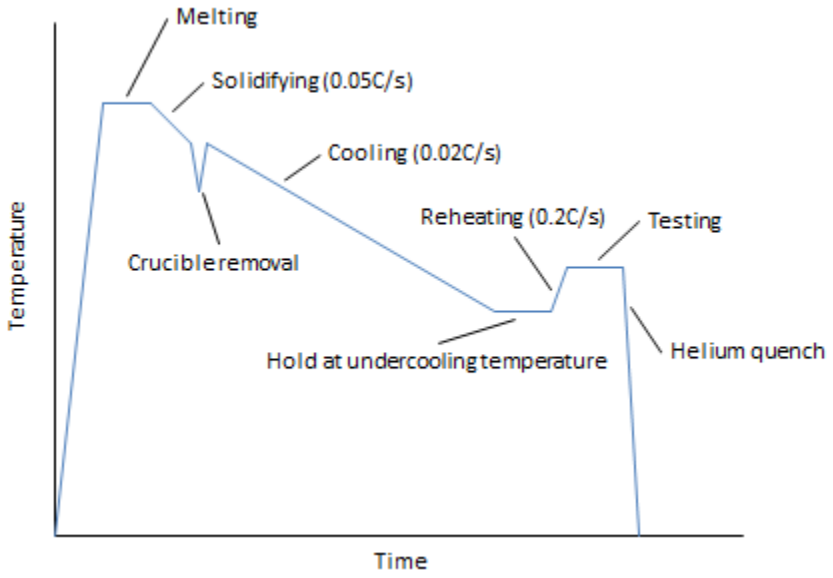

Figure 20: Thermal profile for undercooling to varied temperature tests

Table 8: Samples following undercooling to varied temperature thermal path

Sample	Min T	%RA	AlxN ($x10^4$)
A-11	300	95.9	0.6
A-10	700	94.2	0.6
A-09	800	22.6	0.6
A-08	900	12.2	0.6
A-03	1000	96.4	0.6
B-09	300	96.7	1.3
B-08	700	96.5	1.3
B-07	800	12.7	1.3
B-06	900	0.0	1.3
B-02	1000	97.3	1.3
C-13	300	95.1	5.2
C-12	700	89.7	5.2
C-11	800	98.0	5.2
C-10	900	0.0	5.2
C-04	1000	8.0	5.2

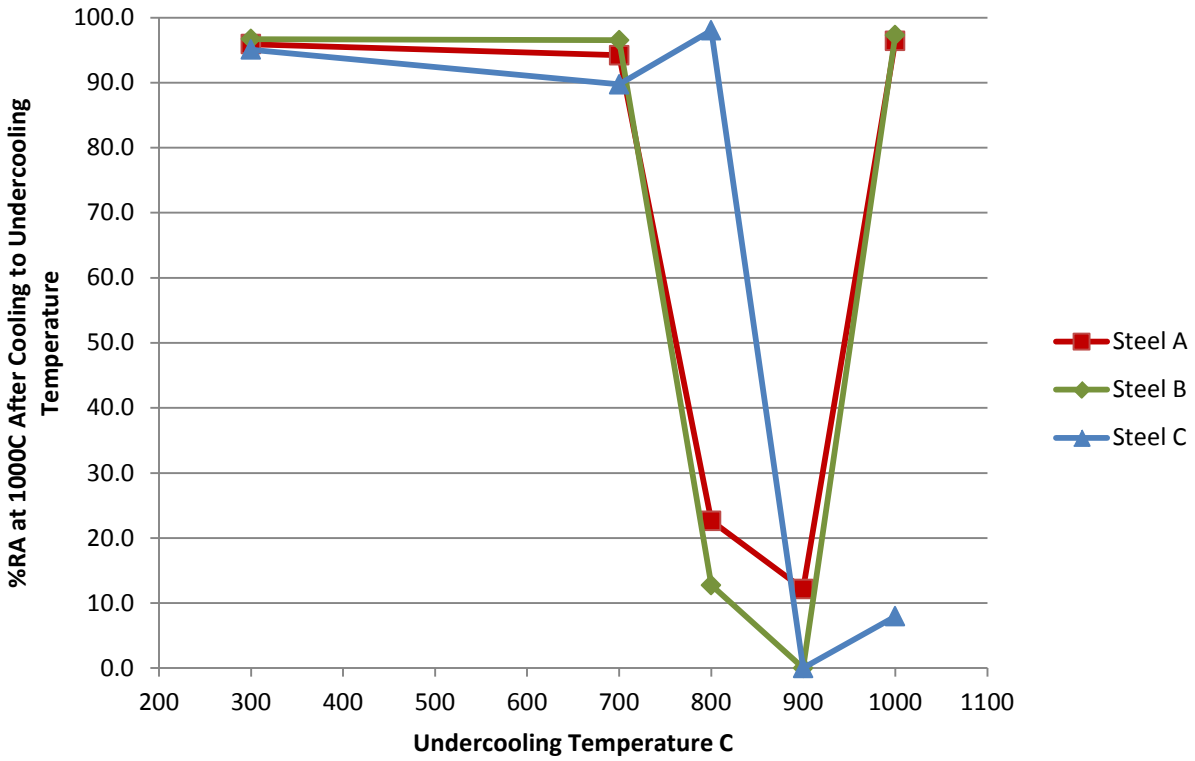

Figure 21: %RA at 1000C for undercooling to varied temperature thermal path

5.3 VARIED UNDERCOOLING HOLD TIME

The excellent ductility of steel C tested after undercooling to 800°C and the poor ductility of steels A, B and C after undercooling to 900°C prompted further investigation. For this reason, samples were tested at 1000˚C after various hold time at 900˚C in order to examine the change in ductility as a function of hold time. The thermal path is identical to that shown in Figure 20, with varied hold times at the undercooling temperature. Table 9 gives the sample ID's, hold time at 900°C, %RA and [Al][N] product for the samples tested. Figure 22 shows the results graphically.

Table 9: Samples following varied undercooling hold time at 900C thermal path

Sample	Hold time	%RA	AlxN ($x10^4$)
A-08	240	12.2	0.6
A-12	1000	31.3	0.6
A-13	2500	56.7	0.6
A-14	5500	79.0	0.6
B-06	240	0.0	1.3
B-10	500	50.9	1.3
B-11	1000	62.8	1.3
B-12	2500	73.8	1.3
B-13	5500	96.8	1.3
C-10	240	0.0	5.2
C-14	500	91.1	5.2
C-15	1000	94.5	5.2
C-16	2500	94.8	5.2
C-17	5500	98.3	5.2

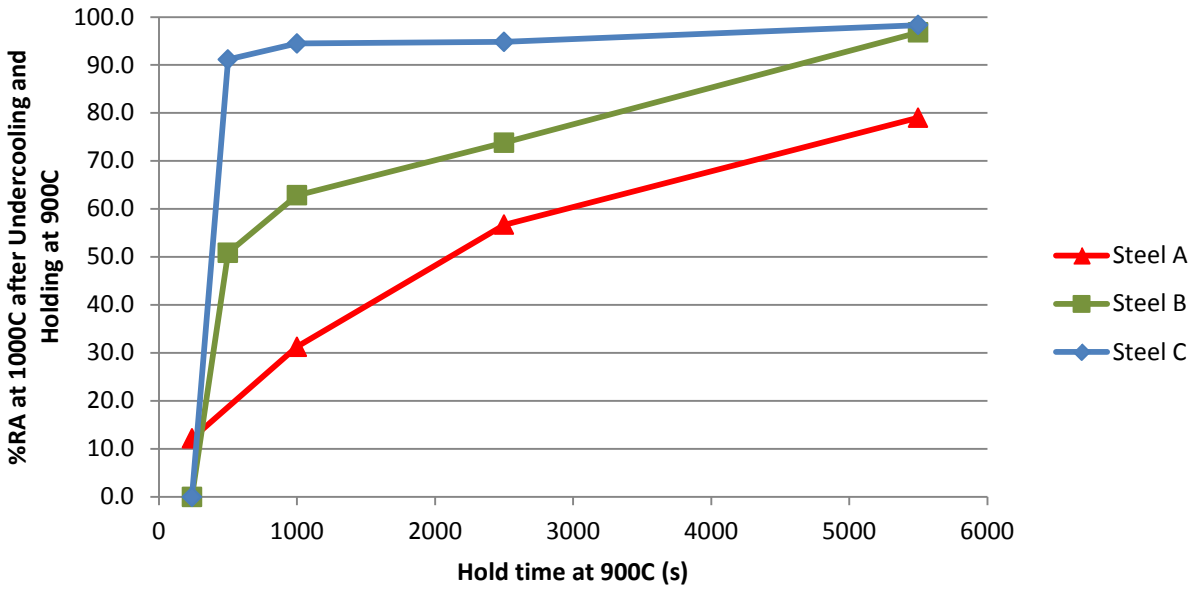

Figure 22: %RA at 1000°C after varied hold time at 900°C undercooling

5.4 THERMAL STRAIN

The thermal strain experiments were carried out in order to allow examination of a much lower strain rate than is attainable using the Instron testing frame. Samples were melted and solidified in the same manner as listed in section 4.2.3. Upon reheating after removal of the crucible, the 2 mm vertical freedom of the bottom tensile half was removed by moving the lower crosshead downward until a load of approximately 100 lb. was achieved. Stress relaxation occurred within 2 minutes and then the load cell was zeroed. The samples were then cooled at the typical value of 0.02˚C/sec to 700˚C. Load cell readings were recorded during the cooling process. Once reaching 700˚C the load due to thermal contraction was relieved by moving the lower crosshead upward and then the sample was quenched with a helium jet. Figure 23 shows the temperature versus load curves for these tests.

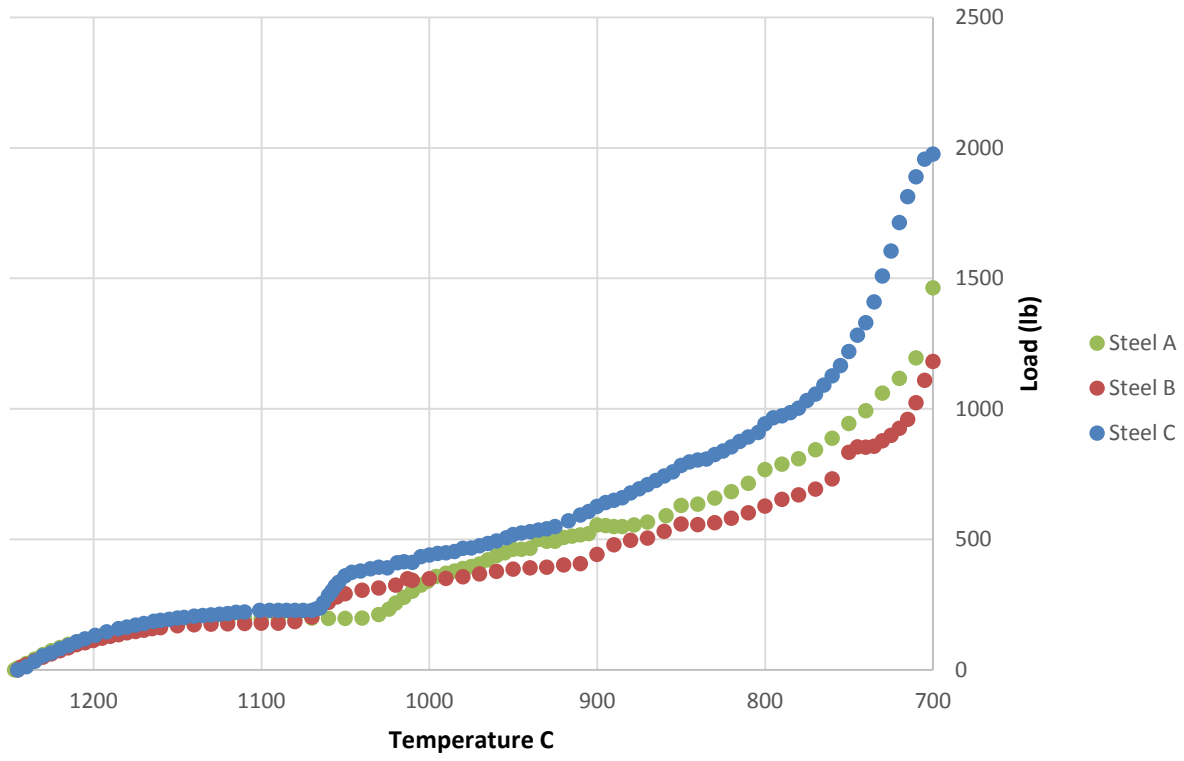

Figure 23: Measured load versus temperature for thermal strain experiments

5.5 ADDITIONAL THERMAL PATHS

Several experiments were performed where the sample was in-situ solidified and then followed a specific thermal path in order to provide additional information about the microstructural state of the material either prior to or during deformation. The thermal handling and deformation details for these samples are listed individually below.

- Sample B-14
    - In-situ solidified and cooled to 1050°C following the thermal path of Figure 17
    - Quenched immediately with helium jet, no deformation applied

- Sample C-18
    - In-situ solidified and cooled to 650°C following the thermal path of Figure 17
    - Isothermal hold at 650°C for 6 hours in order to allow for grain boundary precipitation
    - No deformation applied
- Sample C-19
    - In-situ solidified and cooled to 1000°C following the thermal path of Figure 17
    - Argon flow rate increased to ten times that used in previous experiments
    - Repeat test of sample C-04 with increased argon flow rate to preserve fracture surface
    - RA = 10%
- Sample C-20
    - In-situ solidified and undercooled to 900°C following the thermal path of Figure 20
    - Hold at 900°C for 240 seconds before reheating to 1100°C and testing
    - RA = 96.2%
- Sample C-21
    - In-situ solidified and cooled to 1050°C following the thermal path of Figure 17
    - Quenched immediately with helium jet, no deformation applied

5.6 DILATOMETRY

Figure 24 shows the CCT diagrams for steels A and C. Dilatometry results showed that increasing the Al and N content accelerated the transformation of austenite to ferrite/pearlite during continuous cooling and increases the precipitation start temperature. The transformation of austenite to bainite at faster cooling rates is suppressed for steel C. The Ar_3 temperature is shown to be 794°C at the slowest cooling rate tested. This value is higher than the Ae_3 of 767°C that can be calculated from the information in section 2.3.1.

The microstructures of the two steels examined show many similarities for several of the cooling rates but also some significant differences. Figures 25 and 26 show the microstructures of the two steels after cooling at a rate of 0.5°C/min. The volume fraction of proeutectoid ferrite is much higher in steel C. The prior austenite grain sizes appear slightly larger in steel A due to discontinuous grain growth. In both steels there is a large amount of upper bainite along with the ferrite.

Figures 27 and 28 show the two steels after cooling at 1.0°C/min. Both steels begin to transform to pearlite in place of proeutectoid ferrite at this cooling rate, with a higher volume fraction of pearlite formation in steel C. Some small amount of proeutectoid ferrite remains as shown in Figure 29. At a cooling rate of 1.8°C/min the microstructures of steels A and C change significantly as shown in Figures 30 and 31. The bainite that forms in both steels etches lightly and small areas of pearlite are present within the bainite. There are many fine pearlite islands in steel A. Steel C does not exhibit the very fine pearlite islands, instead most of the pearlite is present in larger islands. Figure 32 shows a higher magnification view of the dark etching areas of steel C, confirming that the areas are pearlite islands rather than contamination.

The formation of martensite and bainite at faster cooling rates are of no consequence in the present work where slow cooling rates were used to approximate that of large cross-section ingots. For completeness, Figures 33 and 34 show the microstructures present in steels A and C after cooling at a rate of 20°C/min. Steel A contains a small amount of bainite however both steels transformed primarily to martensite at this cooling rate. Segregation banding is visible in Figure 34.

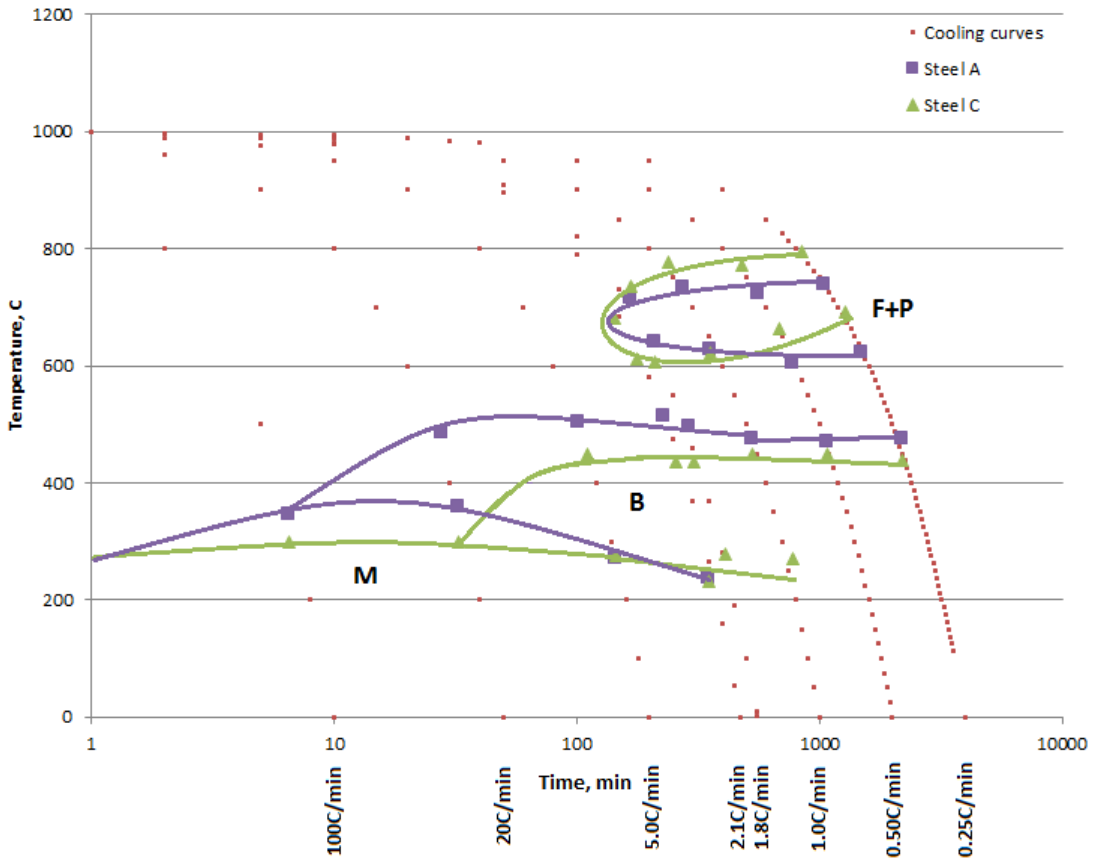

Figure 24: CCT diagrams for steels A (low Al,N) and C (high Al,N), dilatometer results

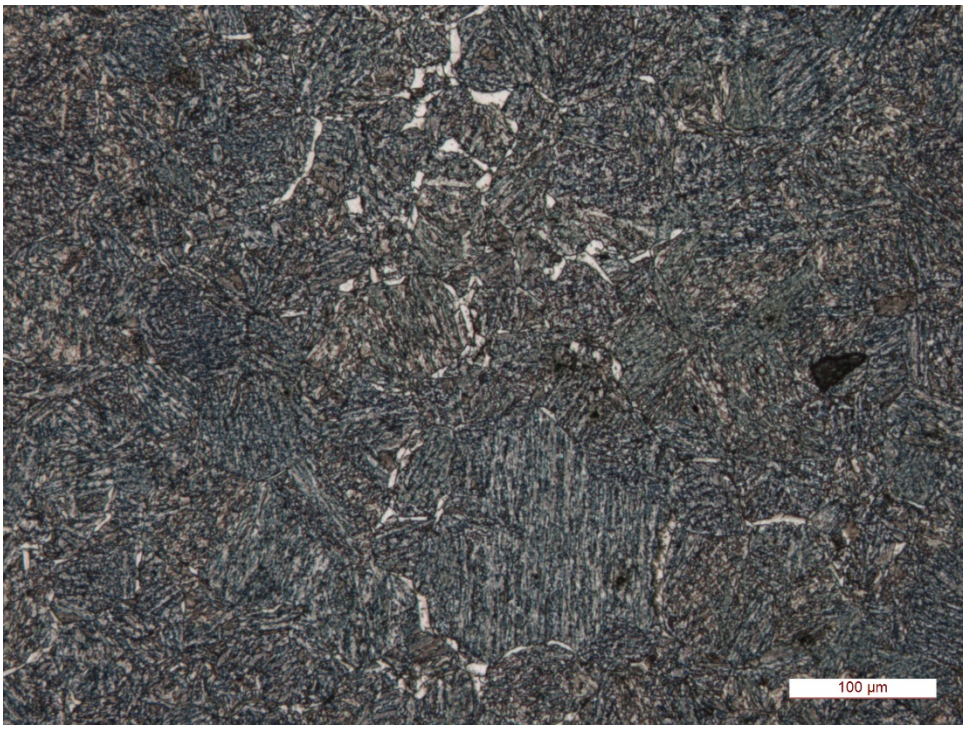

Figure 25: OM image of steel A at 0.5°C/min cooling rate, 2% nital

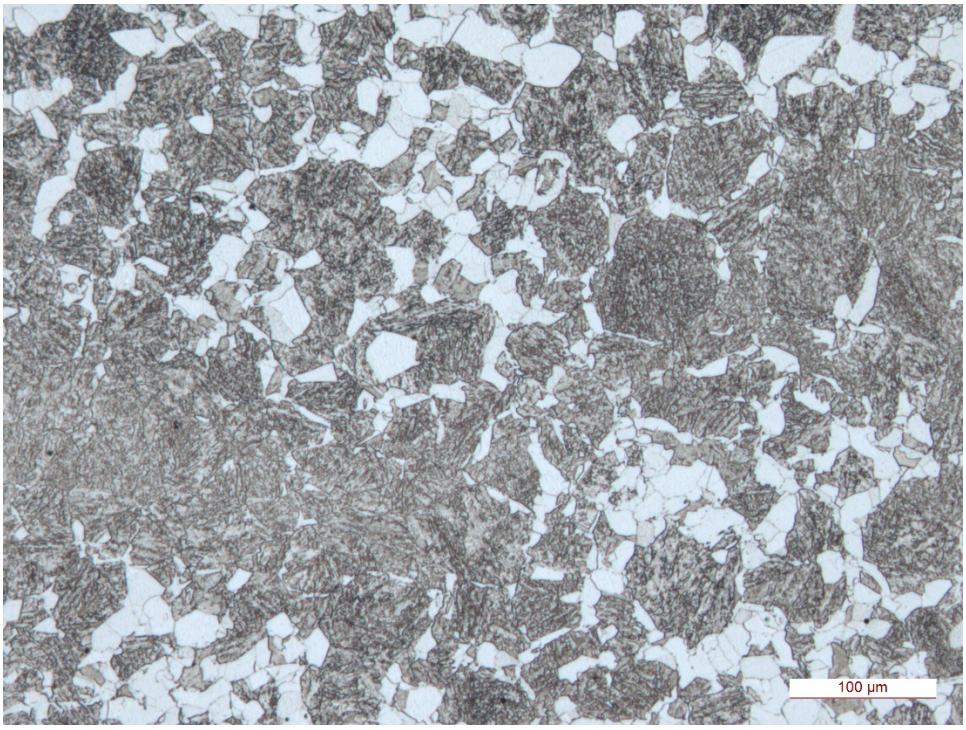

Figure 26: OM image of steel C at 0.5°C/min cooling rate, 2% nital

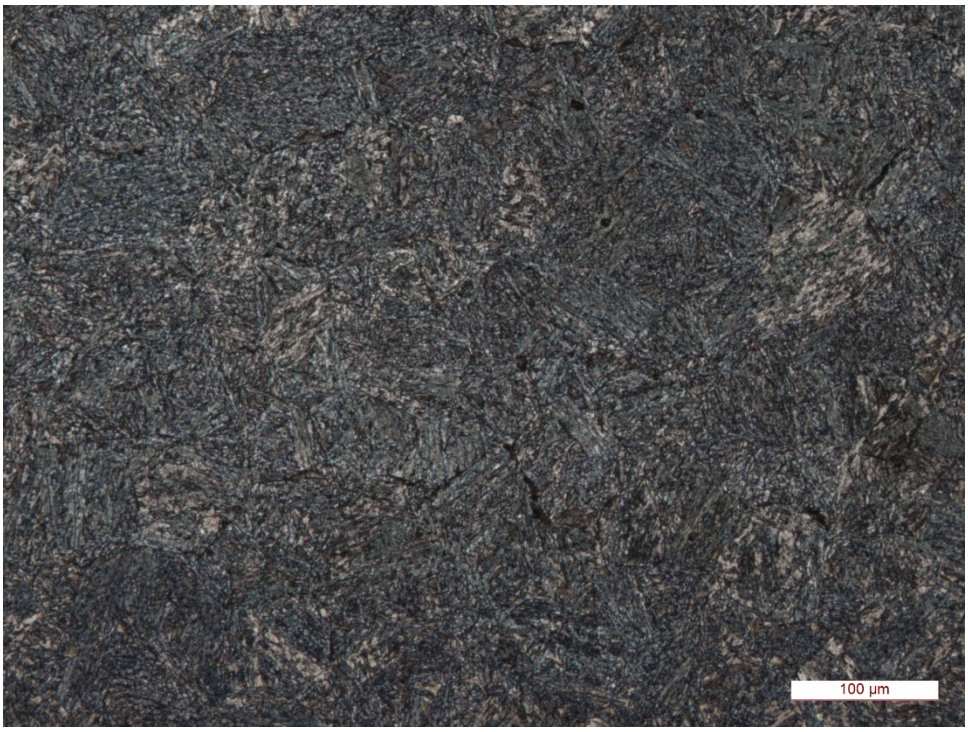

Figure 27: OM image of steel A at 1.0°C/min cooling rate, 2% nital

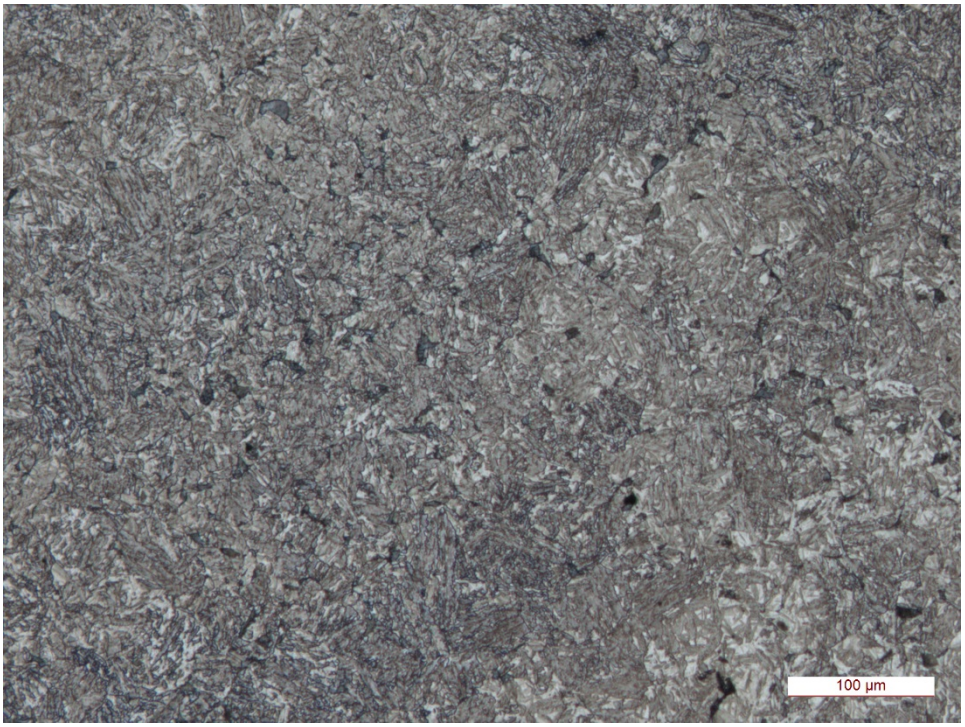

Figure 28: OM image of steel C at 0.5°C/min cooling rate, 2% nital

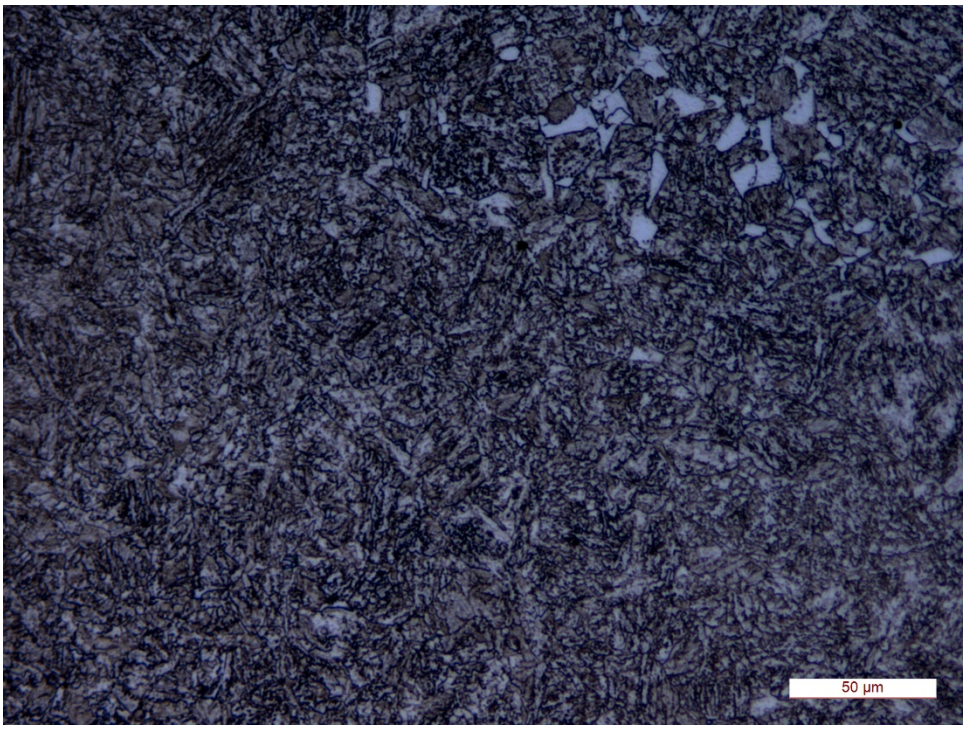

Figure 29: OM image of steel C ferrite precipitation at 0.5°C/min cooling rate, 2% nital

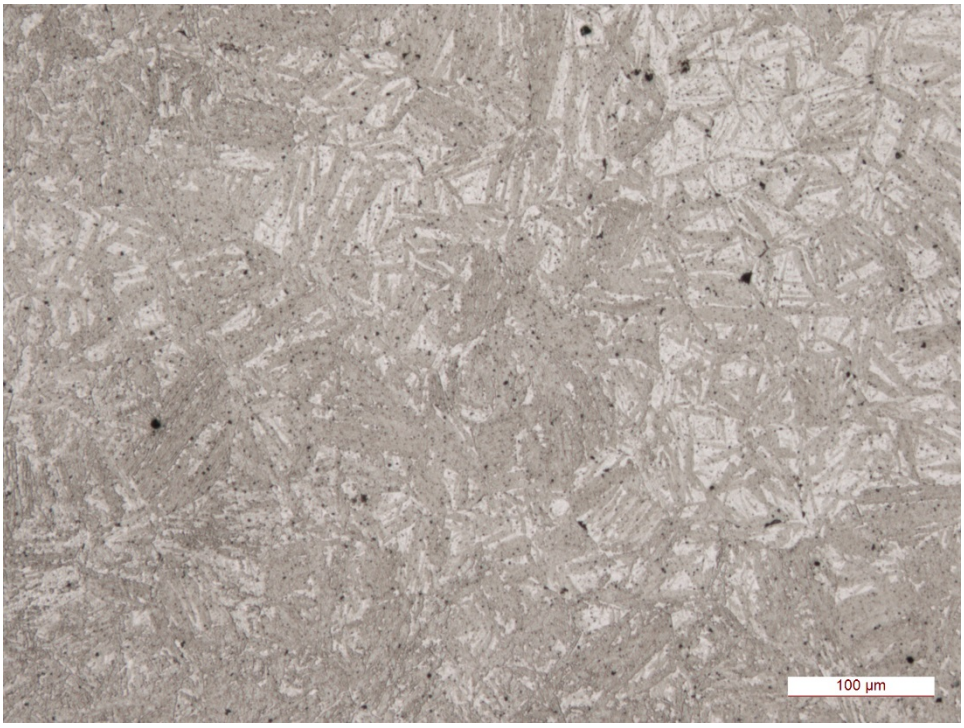

Figure 30: OM image of steel A at 1.8°C/min cooling rate, 2% nital

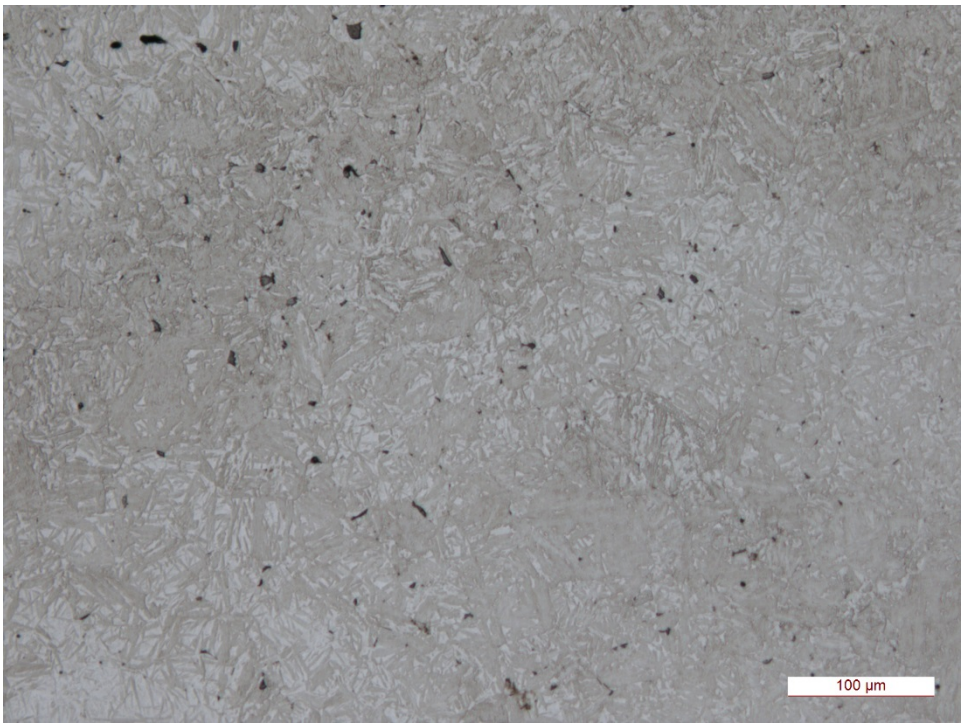

Figure 31: OM image of steel C at 1.8 °C/min cooling rate, 2% nital

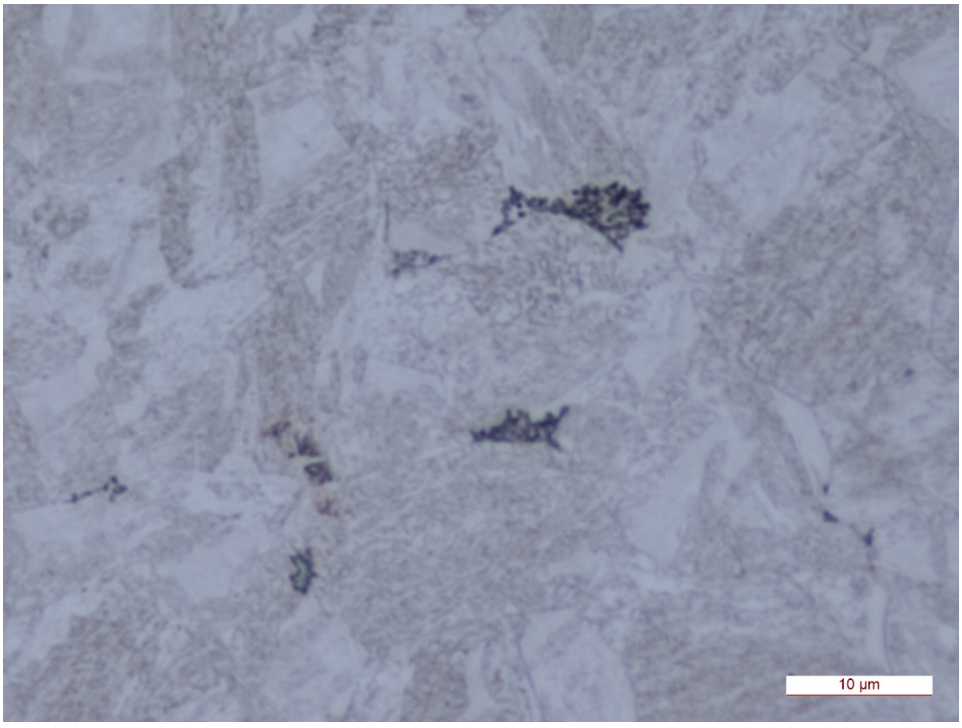

Figure 32: OM image of steel C showing pearlite at 1.8°C/min cooling rate, 2% nital

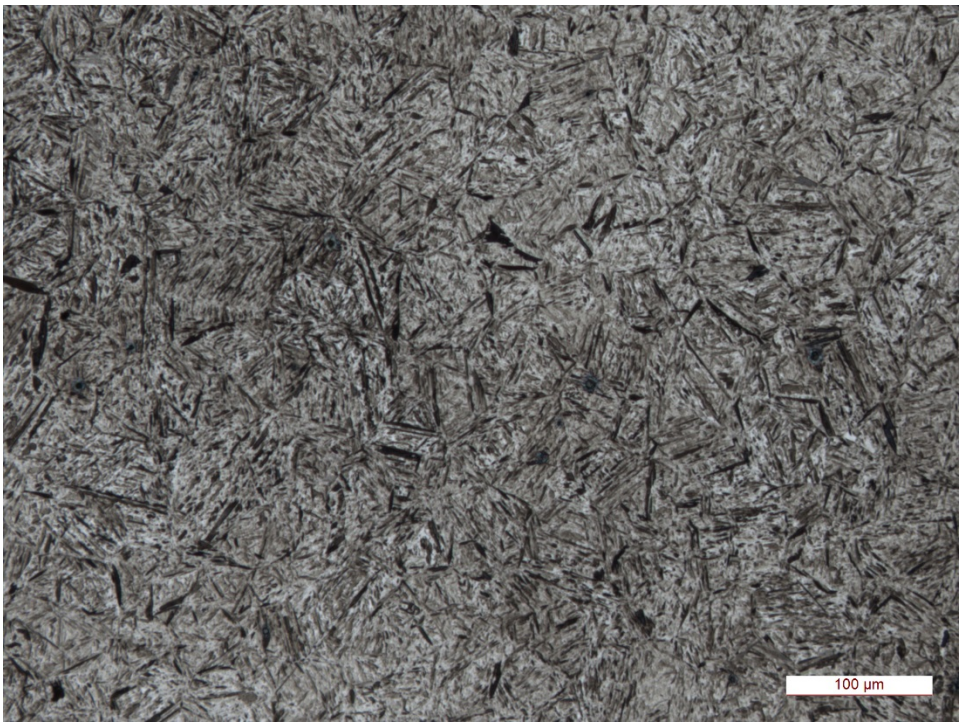

Figure 33: OM image of steel A at 20°C/min cooling rate, 2% nital

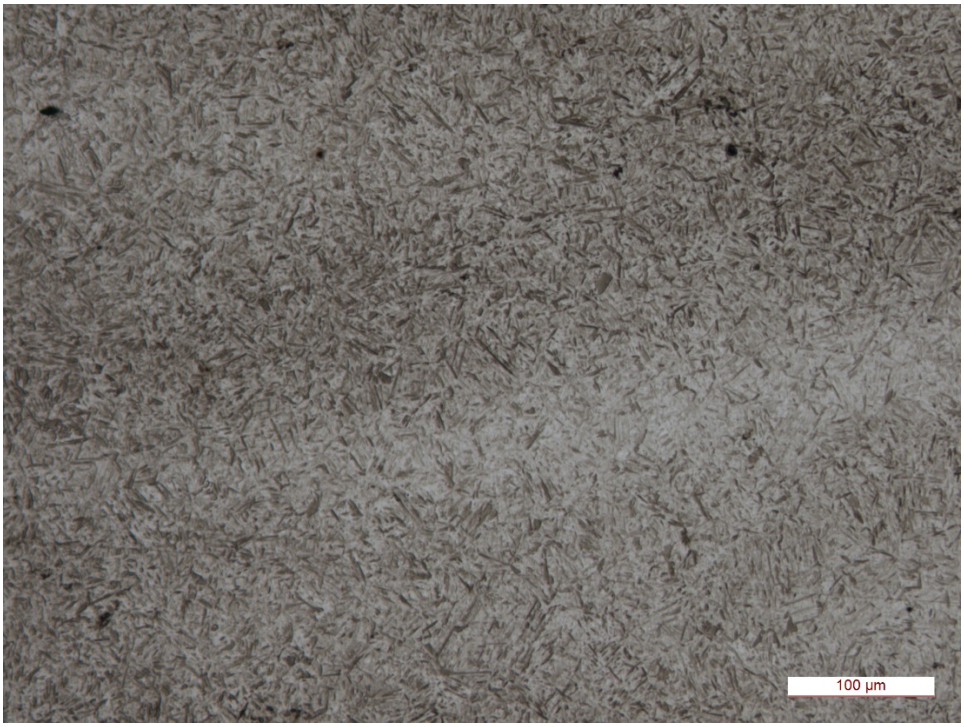

Figure 34: OM image of steel C at 20°C/min cooling rate, 2% nital

5.7 GRAIN SIZE MEASUREMENTS

Grain size measurements were performed on the samples that were used for the thermal strain experiments due to the very small amount of deformation in these samples. There were no signs of dynamic recrystallization in the samples and therefore they are considered a good representation of the as-cast austenite grain size. The prior austenite grains are readily visible without any special preparation techniques due to the as-cast structure.

It was found that the as-solidified structure was coarsened with increased aluminum, as noted in the work by Ericson[104]. A similar effect was found by Torkar[105]. This effect was attributed to an increase in the difference between the liquidus and solidus temperatures when the aluminum content was higher in Ericson's work. The larger difference between liquidus and solidus temperatures implies that there is additional time for dendrite growth during solidification, leading to the larger as-cast grain size. The grain size did not coarsen when increasing the aluminum content from 0.008 wt% (steel A) to 0.015 wt% (steel B). However, steel C showed approximately two times larger an as-cast grain size with the aluminum content of 0.040 wt%. In all cases the total analyzed area was 44.5 mm^2. The large as-cast grain sizes are more readily described in terms of average grain area rather than ASTM grain size; these results are shown in Table 10. Figures 35 - 37 show the micrographs and binary image analyses used to produce the grain size analysis by the Leica software using ASTM method E112.

Individual grain measurements were made of the major and minor grain dimensions (longest and shortest boundary-to-boundary measurement through the approximate mid-point of the grain) of 104 representative grains from 24 samples. The samples were divided evenly among steels A, B and C (eight samples each). The deformation zone was not included in the analyzed area in order to avoid measurement of recrystallized grains. Figure 38 shows an

example of the grain measurements from sample C-04. Table 11 shows the average measured dimension of all grains for steels A, B and C. The results are in good qualitative agreement with those produced using the Leica software with ASTM method E112.

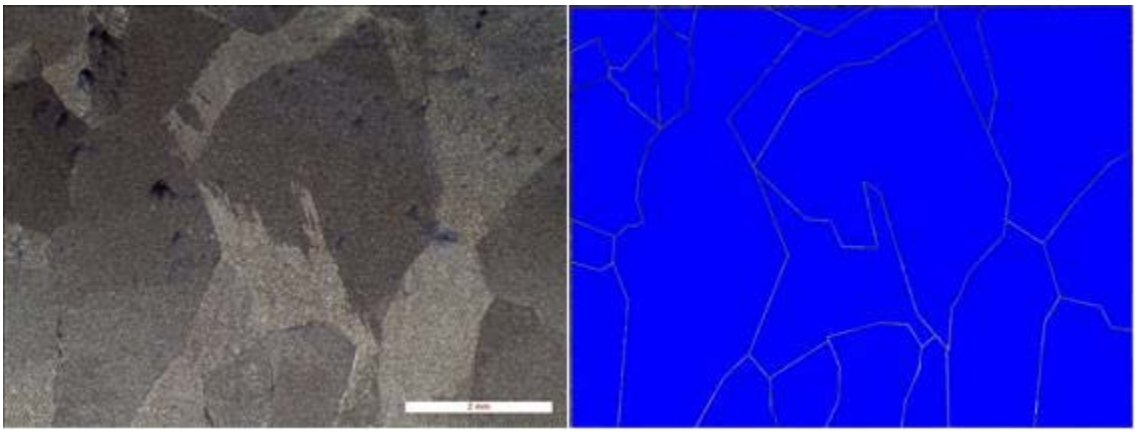

Figure 35: Steel A, 2% nital etch and binary grain boundary image

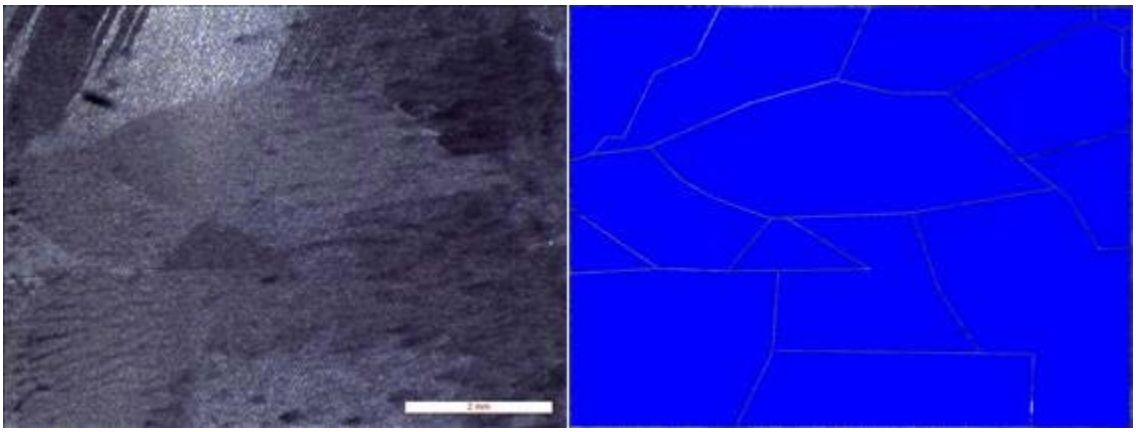

Figure 36: Steel B, 2% nital etch and binary grain boundary image

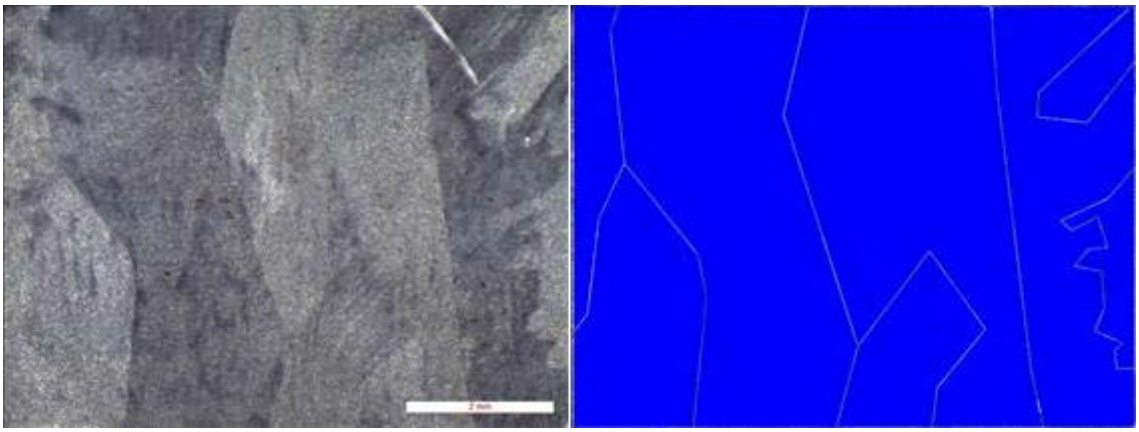

Figure 37: Steel C, 2% nital etch and binary grain boundary image

Table 10: Grain size analysis for steels A, B and C

Steel	**A**	**B**	**C**
Analyzed area mm^2	44.5	44.5	44.5
ASTM grain size	-4.5	-4.5	-5.8
Mean grain area mm^2	3.015	3.015	7.296
Mean linear intercept mm	1.547	1.547	2.406

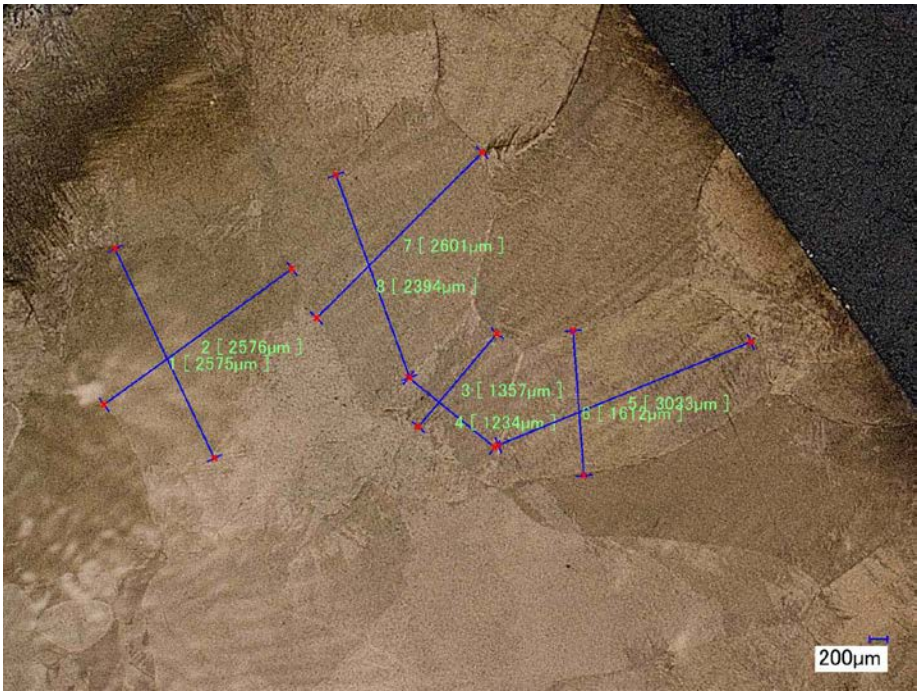

Figure 38: Example of grain dimension measurements, sample C-04

Table 11: Results of grain dimension measurements

Steel	Average measured grain dimension, µm
A	1651
B	1752
C	2432

6.0 RESULTS OF METALLURGICAL ANALYSES

6.1 GENERAL FRACTURE ANALYSIS

There were two fracture mechanisms present in the samples studied: microvoid coalescence and intergranular failure. The area fraction intergranular failure correlated inversely to the reduction in area. Samples which failed in a brittle manner showed nearly 100% intergranular fracture. Figure 39 is an example of such a fracture surface and the large, as-cast prior austenite grains are apparent. Mixed intergranular and microvoid coalescence fractures appeared in samples with a reduction of area in the range of 20 – 60% as depicted in Figure 40. Samples with high reduction of area, greater than 60%, exhibited only microvoid coalescence as shown in Figure 41.

Polished faces of the samples, perpendicular to the tension direction, revealed various grain structures depending on thermal path and composition. The melted/unmelted interface was clearly visible in all samples due to the fine-grained structure in the unmelted areas as shown in Figure 42. During quenching, the austenite phase is transformed into martensite for all samples quenched from above the Ar_3 temperature.

SEM analysis of the low ductility fracture surfaces showed thin films at or near many of the prior austenite grain boundaries. The film contained elevated levels of Cr, Mo, P and C compared to the matrix. Figures 43 and 44 are progressively higher magnification of the fractured prior austenite grain boundary from sample C-10 (0.0% RA). The magnified areas are

highlighted. Figure 45 shows the EDS analysis of the matrix area and Figure 46 shows the EDS analysis of the thin film. The PAGB segregation film was also present on low ductility samples from steels A and B, but to a lesser degree. SEM-EDS elemental maps of the PAGB intergranular fracture from samples A-08 and B-06 (undercooled to 900°C, reheated to 1000°C and tested) both exhibited some degree of grain boundary segregation on the fracture surface as shown in Figures 47 and 48. The segregation of Mo, Cr and P to the austenite boundaries is clear for sample B-06. The EDS map showed very little segregation of chromium in sample A-08, but Mo and P segregation was found. The minimal Cr segregation in sample A-08 was confirmed by EDS spot analysis of both the film and matrix, see Figures 49 and 50.

One grain from sample C-10 was able to be forced out of the fracture surface due to the severe grain boundary separation near the fracture surface of this sample. The underside of the removed grain was examined by SEM-EDS and exhibited fine V(C,N) precipitation within the thin film that adhered to the removed grain. The V(C,N) precipitates contained a significant amount of molybdenum and were less than 1 μm in size as shown in Figure 51. Some areas were free of the thin film and slip bands due to deformation were clearly visible as shown in Figure 52, the highlighted area shows the thin film.

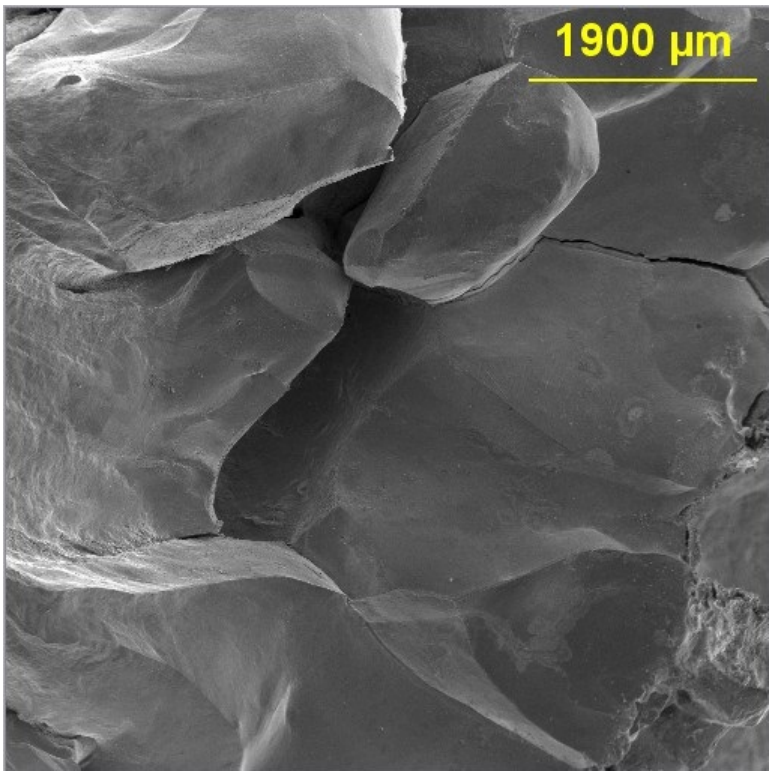

Figure 39: Intergranular fracture of sample C-10, RA = 0%

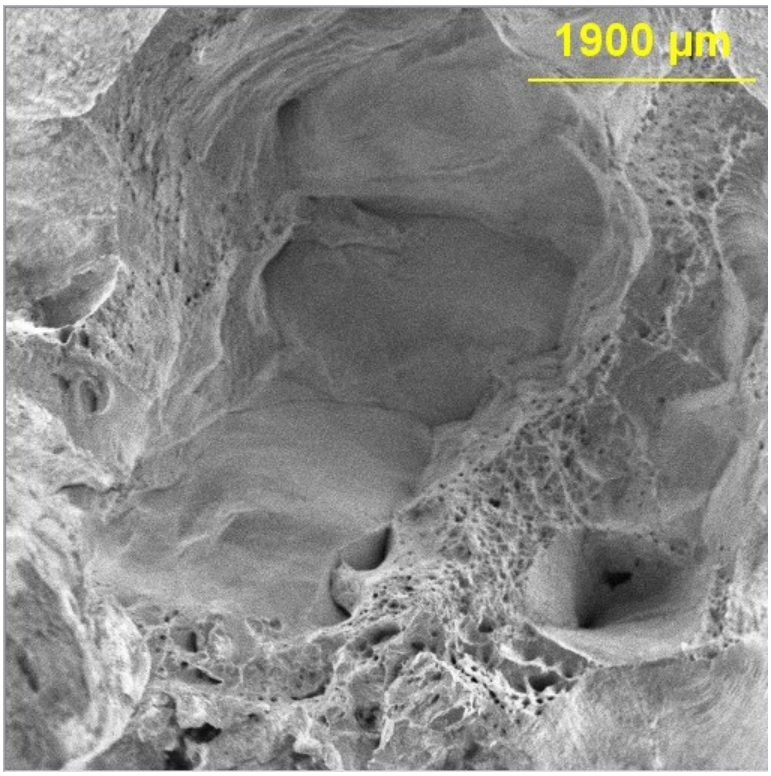

Figure 40: Mixed intergranular and microvoid coalescence, sample B-10, RA = 50.9%

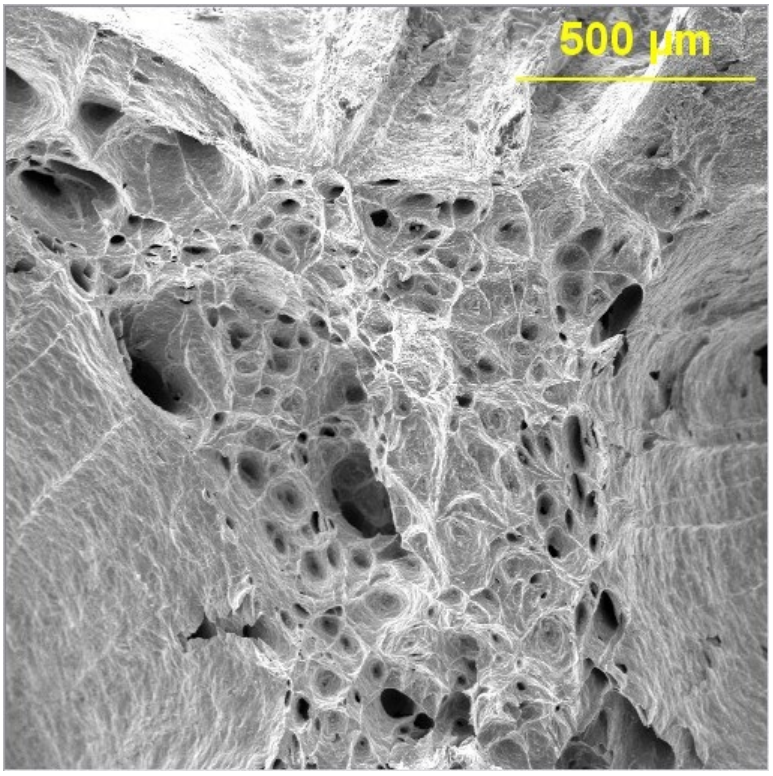

Figure 41: Microvoid coalescence in sample C-06, RA = 68.3%

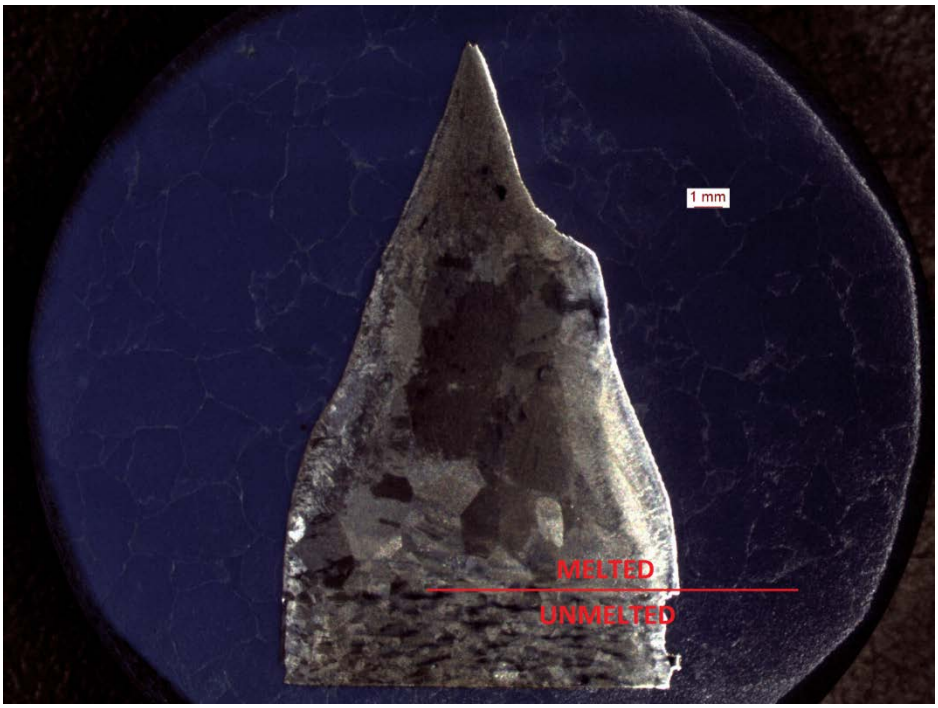

Figure 42: Melted/unmelted interface in bottom-half of broken sample C-14, %RA = 91.1

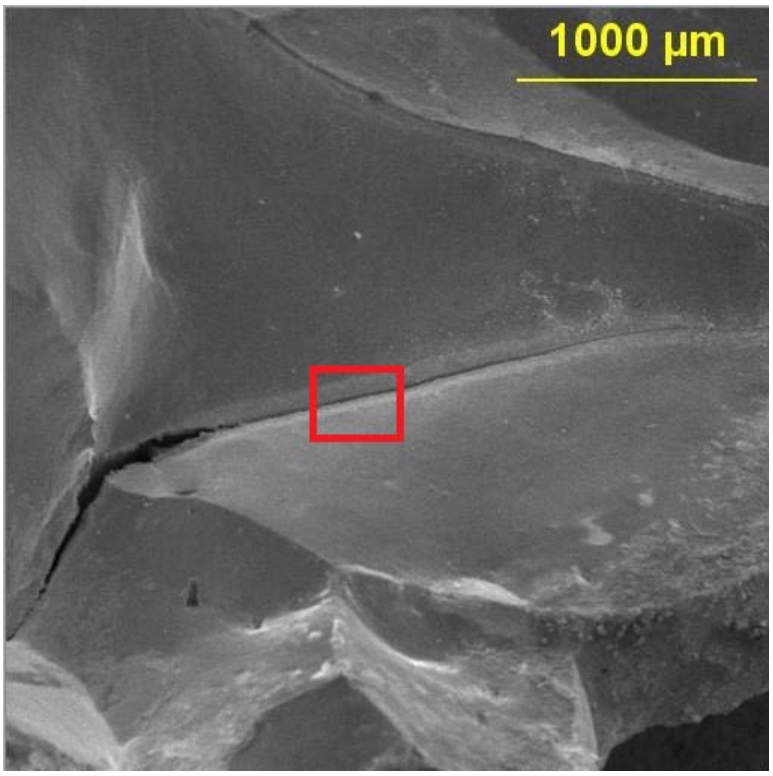

Figure 43: SEM image of PAGB fracture, sample C-10

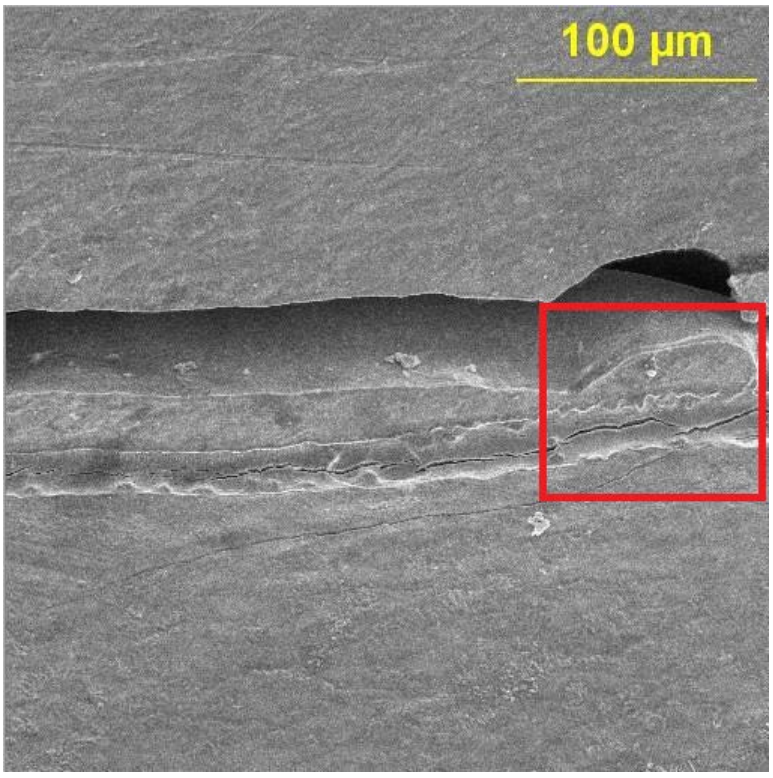

Figure 44: SEM image of segregated film from highligted area of Figure 43

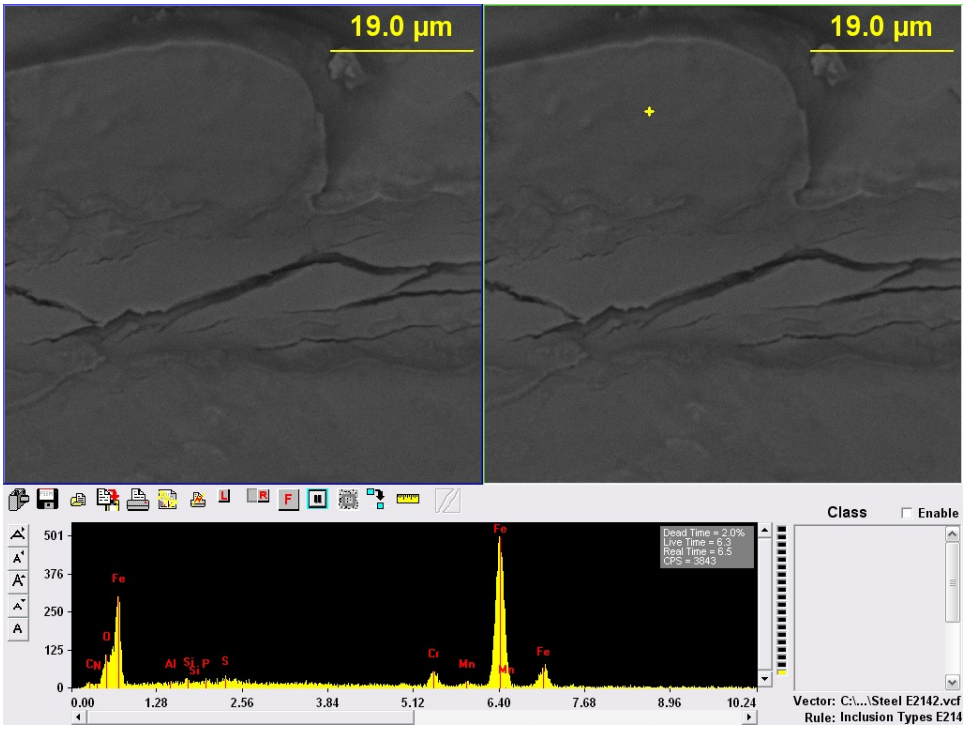

Figure 45: EDS analysis of matrix near segregated film, sample C-10

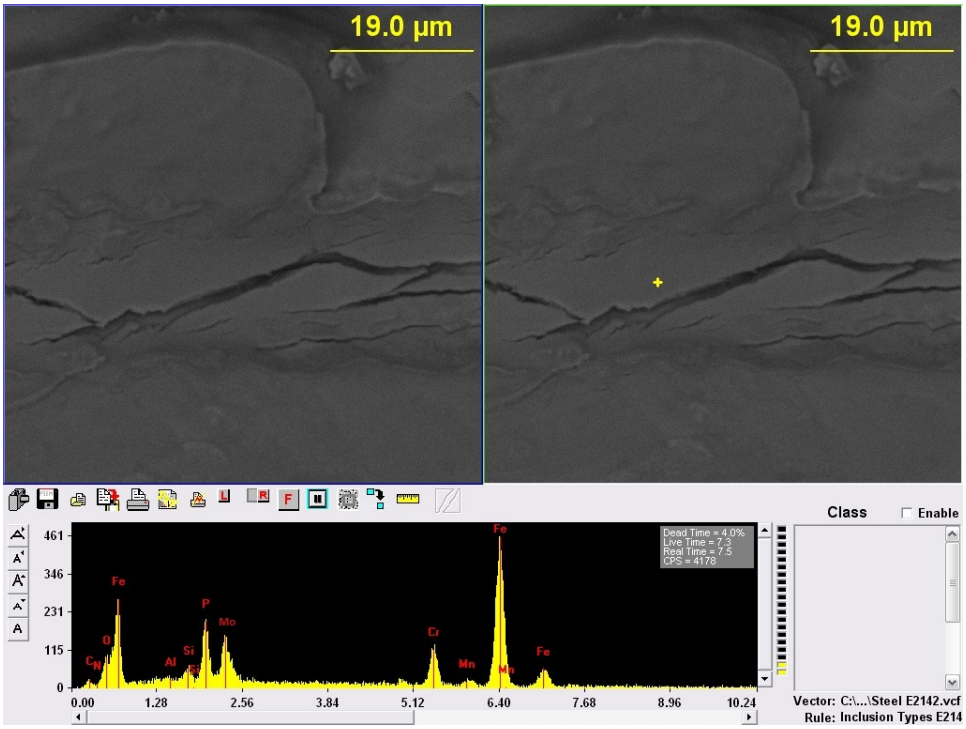

Figure 46: EDS analysis of segregated film showing elevated Cr, Mo and P, sample C-10

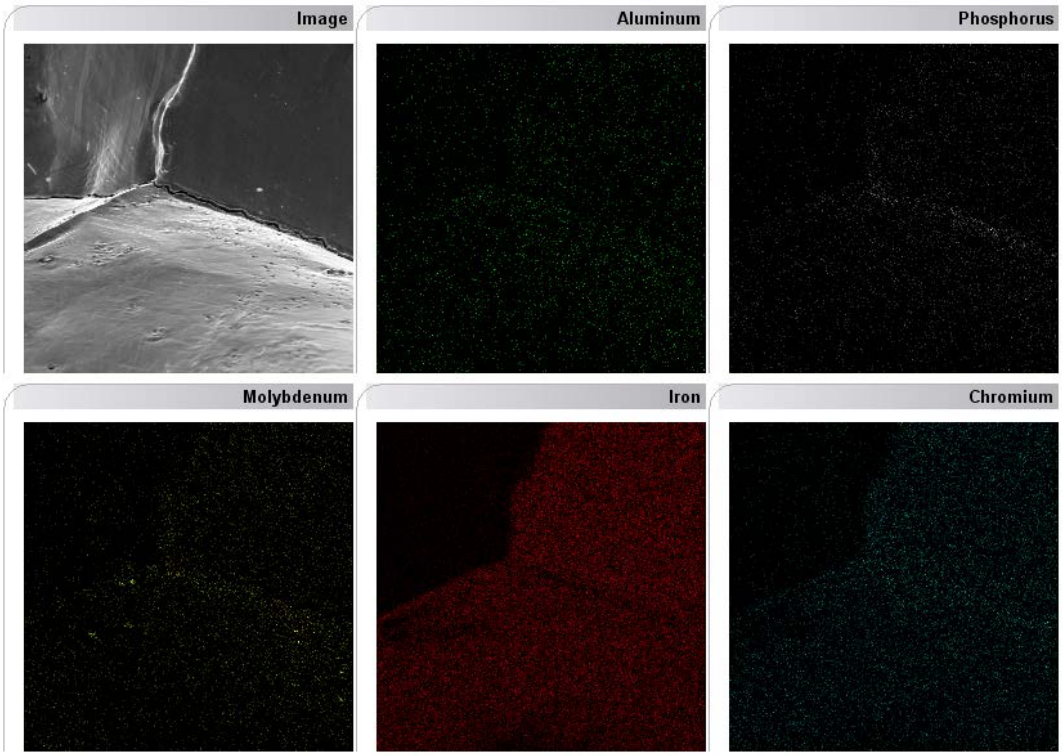

Figure 47: SEM-EDS elemental map from fracture surface of sample A-08

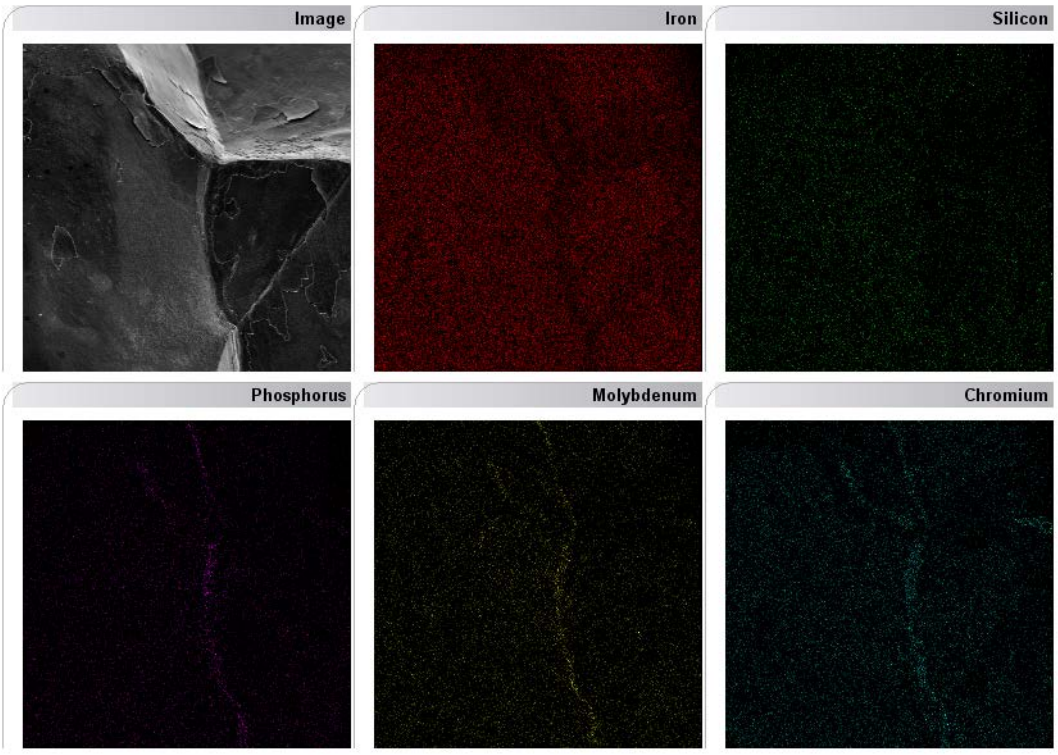

Figure 48: SEM-EDS elemental map from fracture surface of sample B-06

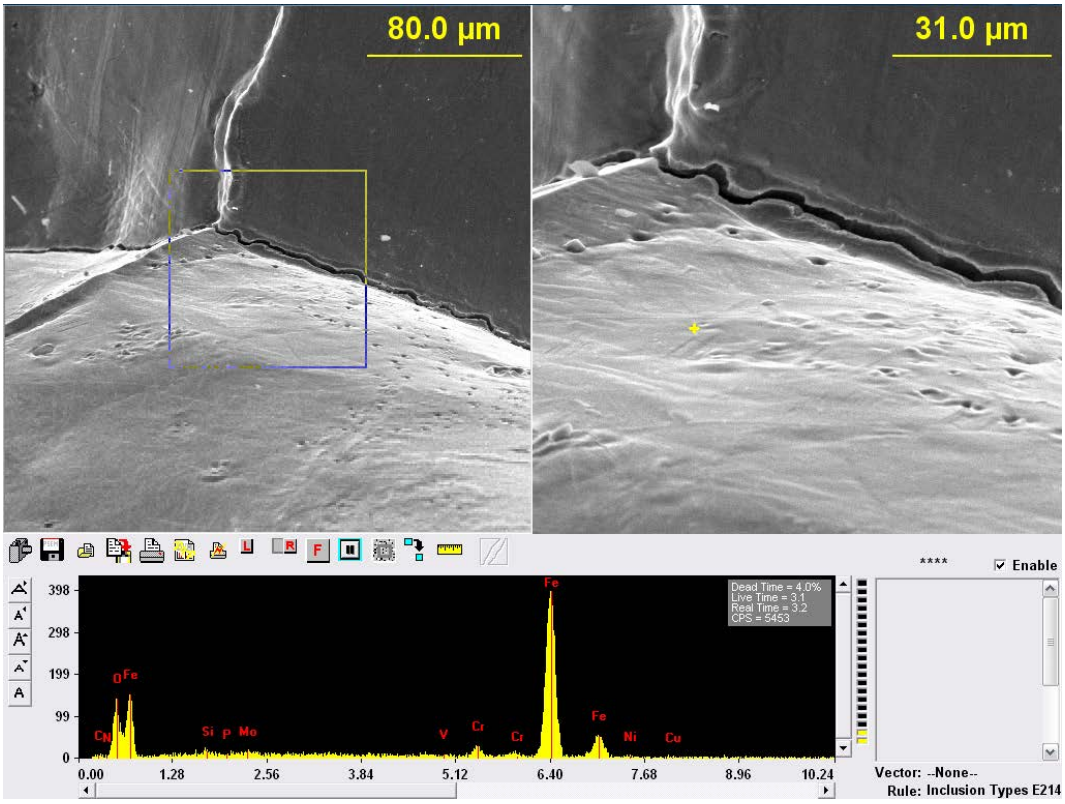

Figure 49: SEM-EDS spot analysis of matrix, sample A-08

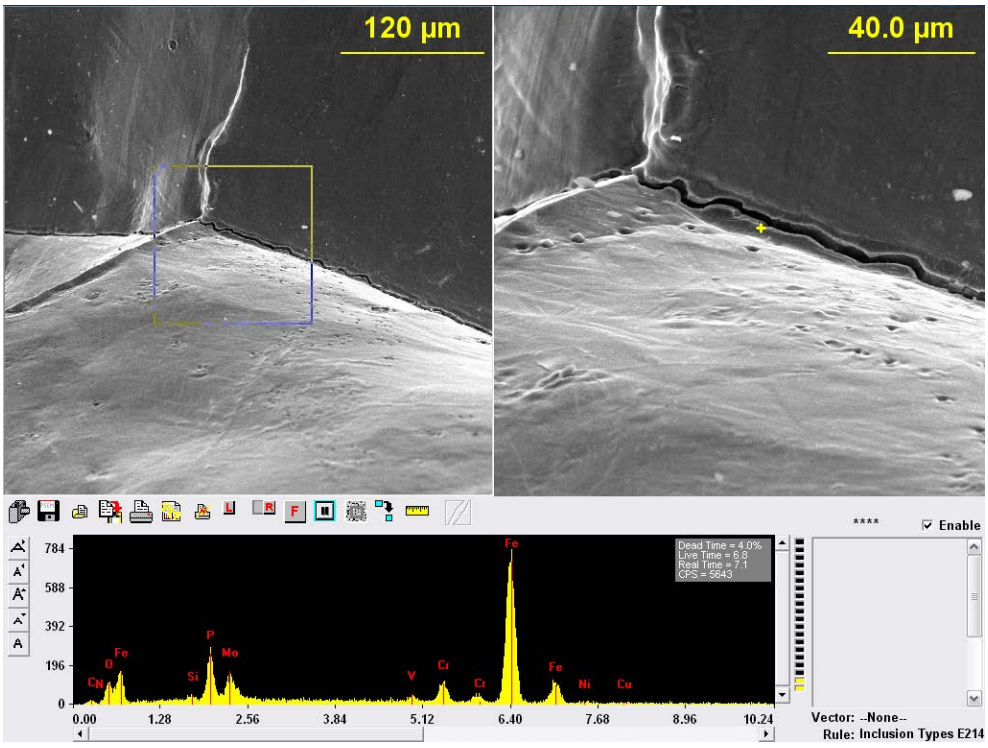

Figure 50: SEM-EDS analysis of segregated film at PAGB, sample A-08

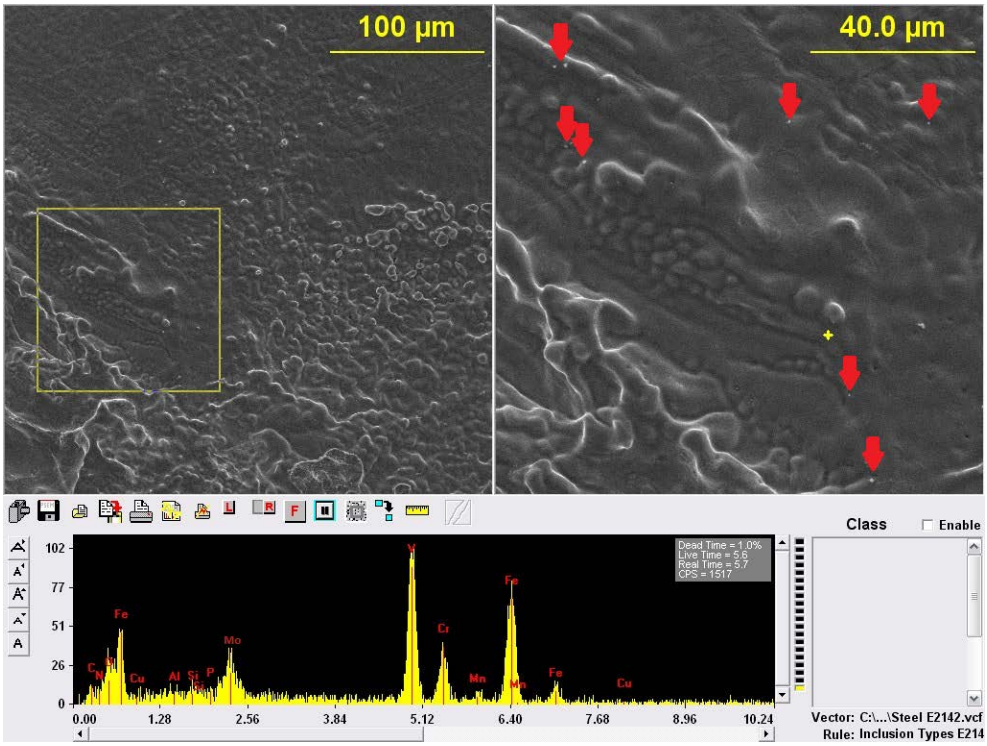

Figure 51: SEM-EDS showing V(C,N) with significant Mo content

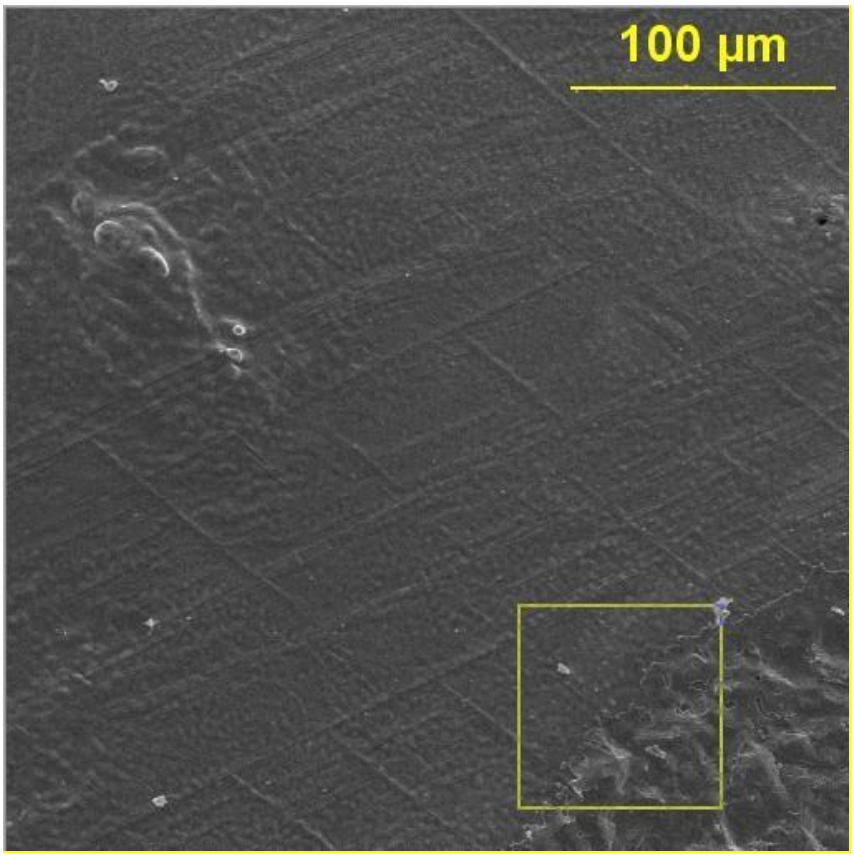

Figure 52: Slip bands due to deformation on removed grain from C-10

6.2 MICROSTRUCTURE AND SEGREGATION

The microstructure in all samples quenched from testing temperatures above the Ar_3 was found to be untempered martensite, as expected. Samples quenched from testing temperatures just below the Ar_3 exhibited a small amount of ferrite formation along prior austenite grain boundaries as shown in Figure 53. Deformation induced ferrite above the Ar_3 temperature was not found in any of the samples.

Deformation had a significant effect on the as-quenched microstructure depending on the temperature at which the samples were deformed. Samples deformed above 900°C that

exhibited ductile failure by microvoid coalescence showed a recrystallized structure in the deformation zone. Deformation below 900° showed no recrystallization, instead the large as-cast grains elongated in the direction of tension. Figure 54 shows the recrystallized grain structure near the fracture surface of the deformed region of sample A-04 (direct cool to 900°C, test) while Figure 55 shows that recrystallization did not occur in the deformed region of sample A-06 (direct cool to 700°C, test).

Electron probe microanalysis (EPMA) was used to examine the level of microsegregation in various samples. The analysis was performed in the interdendritic regions within the grains rather than on the grain boundaries for two reasons:

- The grain boundary thickness is very small compared to the interdendritic segregation bands. The increased thickness of interdendritic segregation bands allow multiple analyses for better accuracy.
- Grain boundaries are more likely to contain precipitates if they are present, which would complicate the interpretation of results.

Three samples were used for comparison of the microsegregation. Samples B-14 and C-21 were undeformed specimens from the intermediate and high [Al][N] compositions. Sample C-03 followed an identical thermal path but was deformed to failure after direct cooling to 1050°C. The segregation is clearly visible when using an etchant for revealing the dendritic structure as shown in Figure 56.

Although a certified reference standard (NIST 1763a) was used for EPMA analysis there remained discrepancies in the EPMA results and the analysis of the bulk material by optical emission spectroscopy (OES). These discrepancies are likely due to surface contamination, inhomogeneous microstructural features within the reference standard and differences between the composition of the reference standard and the experimental material. The OES method is

well known to provide accurate and certifiable bulk chemical analysis of low alloy steels. The EPMA matrix composition results were therefore normalized to the OES bulk analysis that was provided in Table 5. An example of the normalization calculation for sample C-03 is given in Table 12, showing the average raw atomic percent from the EPMA matrix spots, the EPMA atomic percent converted to wt%, the OES bulk analysis, the multiplication factor used for each element and the corrected EPMA wt% value after normalization. Note that aluminum and sulfur did not show reasonable values in the EPMA analysis and are not included. This may be due to the low aluminum and sulfur content of the reference standard. The final corrected EPMA wt% values must be regarded as semi-quantitative due to the normalization described above. Relative precision of EPMA analyses using the JOEL JXA-8530F is approximately 1-2%. Based on the variation of results from point to point it is clear that the material has inhomogeneity at a scale much smaller than that of the segregation banding.

Table 12: EPMA results of Sample C-03 matrix and corrected wt%

	EPMA raw at%	EPMA wt%	OES wt%	at% multiplier	Corrected EPMA wt%
C%	0.85	0.18	0.34	1.86	0.34
Si%	1.03	0.53	0.34	0.65	0.34
Cr%	1.43	1.35	2.03	1.52	2.03
Fe%	95.68	96.82	94.61	1.00	94.61
Mo%	0.09	0.15	0.22	1.44	0.22
P%	0.020	0.011	0.011	1.01	0.011
V%	0.049	0.045	0.059	1.23	0.059
Ni%	0.85	0.91	0.78	0.87	0.78

Figure 57 shows the segregation band of sample B-14 along with the EPMA analysis locations (in red). The yellow lines indicate the approximate edges of the segregated region

which is difficult to see even with back-scattered electron imaging mode. Figure 58 shows the EPMA results graphically. The vertical red lines indicate the approximate bounds of the segregated region. The 95% confidence interval around the mean of the segregated and non-segregated areas is noted. Similarly the images and results for samples C-21 and C-03 are given in Figures 59 – 62. A summary of the results for all three samples are presented in Table 13. There is segregation of Si, Cr, Mo and V in the undeformed sample B-14. Undeformed sample C-21 shows increased segregation of Cr, Mo and V compared to sample B-14, in addition to a small amount of phosphorus segregation. The deformed sample C-03 exhibits a much higher level of segregation for all elements listed with the exception of nickel which showed only a slight increase from matrix to segregation band.

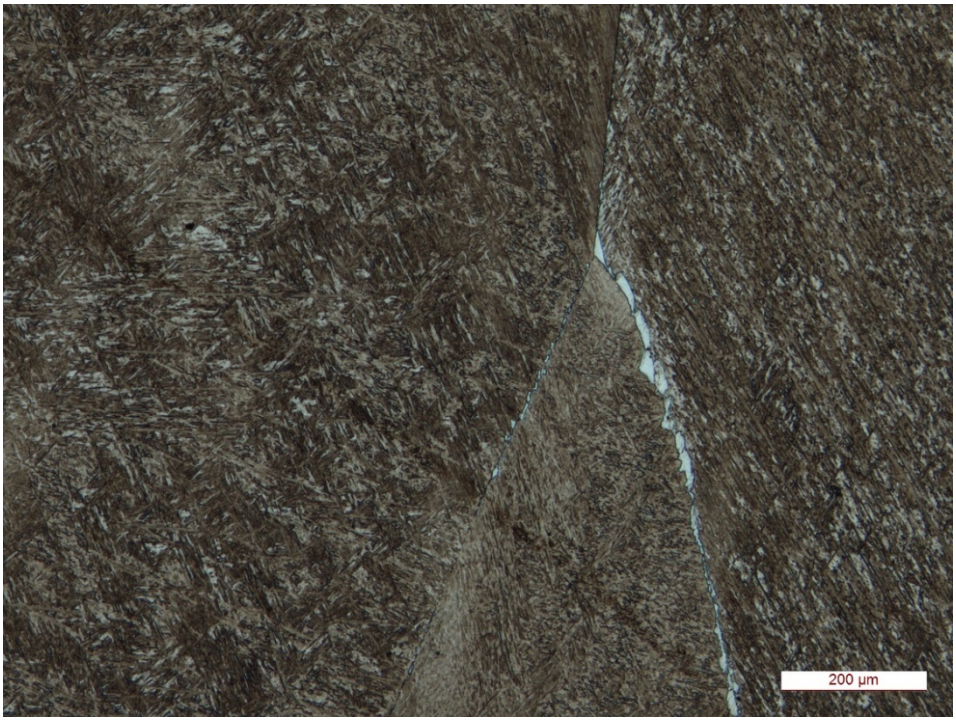

Figure 53: Ferrite formation on PAGB, sample A-07, RA = 76.6%

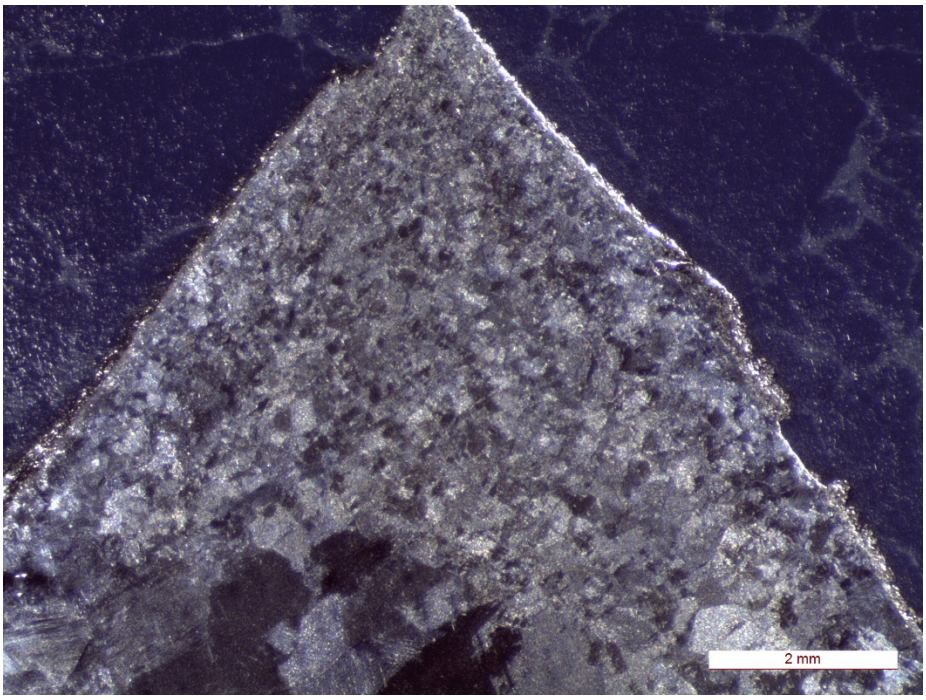

Figure 54: Evidence of dynamic recrystallization in sample A-04

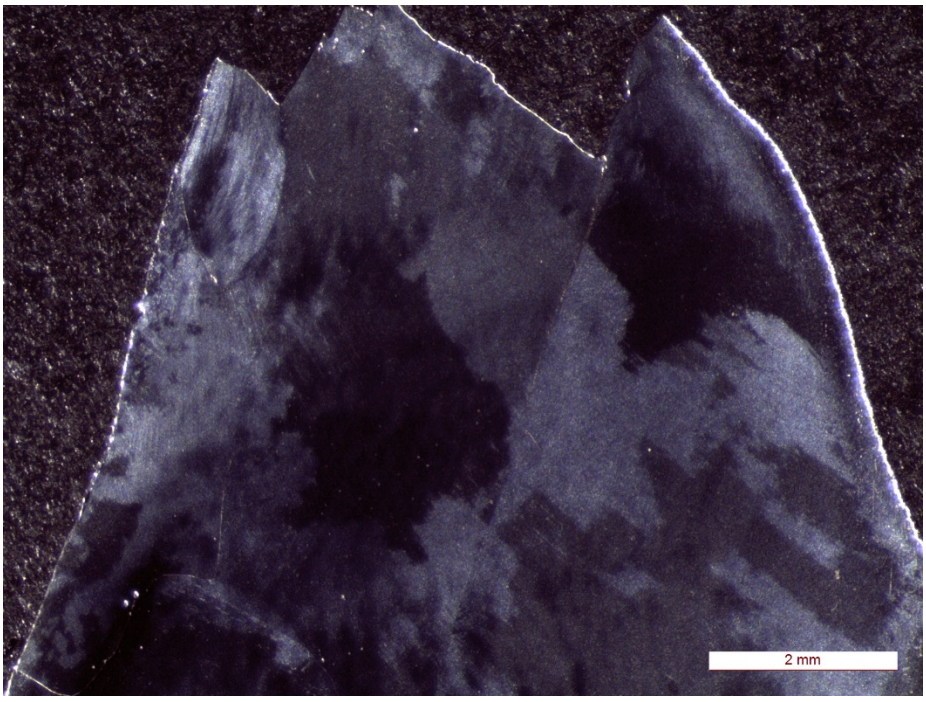

Figure 55: Lack of dynamic recrystallization in sample A-06

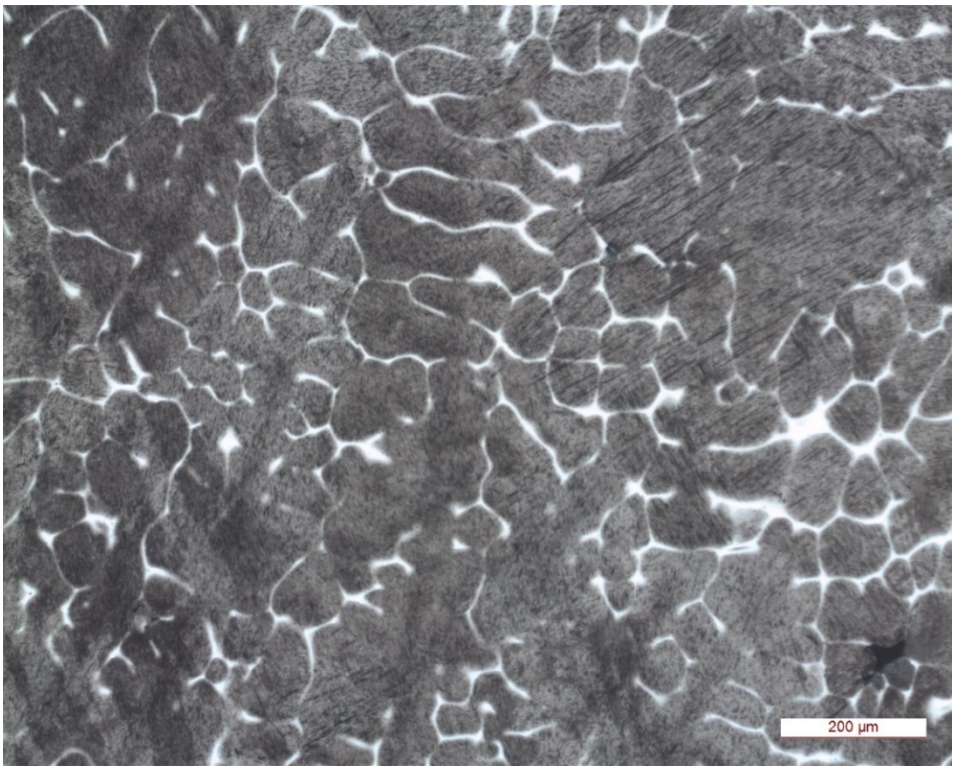

Figure 56: Segregation, dendritic etchant from [106] then 5% nital, steel C

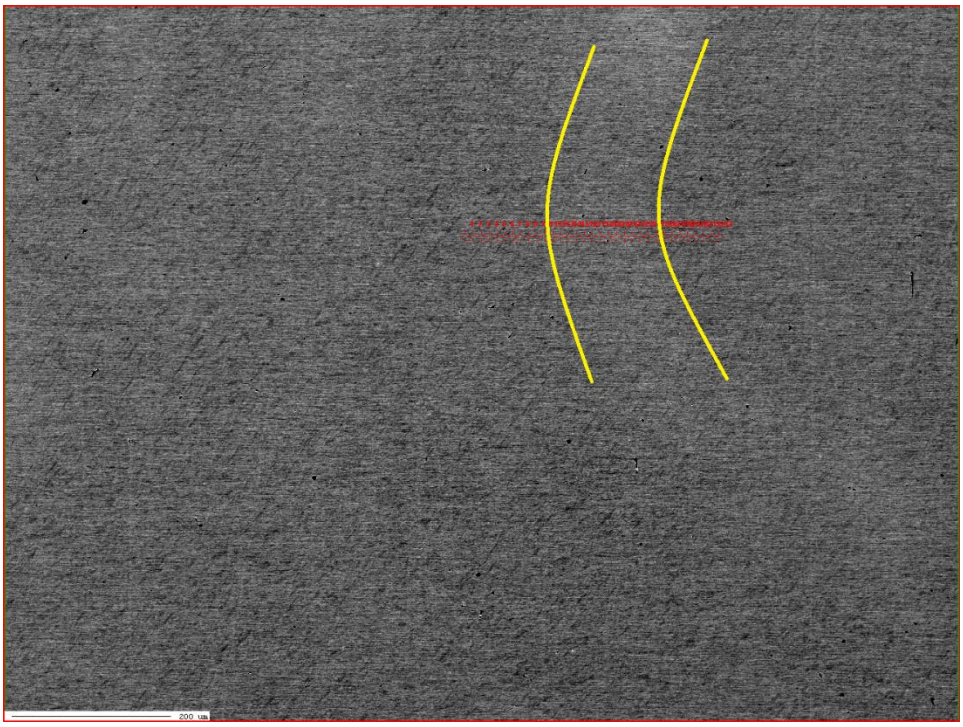

Figure 57: EPMA line scan points of sample B-14, yellow lines indicate segregated area

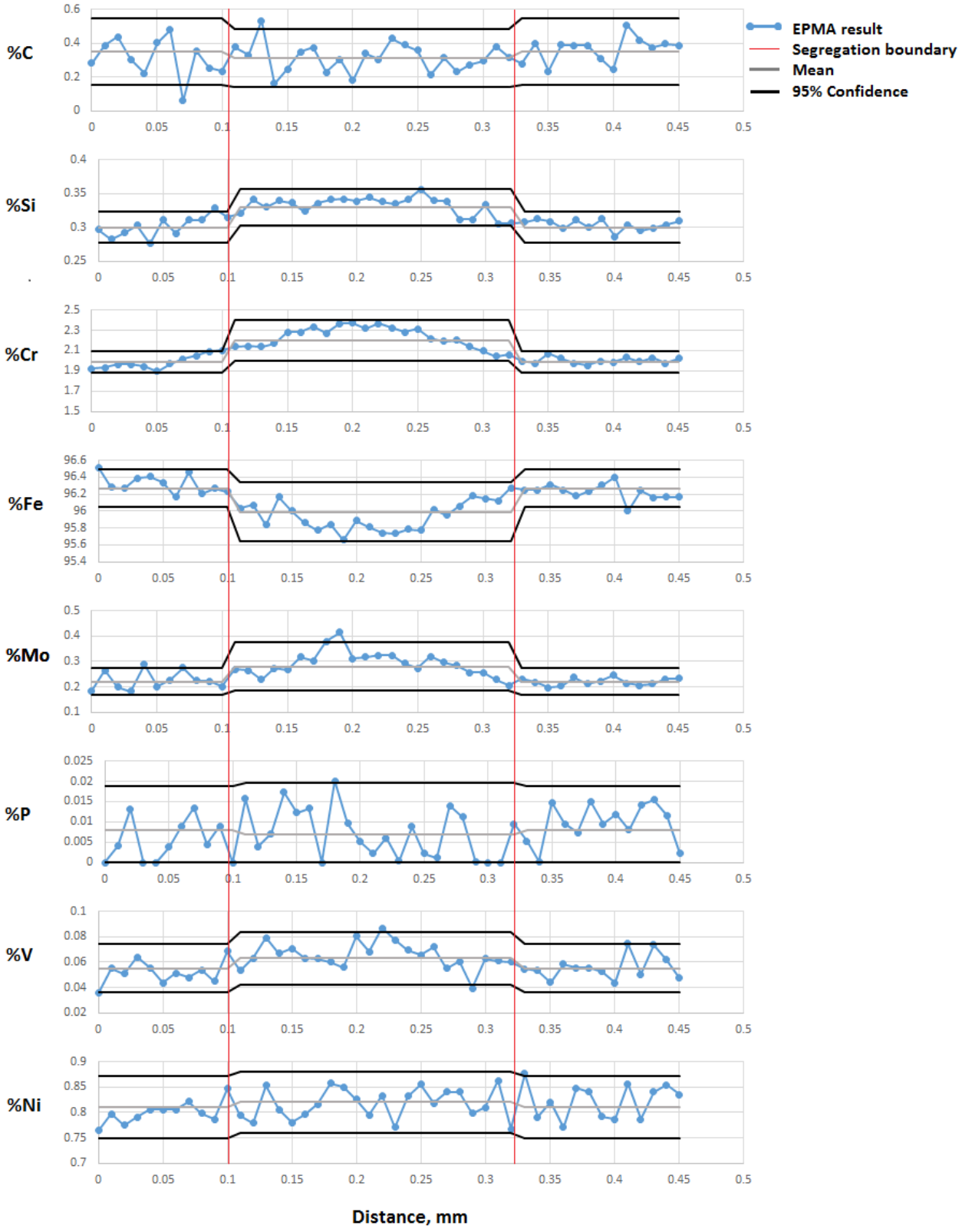

Figure 58: EPMA results of sample B-14, y-axis values in wt%

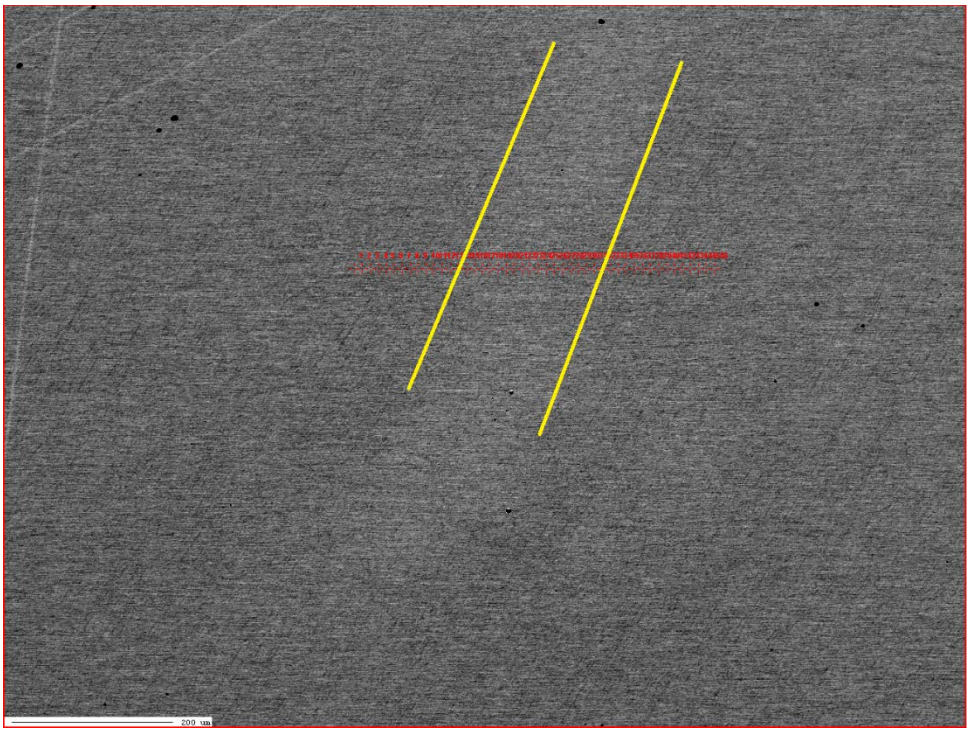

Figure 59: EPMA line scan points of sample C-21, yellow lines indicate segregated area

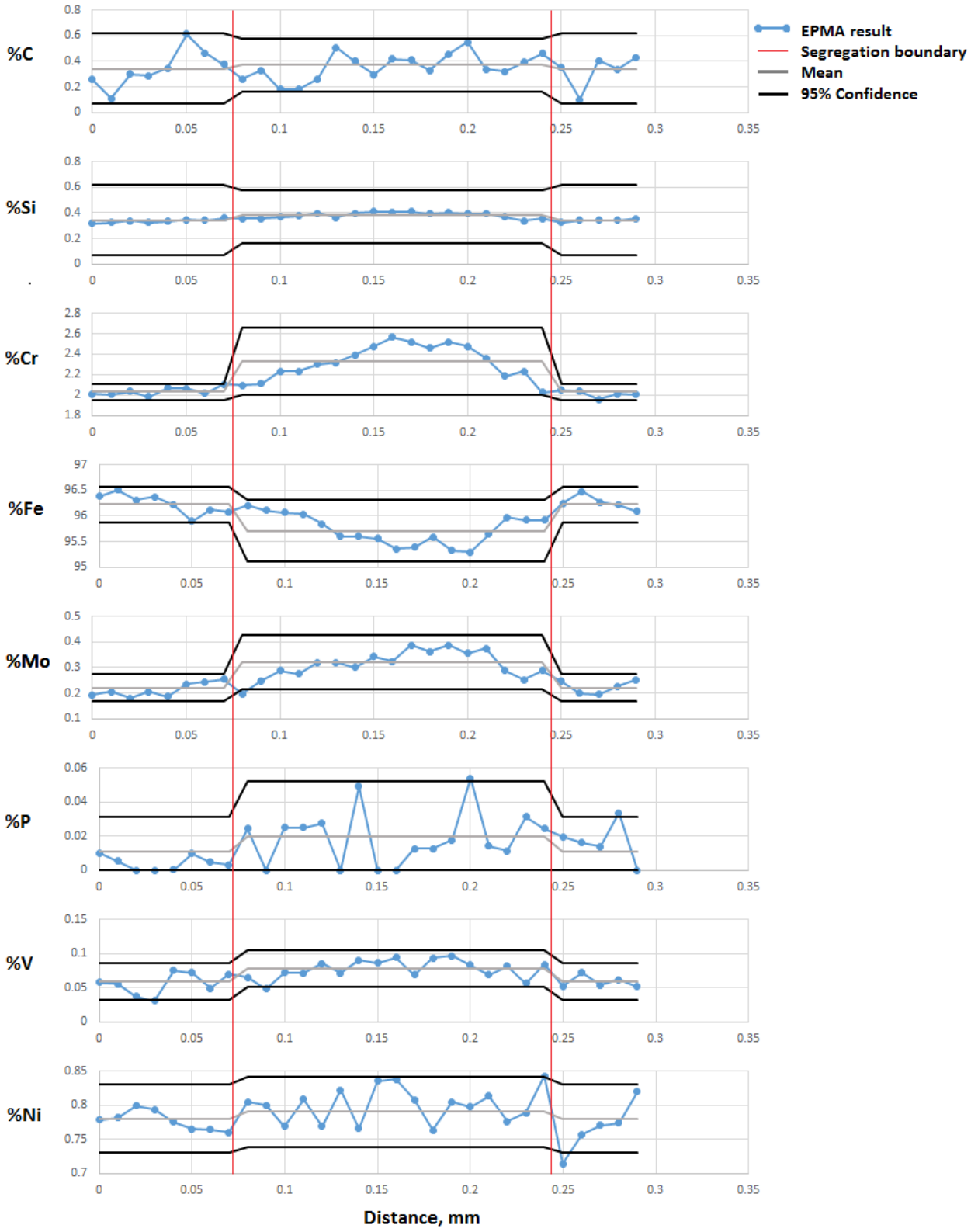

Figure 60: EPMA results of sample C-21, y-axis values in wt%

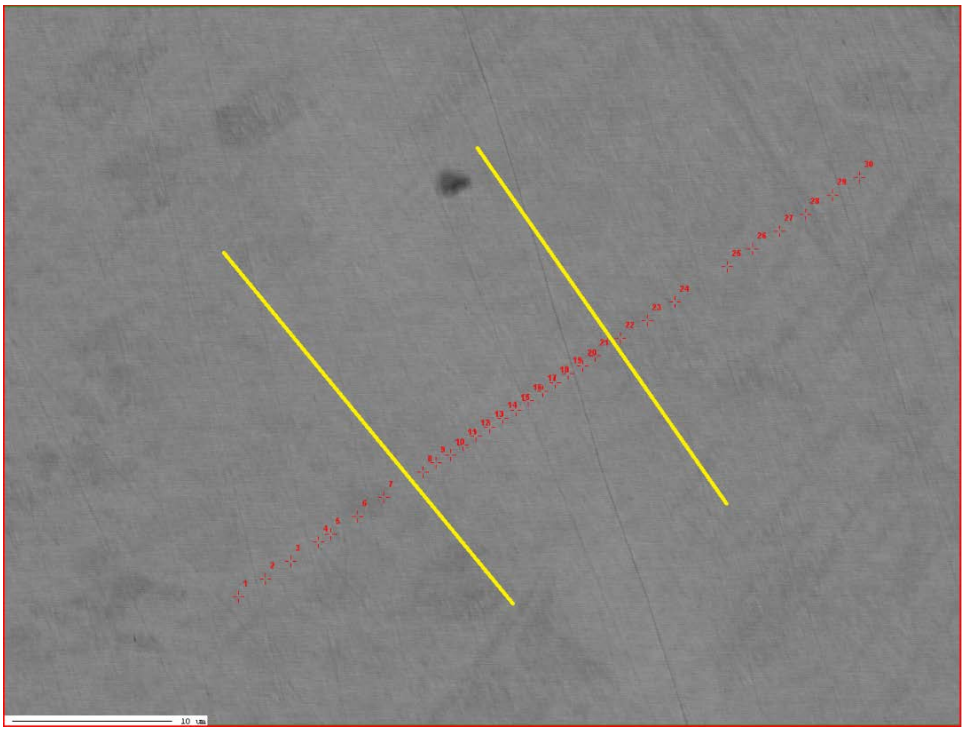

Figure 61: EPMA line scan points of sample C-03, yellow lines indicate segregated area

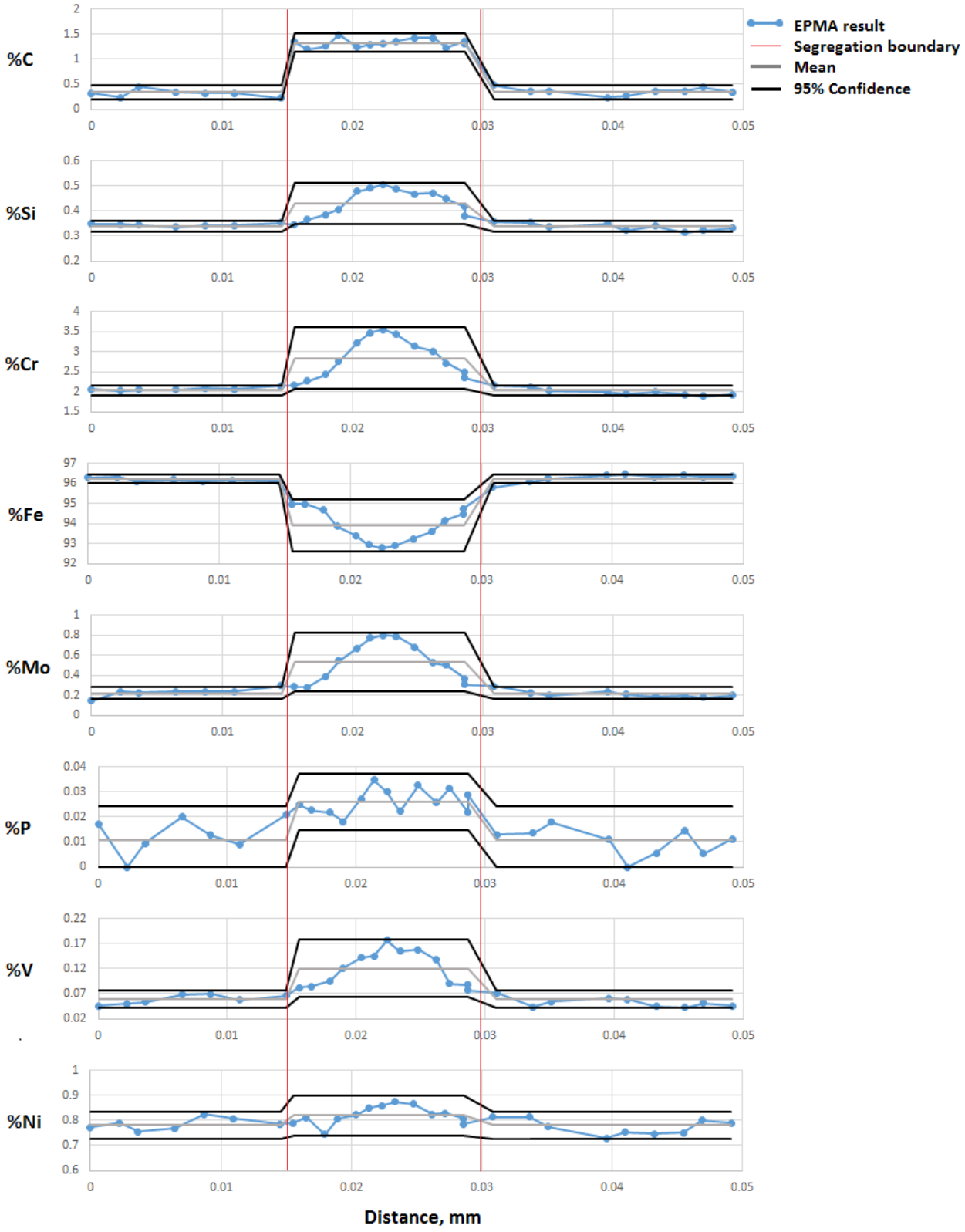

Figure 62: EPMA results of sample C-03, y-axis values in wt%

Table 13: Summary of results from EPMA analyses

Sample	Area	C%	Si%	Cr%	Fe%	Mo%	P%	V%	Ni%
Steel B-14 undeformed	Matrix avg.	0.35	0.30	1.99	96.27	0.22	0.008	0.055	0.81
	Band avg.	0.31	0.33	2.20	95.99	0.28	0.007	0.063	0.82
	Band max.	0.31	0.34	2.37	95.66	0.41	0.010	0.056	0.85
Steel C-21 undeformed	Matrix avg.	0.34	0.34	2.03	96.22	0.22	0.011	0.059	0.78
	Band avg.	0.37	0.38	2.33	95.71	0.32	0.020	0.078	0.79
	Band max.	0.55	0.39	2.48	95.28	0.36	0.054	0.083	0.80
Steel C-03 deformed	Matrix avg.	0.34	0.34	2.03	96.22	0.22	0.011	0.059	0.78
	Band avg.	1.33	0.43	2.84	93.90	0.53	0.026	0.120	0.82
	Band max.	1.30	0.51	3.55	92.78	0.80	0.030	0.177	0.86

6.3 DILATOMETRY

The results of the dilatometry work showed that the formation of ferrite and pearlite was accelerated in steel C as compared to steel A. Proeutectoid ferrite formed in both steels at cooling rates of up to 1.0C/min. As the cooling rate was increased beyond this point the high-temperature transformation was to primarily pearlite. At a cooling rate of 1.8°C/min the pearlite island precipitation in steel A was finer and more uniform than that of steel C. The ductility trough found during the direct cooling to test temperature experiments occurred at temperatures well above the Ar_3, in the fully austenitic temperature range and the pearlite formation from dilatometry experiments is occurring at lower temperatures.

In the in-situ cast material it was found that the formation of proeutectoid ferrite was suppressed significantly (very low volume fraction in the samples direct cooled and tested at 700°C). Sample C-18 followed the direct cooling thermal path to 650°C and was then held isothermally for six hours in order to examine the transformation that occurred. The sample was quenched without deformation at the end of the six hour hold at temperature. Figure 63 shows

an optical micrograph of this sample where pearlite formation is clearly visible on the prior austenite grain boundaries. No ferrite was present in the sample. This phenomena can be explained by carbon and alloying element segregation at the prior austenite grain boundary during the solidification giving a composition that further suppresses proeutectoid ferrite.

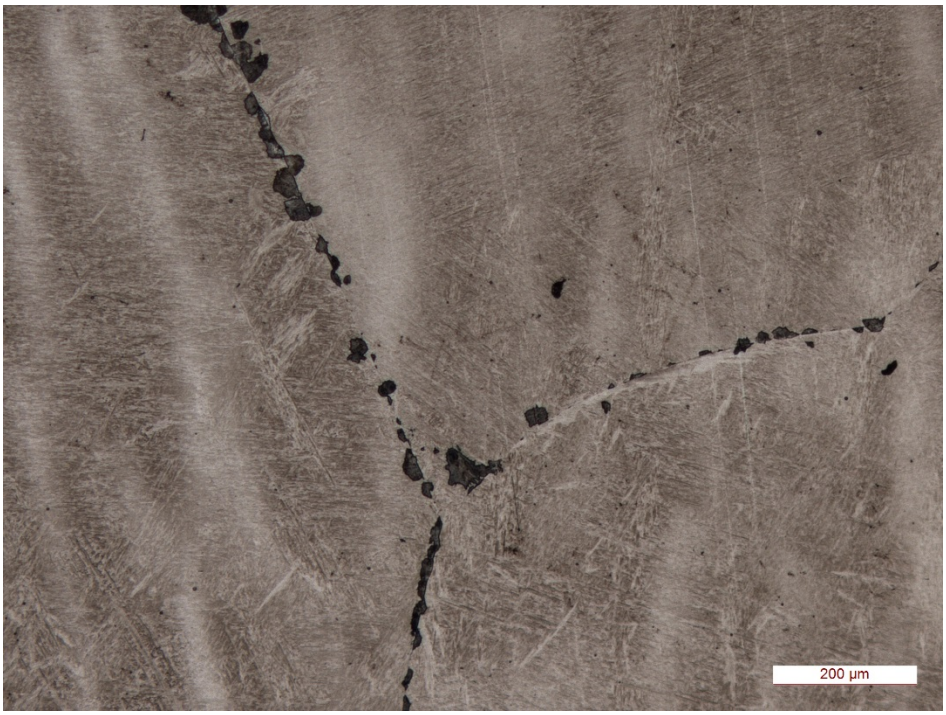

Figure 63: OM image of pearlite on prior austenite grain boundaries, sample C-18

6.4 ALUMINUM NITRIDE

Many of the metallurgical analysis methods employed were done so in order to classify the size and morphology of the anticipated AlN precipitates. However, no distinct AlN precipitates were able to be directly identified in these studies. It may be possible that the AlN precipitate size was smaller than could be detected using the techniques employed in this work.

The electrolytic dissolution work showed evidence of aluminum-based precipitates via ICP analysis of the extracted particles and comparison to the remaining electrolyte, however upon examining the extracted particles via TEM it was very clear that the process had been contaminated by using silicone stoppers during dissolution. The silicone integrity was compromised by the acids used for dissolution and digestion and the data were thereby invalid.

The TEM specimen preparation techniques discussed in section 4.2.6 were validated using a sample of C-Mn material that exhibited sub-surface cracking and had elevated aluminum and nitrogen contents. AlN precipitates were identified in this material following the same sample preparation techniques used for the experimental samples of this work. Figures 64 and 65 show an AlN precipitate of approximately 50 nm length and 5 nm width, along with the associated EDS analysis. Figure 64 includes the matrix and particle FFT images. The precipitate FFT spots match well with AlN cubic B1 structure (002) planes. The matrix FFT shows spots for martensite (001) and austenite (110) planes at a measured angle of 21°, which matches with the expected angle based on the Kurdjumov Sachs relationship where $(111)_{\gamma} \parallel (011)_{\alpha'}$. Note the significant Cr and V content of this precipitate which was found in a plain carbon steel.

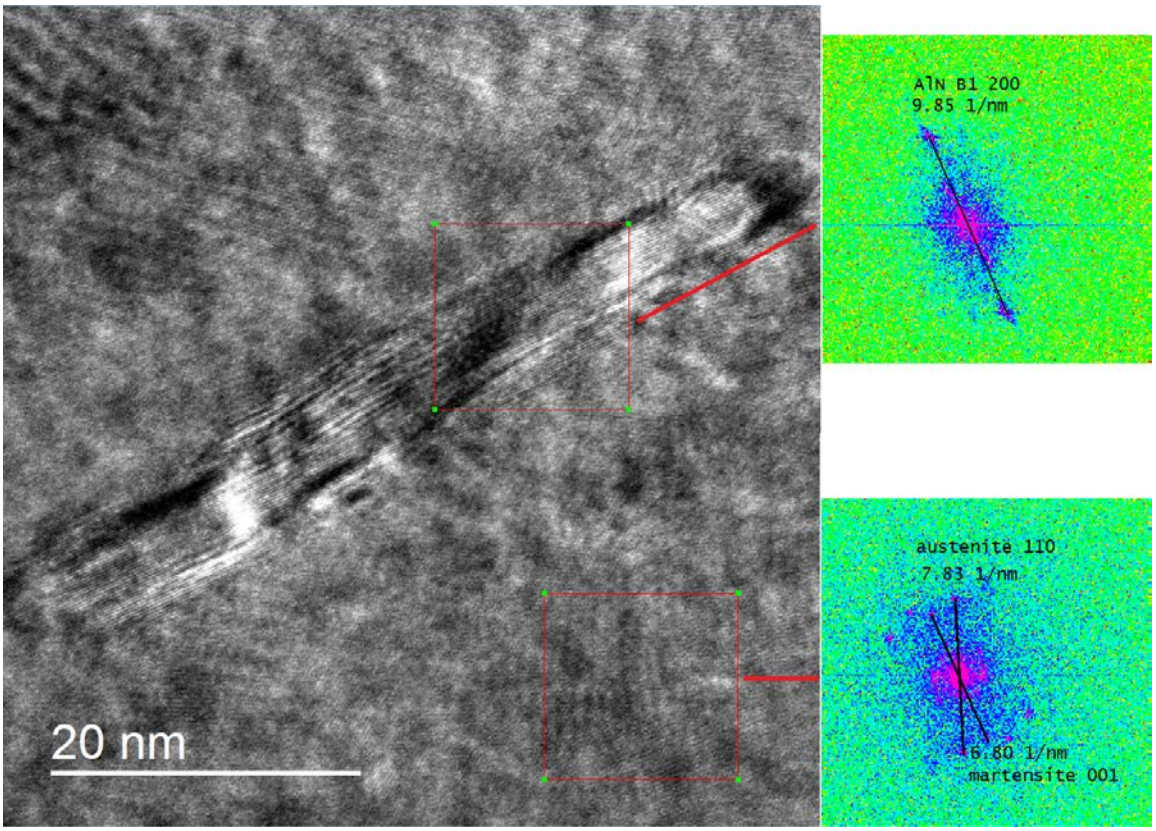

Figure 64: AlN precipitate in commercial C-Mn steel

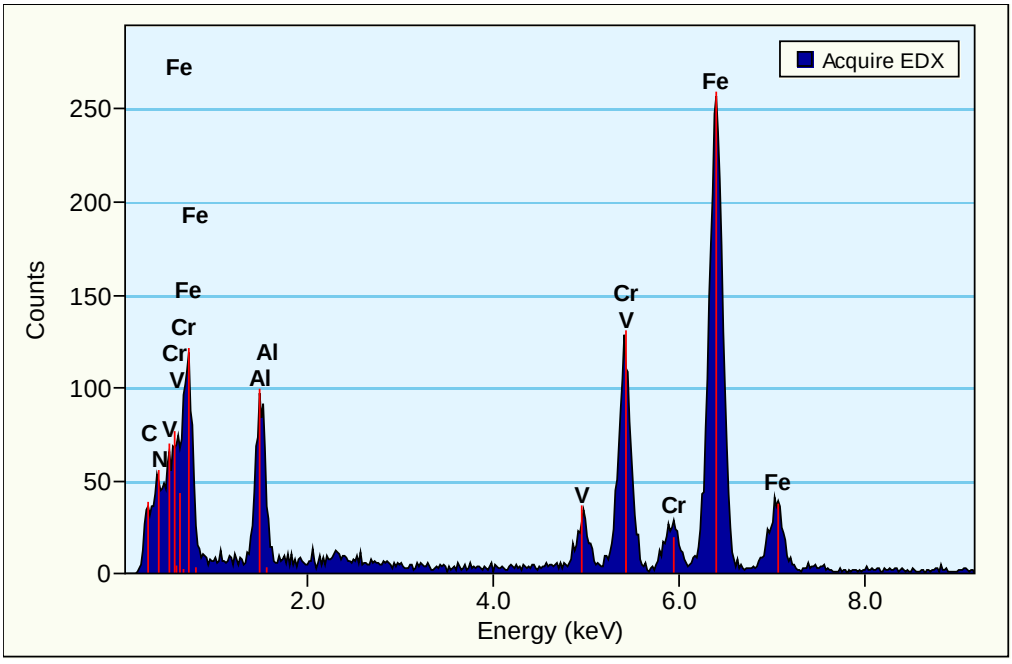

Figure 65: EDS analysis of AlN precipitate in C-Mn steel

6.5 FRACTURE SURFACE FILM

The thin film containing elevated levels of alloying elements discussed in section 6.1 was able to be extracted from the fracture surface of sample C-19 and fished onto a 300-mesh nickel grid for TEM analysis. Sample C-19 was the test performed with extremely high argon flow in order to preserve the fracture surface. A low magnification TEM bright field image of the extracted film is shown in Figure 66. EDS analysis showed various compositions within the film as shown in Figure 67.

Selected area electron diffraction combined with EDS analysis confirmed the presence of two distinct phases in the film:

- MX-type carbonitride
- M_7C_3 carbide

The MX carbonitride was present in much smaller amounts than the M_7C_3 carbide. The MX carbonitride was contained V, Mo, C and N as shown by the EDS analysis in Figure 67 (upper right). The Ni from this analysis is due to the Ni mesh used to hold the extracted sample. This was confirmed by performing EDS analysis on an empty area of the carbon film and the Ni peaks were still present as shown in Figure 68. Selected area electron diffraction showed an FCC crystal structure with lattice parameter 0.416 nm which agrees well with published[107,108] data for V(C,N), see Figure 69. The atomic radii of vanadium and molybdenum are similar so it is reasonable that the lattice parameter of the carbide matches that of V(C,N) even with a significant amount of molybdenum substituted into the MX carbide.

The M_7C_3 carbide contained primarily iron, chromium, molybdenum and carbon. In certain areas there were also various levels of phosphorus, vanadium, silicon and aluminum present in the EDS analysis. This matches well with the PAGB film identified by SEM-EDS on

the fracture surfaces. Several EDS analyses of the M_7C_3 are shown in Figures 70 and 71. Figure 70 shows the bulk carbide analysis containing primarily Fe, Cr, Mo and C with a small amount of vanadium. When phosphorus was present in the EDS analysis it was generally a significant portion of the composition as shown in Figure 71. The elevated aluminum is also visible in this EDS analysis.

The precise crystal structure of M_7C_3 is not generally agreed upon in the literature. Table 14 shows various stated structures and lattice parameters given in previous works. Morniroli et al.[109] show that "an orthorhombic superstructure occurs in three orientation variants referred to an underlying hexagonal lattice" in the M_7C_3 carbides. The complex crystal structure makes full interpretation of electron diffraction patterns difficult, and in this work the issue is exacerbated by the thickness of this film potentially leading to double diffraction.

Selected area electron diffraction patterns of the thin film confirm that M_7C_3 carbide accounts for the majority of the thin film. Figures 72 and 73 show the apparent six-fold axis indexed as M_7C_3 with the hexagonal and orthorhombic structures using the lattice parameters listed in Table 14.

Table 14: M_7C_3 structures presented in literature

Structure	Lattice Parameter(s), nm	Reference
Hexagonal	$a_0 = 0.6969$, $c_0 = 0.4463$	110
Pseudo-hexagonal	$a_0 = 1.3982$, $c_0 = 0.4506$	111
Orthorhombic	$a_0 = 0.4512$, $b_0 = 0.6891$, $c_0 = 1.2119$	110

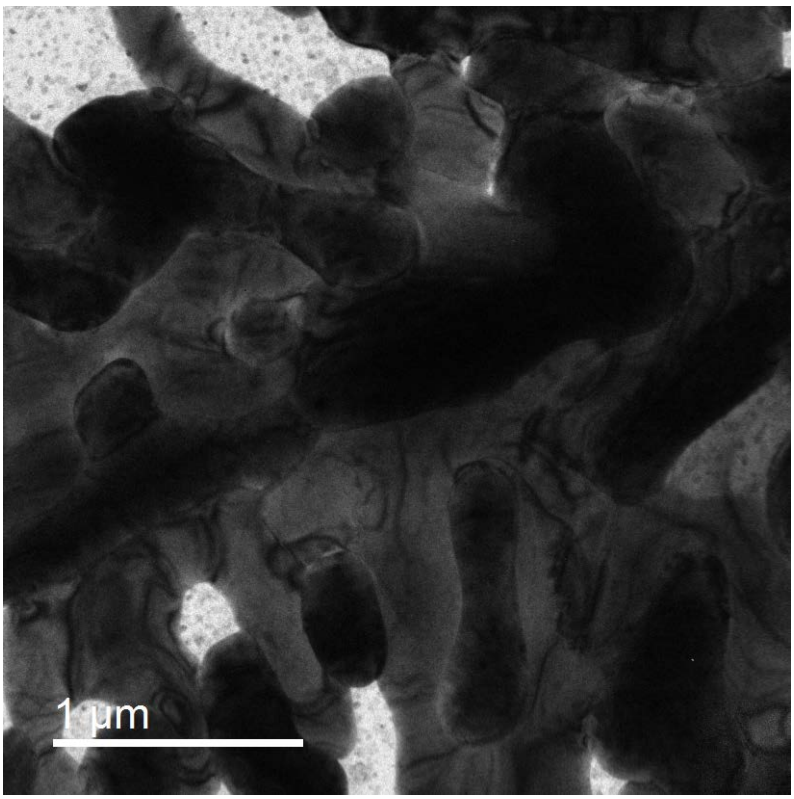

Figure 66: TEM low magnification image of carbide film

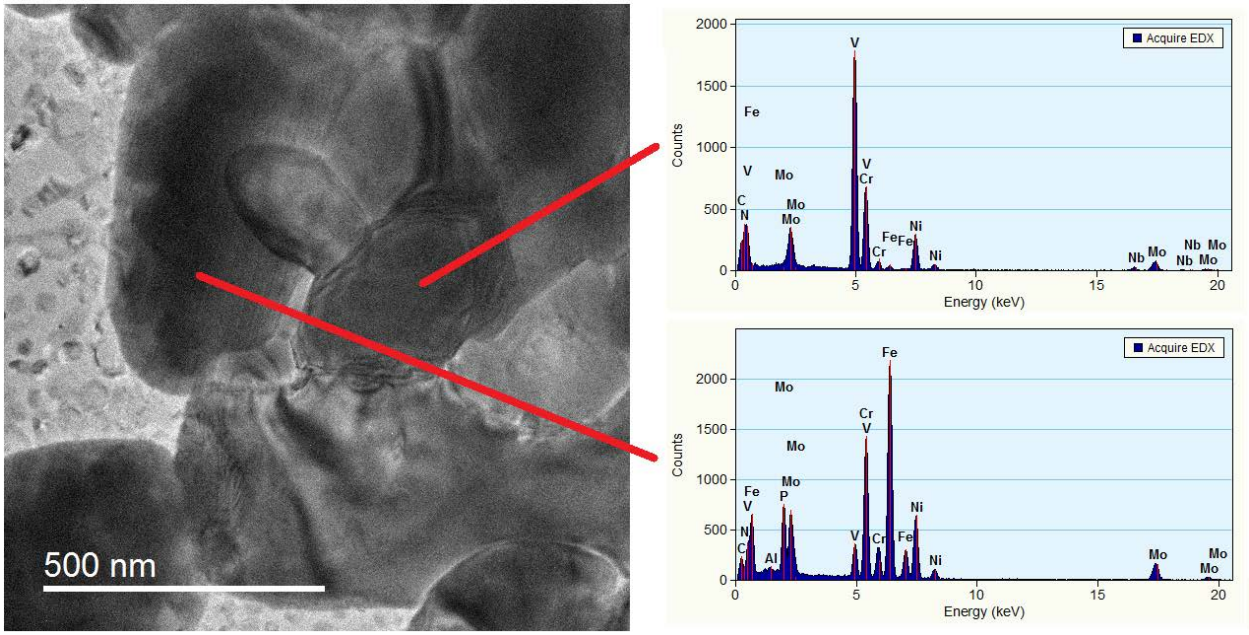

Figure 67: TEM image with EDS analyses showing intermixed MX and M_7C_3

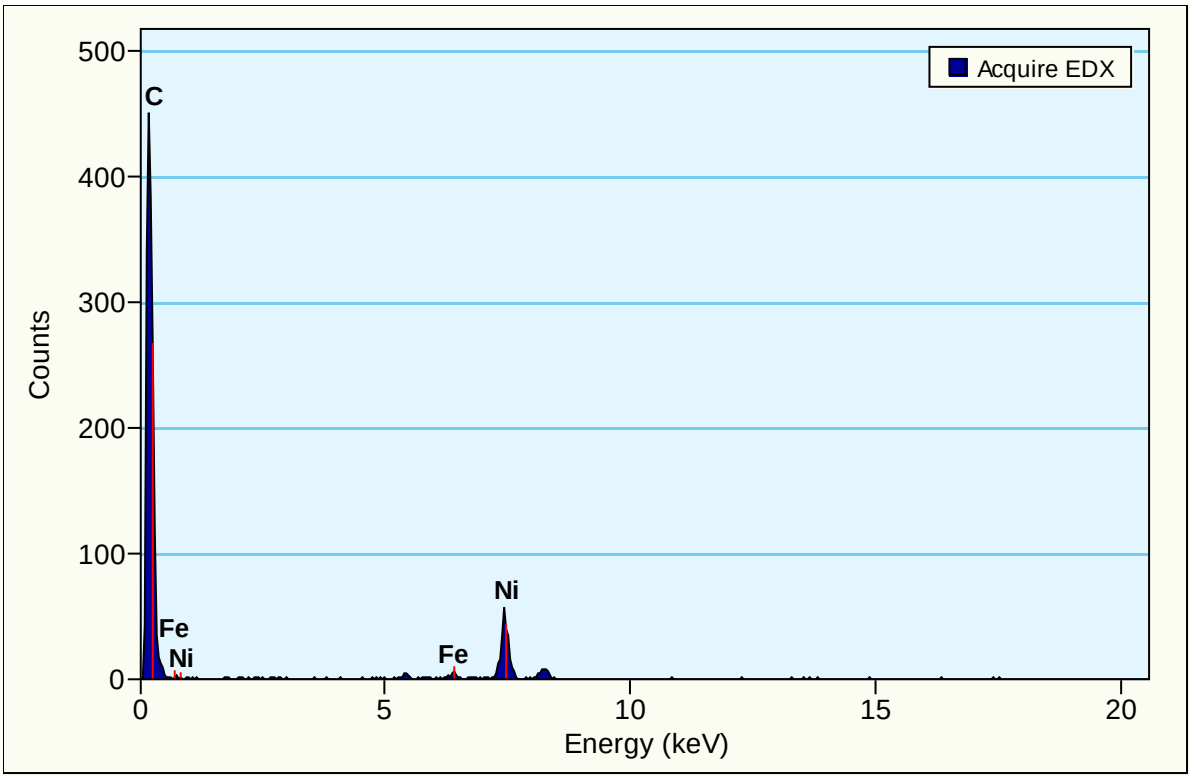

Figure 68: EDS analysis of carbon film on 300 mesh Ni grid

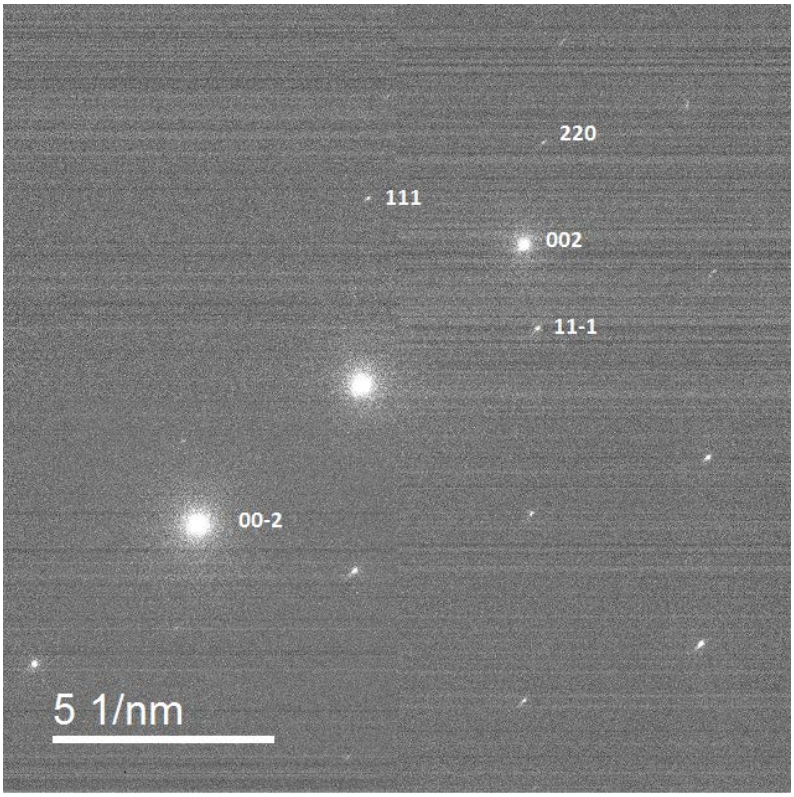

Figure 69: SAED of MX carbonitride, V(C,N), near [-110] zone axis

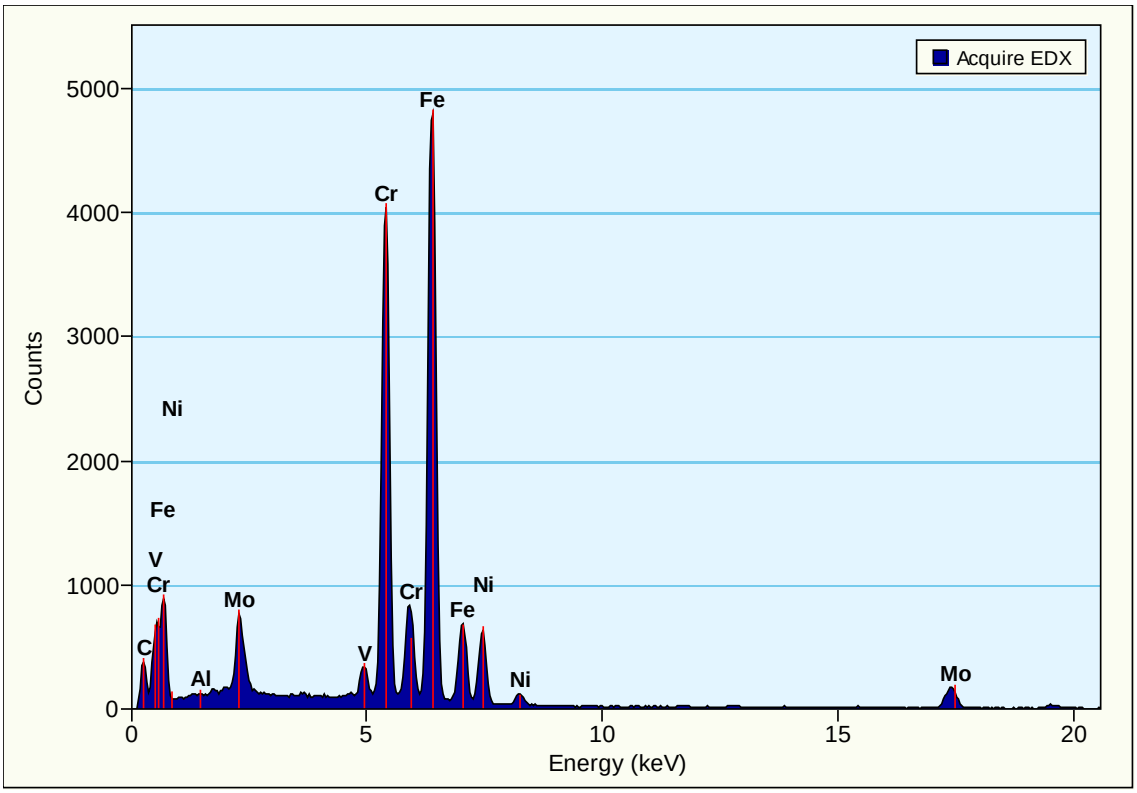

Figure 70: TEM-EDS analysis of bulk M_7C_3 carbide

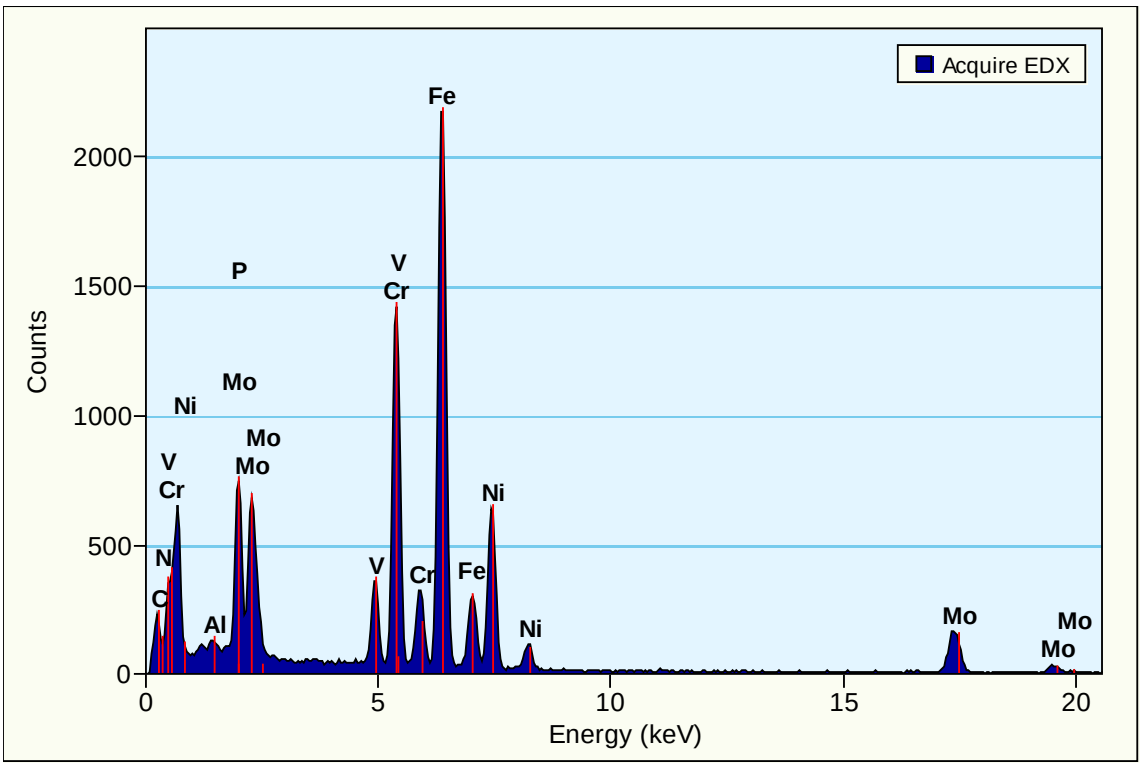

Figure 71: TEM-EDS analysis with significant phosphorus content

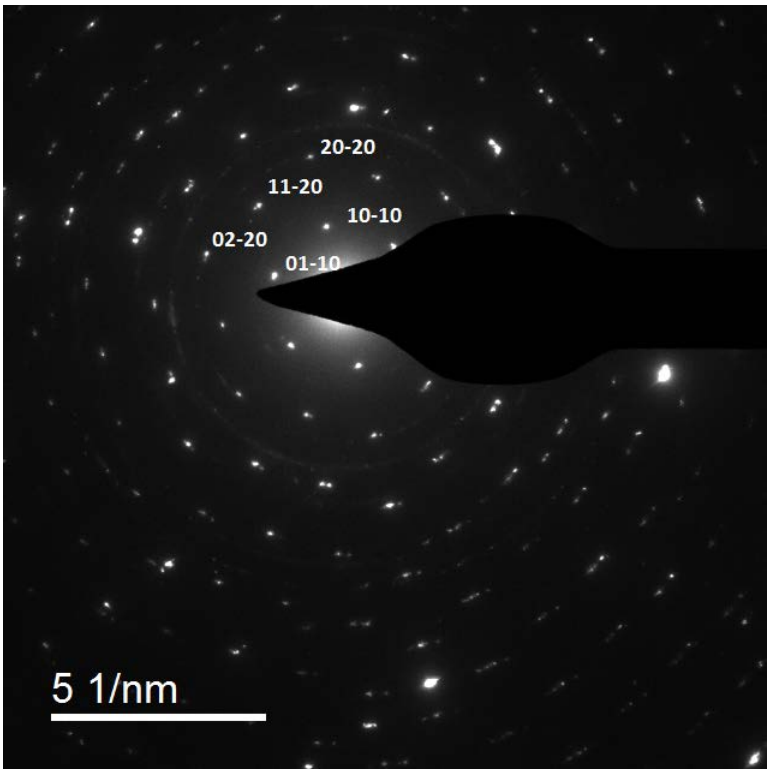

Figure 72: TEM diffraction pattern of M_7C_3 indexed as HCP, [0001] zone axis

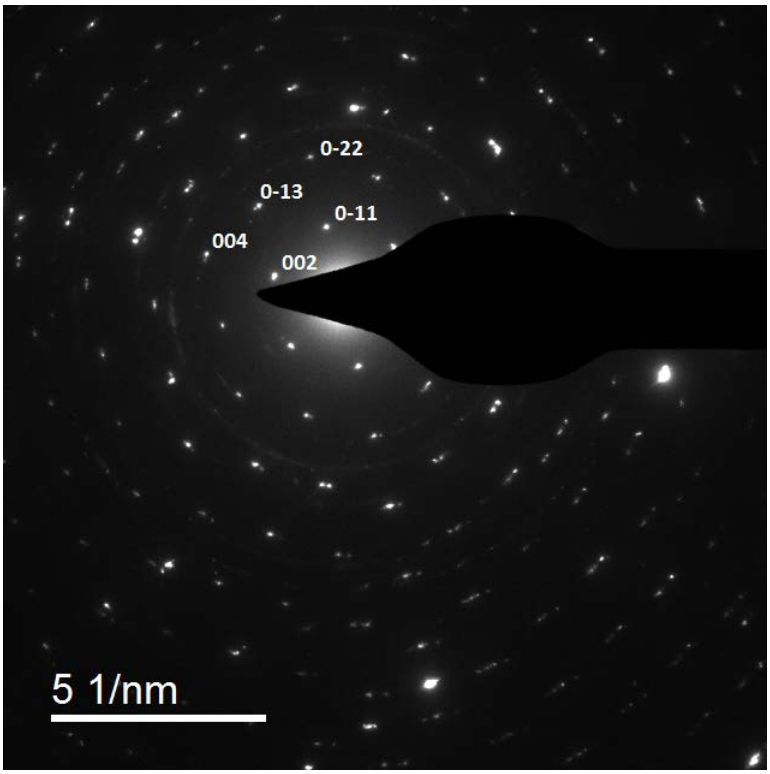

Figure 73: TEM diffraction pattern of M_7C_3 indexed as orthorhombic, [100] zone axis

7.0 NUMERICAL PRECIPITATION MODEL

A numerical precipitation model was developed using MATLAB in an attempt to better understand the parameters which might affect nucleation and growth of precipitates in austenite. The model follows classical nucleation theory and allows simultaneous nucleation, and growth of precipitates. This section will describe the theoretical background and implementation of the precipitation model.

7.1 NUCLEATION

Classical nucleation theory gives the transient nucleation rate, *J*, as

$$J = N\beta^* Z e^{\left(\frac{-\Delta G^*}{k_b T}\right)} e^{\left(\frac{-\tau}{t}\right)}$$

where

N = number of potential nucleation sites

β^* = atomic attachment frequency

Z = Zeldovich non-equilibrium factor

ΔG^* = Gibb's free energy of forming a nucleus of critical size, r^*

k_b = Boltzmann's constant

T = temperature (K)

τ = incubation time

The value of *J* is in units of nuclei per second per unit volume. In the present work, the values for N, β^*, Z and ΔG^* are re-calculated at each time interval according to the current thermodynamic and physical state. The temperature is pre-determined as a function of time as an input to the model. The transient term, $e^{\left(\frac{-\tau}{t}\right)}$, is handled in a separate way which will be described later. The terms required to calculate the nucleation rate are described in detail below.

ΔG^*- Gibb's free energy of forming a nucleus of critical size

The Gibb's free energy of forming a precipitate nuclei is written as

$$\Delta G = V(\Delta G_v + \Delta G_s) + A\sigma - A'\gamma_{gb}$$

where

V = precipitate volume

ΔG_v = chemical free energy of formation per unit volume

ΔG_s= volume strain energy of forming a precipitate within the matrix

A = precipitate surface area

σ = precipitate/matrix interfacial energy

A' = grain boundary area removed by precipitate (for heterogeneous precipitation)

γ_{gb} = grain boundary energy

The free energy equation can be re-written in terms of the spherical precipitate radius, *r*, as

$$\Delta G(r) = \frac{4}{3}\pi r^3(\Delta G_v + \Delta G_s) + 4\pi r^2\sigma - \pi r^2\gamma_{gb}$$

with the assumption that the precipitates nucleate in a manner so that their cross section is maximum along the grain boundary and the grain boundary curvature is approximately planar in

comparison to the precipitate. This assumption is reasonable as it will maximize the negative free energy contribution due to removal of grain boundary area. A plot of the free energy versus radius shows a critical point (r^*) where the total free energy is at a maximum with respect to changes in precipitate size, see Figure 74. The free energy at this point is denoted ΔG^* and is the critical free energy of formation of a stable nucleus.

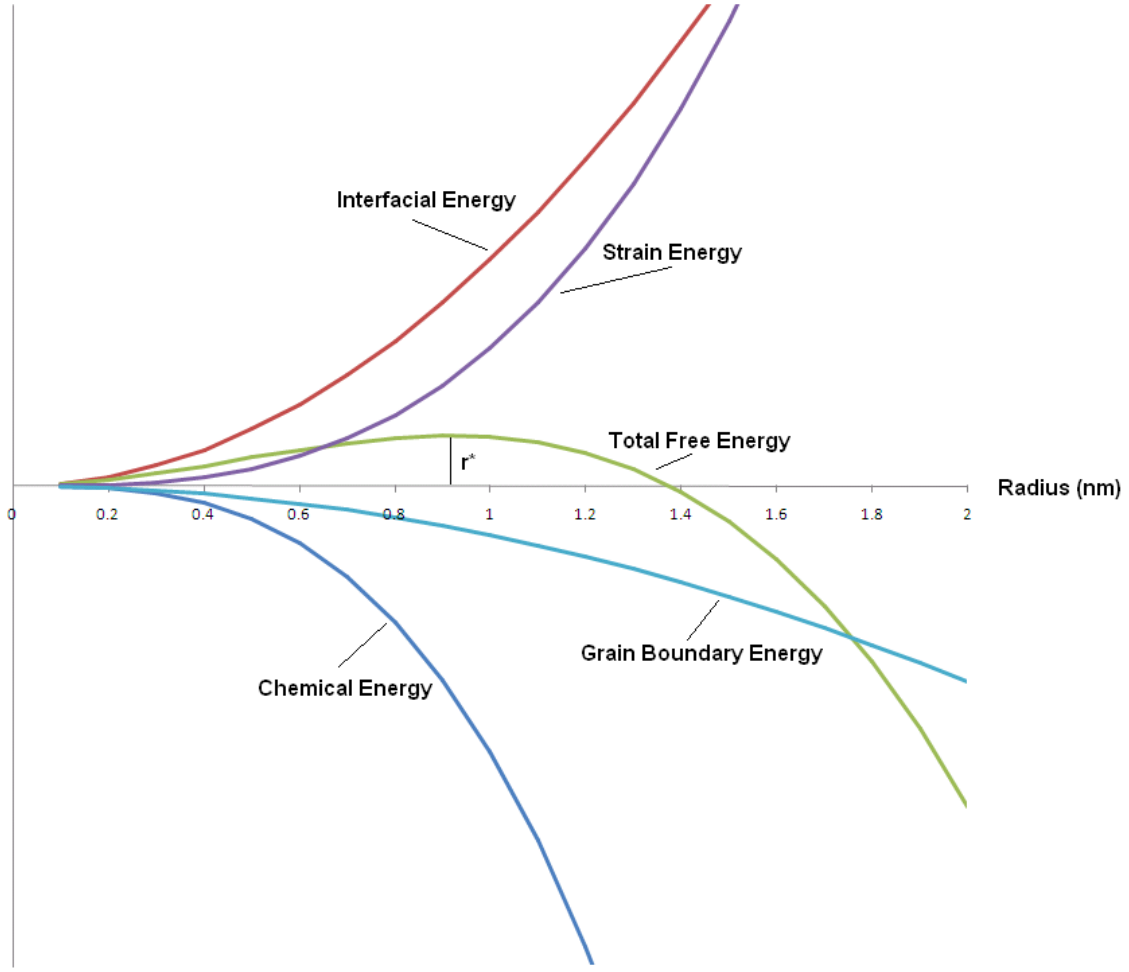

Figure 74: Energy balance for formation of a critical nucleus, r*

The chemical free energy term for AlN formation, ΔG_v, can be calculated thermodynamically from the reaction of aluminum and nitrogen,

$$Al + N \rightarrow AlN$$

for which the Gibbs free energy change is

$$\Delta G_v = \mu_{AlN}^{\gamma} - \mu_{Al}^{\gamma} - \mu_{N}^{\gamma}$$

where μ_i^{ϕ} is the chemical potential of component *i* in phase φ. The chemical potential of AlN is calculated as a function of temperature as[112]

$$\mu_{AlN}^{\gamma} = -345837 + 359.862T - 54.3087TlnT + 8.56x10^{4}T^{2} + \frac{2.326x10^{6}}{T} - \frac{1.26x10^{8}}{T^{2}} + H_{Al}^{0} + \frac{1}{2}H_{N_2}^{0}$$

where H_i^0 is the standard state enthalpy of component *i*. The values for μ_N^{γ} and μ_{Al}^{γ} were approximated by Cheng[112] through binary Fe-N and Fe-Al systems as

$$\mu_N^{\gamma} = \mu_N^{0,\gamma} + RTln\left[\frac{y_N^{\gamma}}{1 - y_N^{\gamma}}\right] - \frac{2}{s_i} y_N^{\gamma} L_N^{\gamma,Fe}$$

$$\mu_{Al}^{\gamma} = \mu_{Al}^{0,\gamma} + RTlny_{Al}^{\gamma} + \left(y_{Fe}^{\gamma}\right)^2 L_{Fe,Al}^{\gamma}$$

where the values of *L* are regular solution binary interaction parameters. The term y_i^{γ} is the sublattice fraction of component *i* and is determined through the relationships

$$y_N^{\gamma} = \frac{S_s}{S_i}\frac{X_N^{\gamma}}{\left(X_{Al}^{\gamma} + X_{Fe}^{\gamma}\right)}$$

$$y_{Al}^{\gamma} = \frac{X_{Al}^{\gamma}}{\left(X_{Al}^{\gamma} + X_{Fe}^{\gamma}\right)}$$

$$y_{Al}^{\gamma} + y_{Fe}^{\gamma} = 1$$

Cheng[112] compiled the necessary thermodynamic parameters for completing these calculations for the Fe-Al-N system from various other works as (in J/mol):

$$\mu_N^{0,\gamma} = -7358.85 + 17.2T - 16.4TlnT - 6.5x10^{-4}T^2 + 3.01x10^{-8}T^3 + 563070T^{-1} + \frac{1}{2}H_{N_2}^0$$

$$\mu_{Al}^{0,\gamma} = -2132.5 - 14.767T - 0.0247T^2 + H_{Al}^0$$

$$S_0 = S_1 = 1 \; for \; FCC \; iron$$

$$L_N^{\gamma,Fe} = \text{-}26150$$

$$L_{Fe,Al}^{\gamma} = L_{(Fe,Al)_0}^{\gamma} + L_{(Fe,Al)_1}^{\gamma}(y_{Fe}^{\gamma} - y_{Al}^{\gamma})$$

$$L_{(Fe,Al)_0}^{\gamma} = -96053 + 18.408T$$

$$L_{(Fe,Al)_1}^{\gamma} = 31654 - 19.474T$$

The final results allow calculation of the chemical free energy as a function of aluminum content, nitrogen content and temperature. It is then possible to determine the zero free energy composition for a given temperature, i.e. the solubility, which can be approximated by the familiar form of the solubility product

$$\log([Al][N]) = \frac{A}{T} + B$$

Using the thermodynamic values from Cheng as listed in the Appendix, chemical free energy values were tabulated and the values for A and B were approximated as -12596 and 5.213, respectively. Figure 75 shows the comparison of the fitted solubility product curve and the tabulated values calculated from the thermodynamic method.

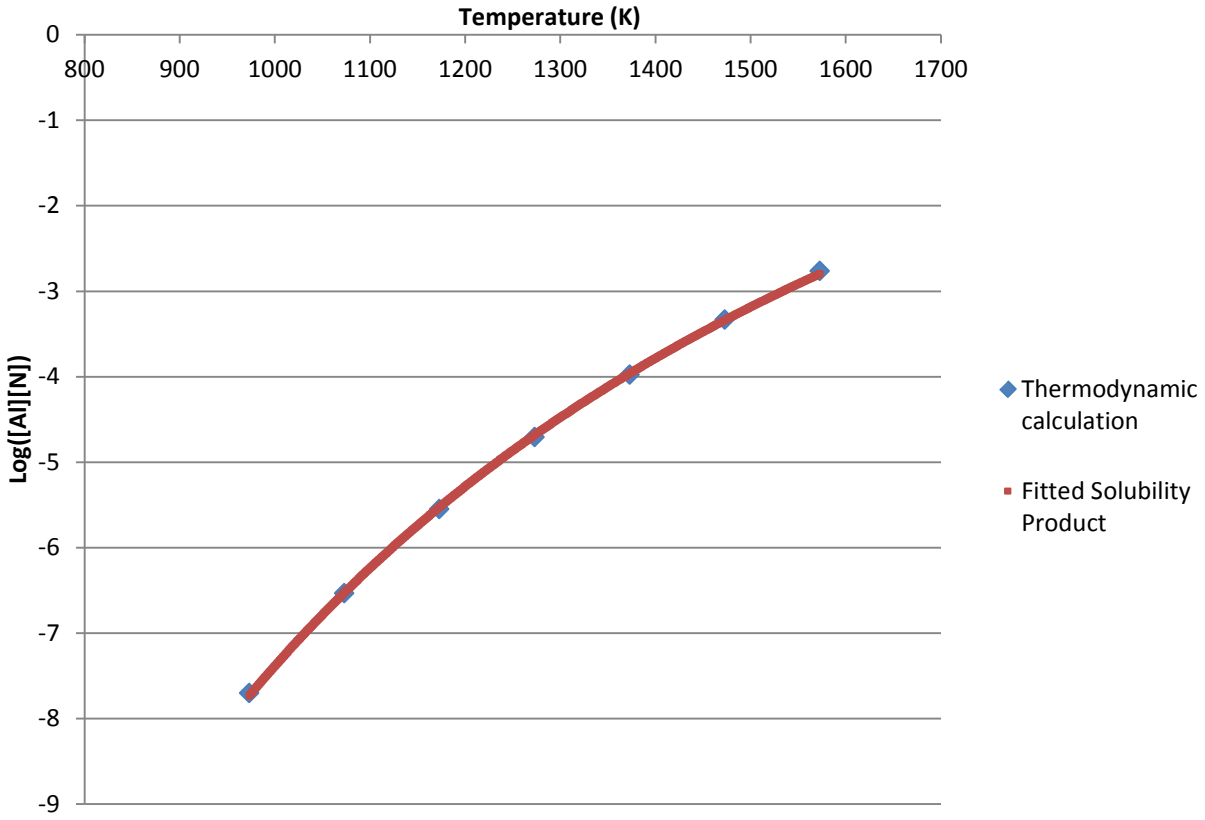

Figure 75: Calculated AlN free energy of formation and fitted solubility curve

Since the value of the free energy of AlN formation is in units of J/mol, it is necessary to divide by the molar volume of AlN to convert to J/m^3 as required for the calculation of ΔG^*. The molar volume of AlN as a function of temperature is approximated from the data of Bruls et al.[113].

$$V_m^{AlN} = (2.36202x10^{-5}T + 1.2490099245)x10^{-5}$$

in m^3/mol.

The strain energy, ΔG_s, is the energy associated with the misfit of AlN precipitate volume in the steel matrix. According to Russell[114], the excess vacancies available at grain boundaries are able to accommodate the strain energy term so that this term could in theory be neglected.

However, even in the presence of excess vacancies it does not seem a reasonable assumption to allow the precipitates to form without any strain on the surrounding matrix. The strain energy is commonly expressed as[22]

$$\Delta G_s = \frac{E}{1-\nu_M}\varepsilon^2$$

where E is the elastic modulus of the matrix, ν_M is the Poisson ratio of the matrix and ε is the linear misfit strain. Radis[22] approximates the linear misfit strain as

$$\varepsilon = \frac{1}{3}\frac{V_m^P - V_m^M}{V_m^M}$$

where $V_m^{P,M}$ represents the molar volume of the precipitate (superscript P) or matrix (superscript M). A more elaborate treatment of the strain energy is given by Liu and Jonas[115]:

$$\Delta G_s = \frac{2}{3}\mu_M(\Delta^*)^2\frac{\alpha}{\alpha + (1-\alpha)\frac{K_M}{K_P}}$$

with μ_M being the shear modulus of the matrix, Δ^* the effective cubic dilation and the elastic parameters are given as (with subscript M and P denoting matrix and precipitate, respectively):

$$\alpha = \frac{1+\nu_M}{3(1-\nu_M)}$$

$$K_M = \mu_M[2 + \frac{3}{(1-\nu_M)}]$$

$$K_P = \mu_P[2 + \frac{3}{(1-\nu_P)}]$$

Interfacial energy, σ, is comprised of two additive terms

$$\sigma = \sigma_c + \sigma_s$$

where σ_c arises from the bonds between the precipitate and matrix atoms and σ_s is a structural term corresponding to the necessary dislocations that form within the matrix or precipitate to

accommodate the lattice misfit. Liu and Jonas[115] calculate the interfacial energy between a nucleus and the matrix in terms of a coherency loss parameter, C, which is given as

$$C = \frac{\delta_p}{\delta}$$

where δ_p is the plastically accommodated disregistry and δ is the total lattice disregistry. The value of δ is given as

$$\delta = \frac{(a_p - a_m)}{a_m} = \delta_e + \delta_p$$

where a_p and a_m are the lattice parameters of the precipitate and matrix, respectively, and δ_e is the elastically accommodated disregistry. By the manner in which Liu and Jonas defined the coherency loss parameter, it can vary only between zero (for a fully coherent precipitate) and one (for an incoherent precipitate) and they define the interfacial energy as

$$\sigma = \sigma_c(1 - 2C\delta) + \sigma_s$$

In the present model, the AlN precipitates may be chosen as fully coherent FCC nuclei or as fully incoherent HCP. The linear misfit is approximated using the volumetric misfit, ε, according to

$$\xi = \frac{\varepsilon}{3}$$

where the volumetric misfit is calculated by

$$\varepsilon = \frac{V_m^{AlN} - V_m^{\gamma}}{V_m^{\gamma}}$$

The grain boundary energy, γ_{gb}, is an important term in that it reduces the overall energy required for nucleation through elimination of some amount of grain boundary area. Cheng[112] used constant values of γ_{gb} = 0.65 – 0.85 J/m^2 in his work and concluded that the most reasonable

results were achieved by using 0.75 J/m^2. The present work uses a temperature-dependent expression for grain boundary energy given as[116]

$$\gamma_{gb} = 1.3115 - 0.0005T$$

The amount of grain boundary removed by a spherical precipitate may be estimated as πr^2 which is the maximum precipitate cross section. Maximizing the grain boundary area removed will minimize the necessary energy to form a precipitate and is therefore energetically favorable. The interfacial energy and grain boundary energy both contribute to the free energy of nucleation in proportion to r^2 so it is convenient to define an effective surface energy as

$$\sigma_{eff} = \sigma + \frac{\gamma_{gb}}{f\left(\frac{c}{a}\right)}$$

where in the present case of spherical precipitates $f\left(\frac{c}{a}\right)$ has a value of 4, but in the case of spheroid precipitates $f\left(\frac{c}{a}\right)$ is a shape function based on the ratio of the defining axes. For the sake of completeness the shape function is noted as

$$f\left(\frac{c}{a}\right) = \frac{1}{2} + \frac{2c}{a} + \frac{2a}{c} - \frac{c^2}{2a^2}$$

By describing the effective surface energy it is now possible to exclude the entire grain boundary term from the definition of ΔG^*, and the necessary terms for calculating ΔG^* have now been defined.

In the case of precipitation occurring within the grains it is considered that dislocations would be a preferential site for nucleation. For dislocation precipitation the grain boundary energy contribution is not used and the solution for r^* is instead based on the decreased energy by removing part of a dislocation. Following the method outlined by Kozeschnik[117], the precipitate will remove some part of the dislocation core and the energy decrease can be

approximated by the dislocation line energy removed. The energy associated with removing a section of the dislocation core is given as:

$$\Delta G_{disl} = Gb^2r$$

where G is the shear modulus of the matrix, b is the Burger's vector and r is the radius of the precipitate, in this case the radius of a critically-sized nucleus. The energy associated with removal of a dislocation is linearly related to the nuclei radius while the energy due to removal of a section of grain boundary is proportional to r^2. The effective surface energy term that is used in order to simplify precipitation on the grain boundaries cannot be used when considering precipitation on dislocations for this reason.

N – Number of potential nucleation sites

The number of potential nucleation sites for homogeneous nucleation is simply the number of atomic sites per unit volume. The present model is concerned with grain boundary precipitation and so the number of potential nucleation sites is calculated as

$$N = 14.61x10^{18}A_{gb}$$

where A_{gb} is the grain boundary area which is approximated as

$$A_{gb} = \frac{3}{grainsize}$$

The term $14.61x10^{18}$ is the number of atoms per square meter on the close-packed plane of austenitic iron. The resulting value matches well with those in the literature[117].

Z – Zeldovich non-equilibrium factor

The physical significance of the Zeldovich factor is that it accounts for the non-equilibrium concentration of critical-sized nuclei and the portion of critical-sized nuclei which do not

continue to grow. There are several expressions for the Zeldovich factor in the literature. Kozeschnik[117] gives the Zeldovich factor in the form

$$Z = \left[-\frac{1}{2k_bT}\left(\frac{\partial^2 \Delta G^*}{\partial n^2}\right)\right]^{\frac{1}{2}}$$

where the term $\left(\frac{\partial^2 \Delta G^*}{\partial n^2}\right)$ is the second derivative of the Gibb's free energy of forming a cluster of n molecules, evaluated at n^*. By substituting the spherical precipitate volume, $\frac{4}{3}\pi r^3$, with the sum of molecular volumes, $n\Omega$, the value of $\left(\frac{\partial^2 \Delta G^*}{\partial n^2}\right)$ can be determined. After re-arranging with such substitutions, the Zeldovich factor as used in the present model is written as

$$Z = \frac{(\Delta G_v + \Delta G_s)\left(\frac{V_m^{AlN}}{N_A}\right)}{8\pi(k_bT\sigma_{eff}^3)^{\frac{1}{2}}}$$

β^* - Atomic attachment frequency

The atomic attachment frequency is the rate at which atoms jump across the interface from the matrix to the precipitate. Johnson et al.[118] give the following expression for β^*

$$\beta^* = \frac{16\pi\sigma^2 D_{Al}^{\gamma} X_{Al}^{\gamma}}{a^4(\Delta G_v + \Delta G_s)^2}$$

For the present model the value of σ is replaced with σ_{eff} in order to account for the contribution of grain boundary energy to give

$$\beta^* = \frac{16\pi\sigma_{eff}^2 D_{Al}^{\gamma} X_{Al}^{\gamma}}{a^4(\Delta G_v + \Delta G_s)^2}$$

τ – Incubation time

The incubation time, τ, is noted in the literature[117] as the time that is required for isothermal nucleation to reach the steady state rate. Incubation time can be written as

$$\tau = \frac{1}{2\beta^* Z^2}$$

for solid-state precipitation.

In the present model the incubation time is recalculated at each time step. The value of hold time is reset to one second for all cases where ΔG^* is less than or equal to zero, and incremented by the time step (one second) for all cases where ΔG^* is greater than zero.

7.2 GROWTH, DISSOLUTION AND COARSENING

Growth, dissolution and coarsening are accounted for by using a single equation which is derived and applied in a manner similar to that shown in the work of Cheng[112] and Maugis[119]. In both cases, the classical Zener growth theory is applied[120]. Cheng included grain boundary diffusion, which in this work is ignored due to the exceedingly large as-cast grain size. The governing equation is

$$\Delta r = -k\left(\frac{D_{Al}^{\gamma}}{r}\right)\Delta t$$

where Δr is the change in the radius and k is the concentration gradient, defined by

$$k = \frac{C_i - C_m}{C_p - C_i}$$

The concentration of aluminum in the matrix, C_m, is re-calculated at each time step and each growth step. C_p is the aluminum concentration in the precipitate and C_i is the aluminum

concentration at the precipitate/matrix interface. The effective interface concentration is increased significantly for small precipitates with a high radius of curvature due to the Gibbs Thomson effect. The correction to the equilibrium interfacial concentration, C_e, is given[112] as

$$C_i = C_e e^{\frac{2\sigma_{eff} V_m^{AlN}}{RTr}}$$

and C_e is calculated from the solubility product. The Gibbs Thomson effect is quite significant at small precipitate sizes and care must be taken in calculating the growth of precipitates immediately after nucleation as will be discussed in section 7.3. The precipitate will shrink when k is positive and grow when k is negative.

7.3 MODELING APPROACH

Inputs and outputs of the present model are given in Table 15, below. At each time step, the nucleation rate is calculated and the number of nuclei formed at time, t, during the period Δt is then set as N(t). For each N(t) the starting radius is assigned to a radius distribution matrix at the position r(t,i).

Table 15: Inputs and outputs of precipitation model

Model Inputs	**Model Outputs**
Temperature profile	AlN precipitate radius distribution
Al, V, N content (wt%)	VN precipitate radius distribution
AlN solubility product	AlN volume fraction precipitated
Austenite grain size	VN volume fraction precipitated

The starting radius must be slightly larger than the value of r^* in order to prevent immediate dissolution of all precipitates formed at each time step. According to Perez[121] the precipitate radius is stable upon reaching a value of $r^*_{k_bT}$, which is calculated from

$$r^*_{k_bT} = r^* + \frac{1}{2}\left(\frac{k_bT}{\pi}\right)^{\frac{1}{2}}$$

The value of $r^*_{k_bT}$ is the radius size where the free energy is reduced by a small amount, k_bT, beyond the inflection point that occurs at r^*. A graphical representation of the starting radius compared to r^* is shown in Figure 76.

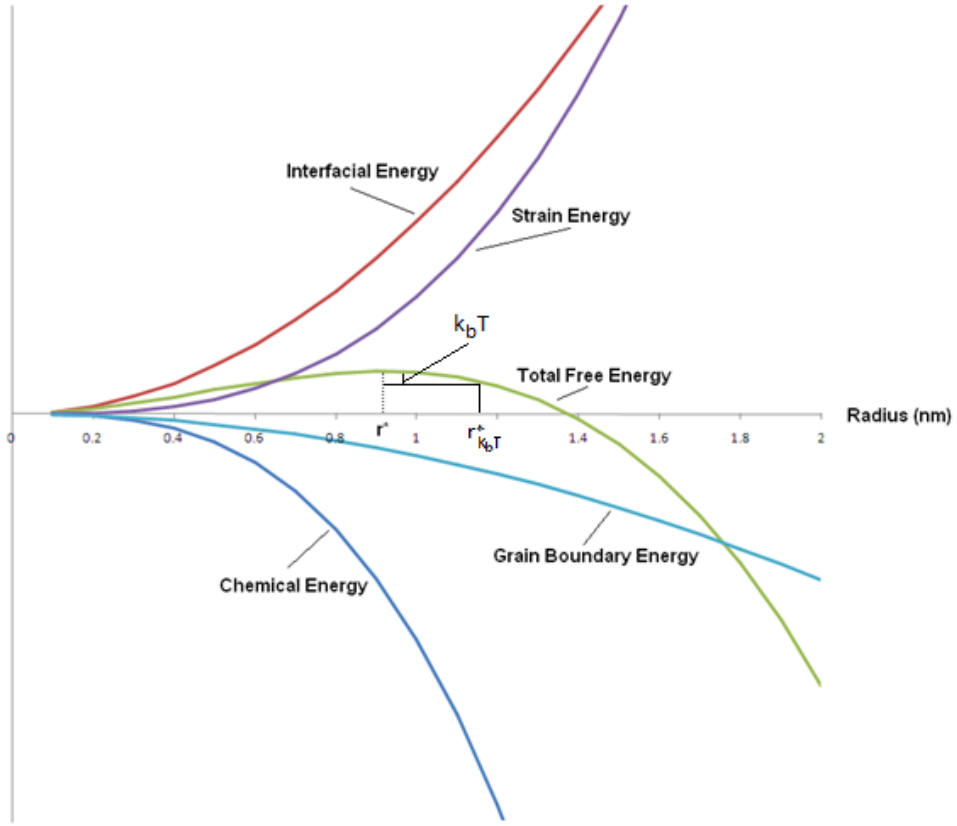

Figure 76: Graphical representation of the starting precipitate radius

After the precipitation for a given time step has occurred, each of the previously formed precipitates is allowed to grow or dissolve independently according to the method outlined in section 7.2. At each time step and each growth step the remaining Al and N matrix concentration is recalculated.

When precipitates are first nucleated, the very small radius drastically increases the effective interface concentration due to the Gibbs Thomson effect. The typical time step used in the present model is one second, which gives a significant overestimate of the initial growth of small precipitates due to the rapid reduction in growth rate as the particle size increases. The model is able to provide a reasonable value for the growth of a small particle with the use of a nested loop in the program where much smaller time steps are used and accumulated until the full 1s base time step for the overall model has been achieved. This prevents the rapid growth rate at the start of a 1s time step from carrying through for the entire second.

7.4 RESULTS OF PRECIPITATION MODEL

The precipitation model showed that when the HCP lattice parameters of AlN are used it is not possible to overcome the volumetric strain of forming a precipitate within the matrix. From section 7.1 it is clear that when the volumetric strain term, ΔG_s, is larger in magnitude than the volumetric free energy term, ΔG_v, then the nucleation process cannot begin without assuming an unreasonable value for the grain boundary energy (or dislocation energy in the case of precipitation within the grains). Figures 77 and 78 show the calculated values of ΔG_v, ΔG_s and $\Delta G_v + \Delta G_s$ for the HCP and FCC AlN structures, respectively. All data shown are for steel C unless otherwise noted.

When the model considers the FCC structure for AlN formation, nucleation begins at 1048°C according to the thermodynamic analysis of solubility that was presented in section 7.1. The precipitation rapidly consumes the grain boundary area when coarse as-cast grains of ~1000 μm are considered. Precipitation of AlN on matrix dislocations begins at 996°C. No precipitation of VN occurs due to consumption of the nitrogen and reduction of potential nucleation sites. If the HCP lattice parameters for aluminum nitride are used there is no AlN precipitation at the austenite grain boundaries or within the grains. Instead, VN begins to precipitate at 871°C, but not to any significant volume fraction unless a relatively slow cooling rate is used (<0.2°C/sec).

Changes to the cooling rate do not have a great effect on the precipitation start temperature. However, slower cooling rates lead to higher volume fraction of precipitates at a given temperature due to additional time at high temperature when diffusion is fastest. This is shown in Figure 79 (FCC structure is assumed) where the final volume fraction of AlN at grain boundaries and on dislocations is shown for various cooling rates.

The choice of solubility product has a pronounced effect on the precipitation temperature and volume fraction. A comparison of precipitation start temperatures, precipitated volume fraction of AlN at 800°C, and equilibrium solution temperatures for various solubility products are shown in Table 16 for steel C cooled at 1°C/sec. The wide range of values for both precipitation start temperature and volume fraction AlN at 800°C shows that the precipitation model is extremely sensitive to input data.

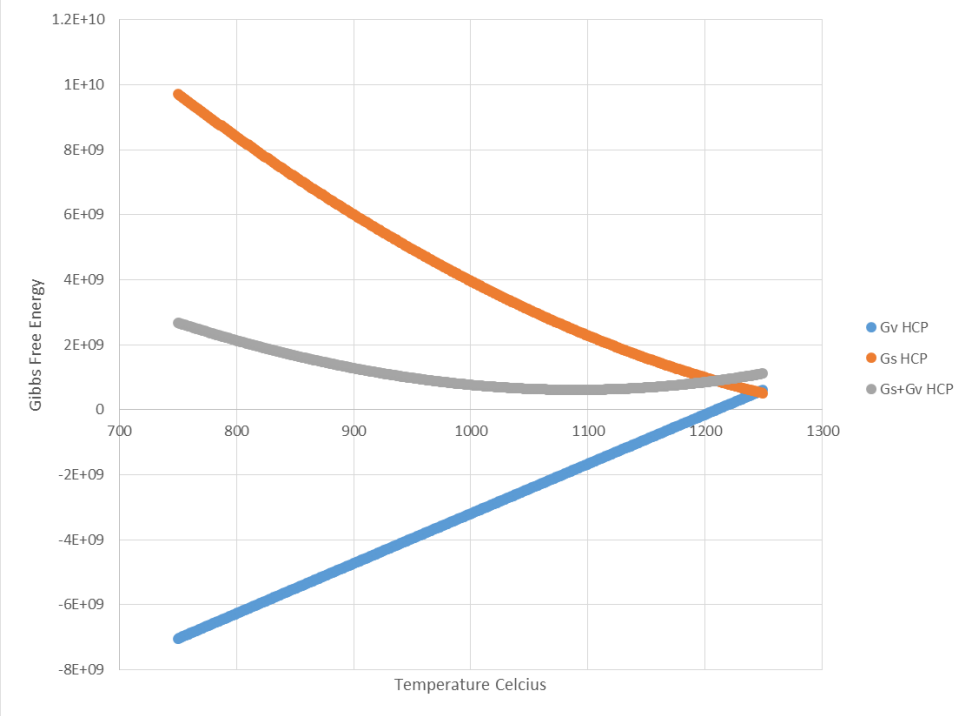

Figure 77: Chemical (G_V) and strain (G_s) energy terms for HCP AlN structure

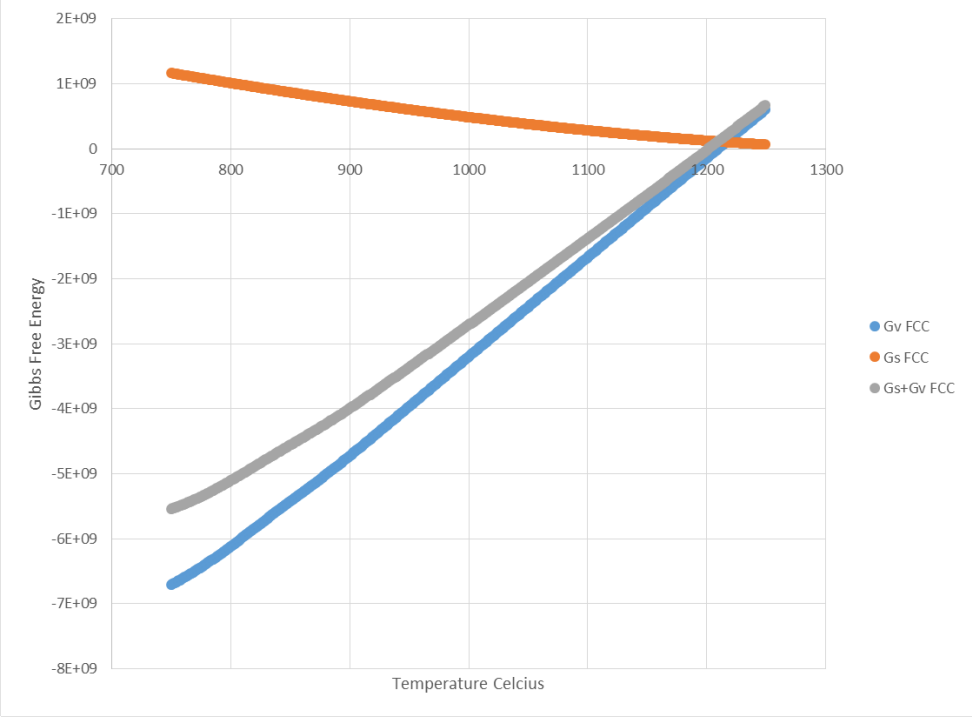

Figure 78: Chemical (G_V) and strain (G_s) energy terms for FCC AlN structure

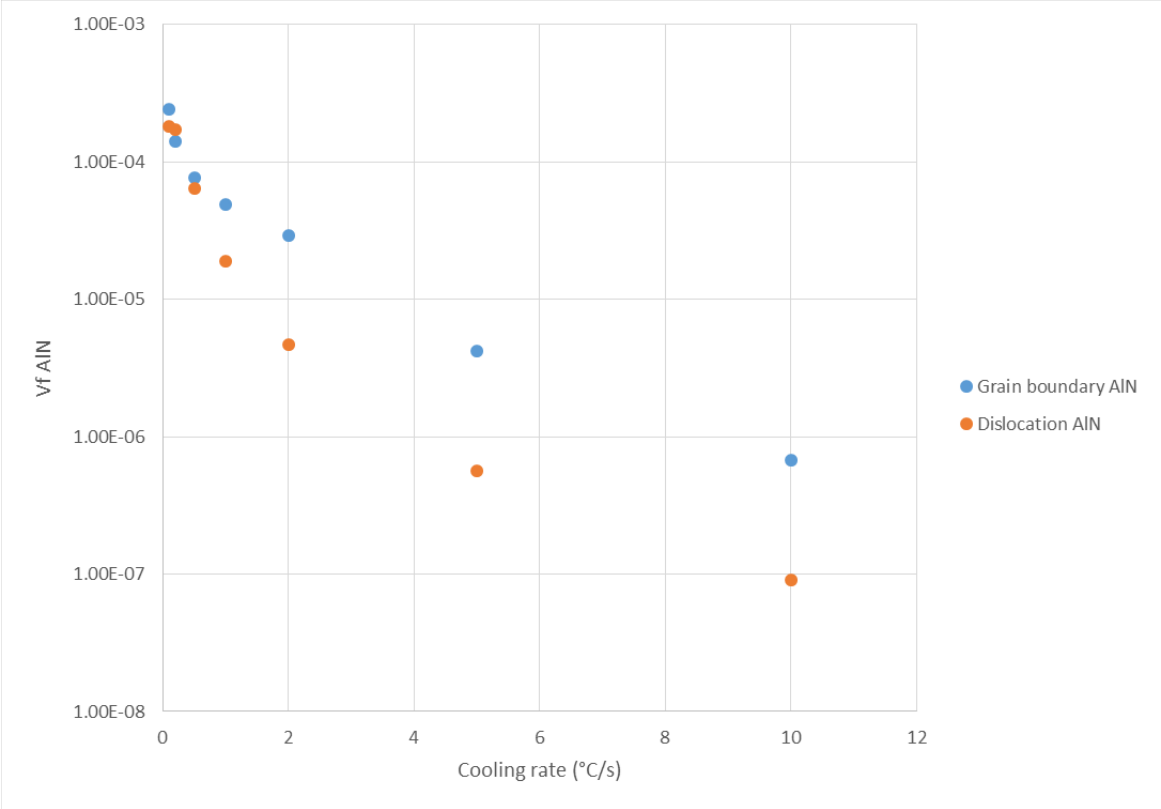

Figure 79: Effect of cooling rate on volume fraction of AlN

Table 16: AlN precipitation model results for various solubility products

Sol. Prod. Reference	$T_{sol, eq}$ °C	$T_{precip\ start}$ °C	$V_{f\ GB\ AlN}$	$V_{f\ disl\ AlN}$
Present work	1209	1048	$4.9x10^{-5}$	$1.9x10^{-5}$
49	1141	NA	0	0
51	1296	939	$3.5x10^{-22}$	0
52	1269	836	$6.6x10^{-23}$	0
52	1401	1000	$3.2x10^{-21}$	0
50	1142	NA	0	0
53	1251	953	$2.3x10^{-14}$	0
54	1301	998	$9.9x10^{-12}$	0
36	1377	1169	$1.4x10^{-4}$	$5.3x10^{-6}$
55	1187	970	$2.0x10^{-9}$	$1.1x10^{-11}$
55	1188	947	$2.1x10^{-11}$	$1.2x10^{-14}$
45	1194	1014	$3.6x10^{-6}$	$2.4x10^{-7}$
47	1209	1069	$7.7x10^{-5}$	$3.9x10^{-4}$
46	1173	980	$7.1x10^{-8}$	$1.8x10^{-9}$
56	1216	824	$2.1x10^{-23}$	0
57	1285	822	$7.6x10^{-24}$	0

8.0 DISCUSSION

There is little published information available regarding the hot ductility of large-grain, as-cast, slow-cooled steels. A thorough understanding of the effects of thermal path and composition on hot ductility can provide ingot producers and forgers with the fundamental information necessary for well-designed thermal handling and processing procedures. In this section the experimental results are analyzed and interpreted within the context of large cross-section ingots.

8.1 EVALUATION OF EMPIRICAL AND METALLURGICAL RESULTS

The results of the direct cooling to test temperature showed ductility troughs that were in reasonable agreement with similar works. Steel C shows a significant drop in ductility starting in the temperature range of 900°C - 1050°C on direct cooling to the test temperature after solidification. This temperature range is generally consistent with the start of aluminum nitride precipitation according to previous researchers [122,123,124] and the precipitation model presented in this work. Figures 80 - 82 show various TTT curves for AlN formation from the literature. There was essentially no ductility loss in steel B until around 900°C and no ductility loss in steel A until 800°C. In the direct cooling experiments, the loss in ductility of steels A and B was related to a reduction in the extent of dynamic recrystallization as temperature was decreased below 900°C. The further reduction in ductility as temperature is decreased is due to a reduction

in thermally activated softening mechanisms such as recovery. The large drop in ductility of steel C showed a brittle intergranular failure that was found to be associated with a thin carbide film at the prior austenite grain boundaries.

The result of sample C-20 (identical to sample C-10 except that the testing temperature was increased from 1000°C to 1100°C) showed that the loss in ductility due to undercooling and reheating is not a result of permanent damage to the microstructure. Low alloy steel ingots are typically forged at temperatures greater than or equal to 1200°C, well above the temperature of ductility recovery shown in sample C-20. Therefore it should be expected that low alloy steels have the necessary hot ductility to avoid cracking during the initial forging operations.

Perhaps the most interesting empirical results of this work are the improved ductility of steel C in the undercooling experiments as compared to steels A and B. The improved ductility occurs at 800°C undercooling temperature and also for extended hold times at 900°C the ductility improves with increasing AlxN product and increased hold time. In absence of the metallurgical analysis this effect may have been attributed to coarsening of AlN precipitates during the hold at 900°C. Steel C is a hyperstoichiometric composition, and aluminum would be the rate-limiting element during growth of the precipitate, so it should be anticipated that the precipitates in steel C would coarsen at a faster rate than the other materials tested. Knowing that a carbide film of M_7C_3 is present on the fracture surface, it is more likely that the increased time at 900°C is affecting the type of carbide that forms. In the work of Djebaili[125] et al. they find that fine M_7C_3 precipitates give way to relatively large M_6C and $M_{23}C_6$ during high temperature holding. The M_7C_3 film was not identified within any of the non-deformed or high ductility samples of the present work. Most likely very fine MX precipitates are forming at austenite grain boundaries causing pinning and retarding the recrystallization. With longer hold

times at 900°C the fine MX coarsens to the point of being ineffective for pinning and retarding dynamic recrystallization during the early stages of deformation.

Steel D did not exhibit the severe ductility loss on direct cooling to the temperature range of 950°C - 1050°C. This steel had an aluminum content similar to steel B, but an increased nitrogen content similar to steel C. The results of direct cooling to test temperature for steel D compared to steel C imply that the increased nitrogen content on its own is an insufficient condition for the reduction in hot ductility over the temperature range tested.

The thermal strain experiments showed a sharp increase in the load at approximately 1070°C for steels B and C, while steel A did not show a corresponding increase until almost 50°C lower temperature. In these experiments, the samples were subjected to a small continuous load due to the thermal contraction during cooling. The constant load would aid the precipitation by reducing the strain free energy term when the matrix lattice is expanded during elastic strain. The increase in load for steel C at 1070°C agrees reasonably well with the initial drop in ductility from the direct cool to test temperature experiments.

Deformation was clearly shown to enhance the segregation present in the steels of this work. In the undeformed state the segregation was slightly higher in steel C compared to steel B. Chromium, molybdenum and vanadium were segregated in the as-cast structure prior to deformation, and the extent of segregation was increased during the deformation process. This enhanced uphill diffusion during deformation as has been identified in previous works[34,96].

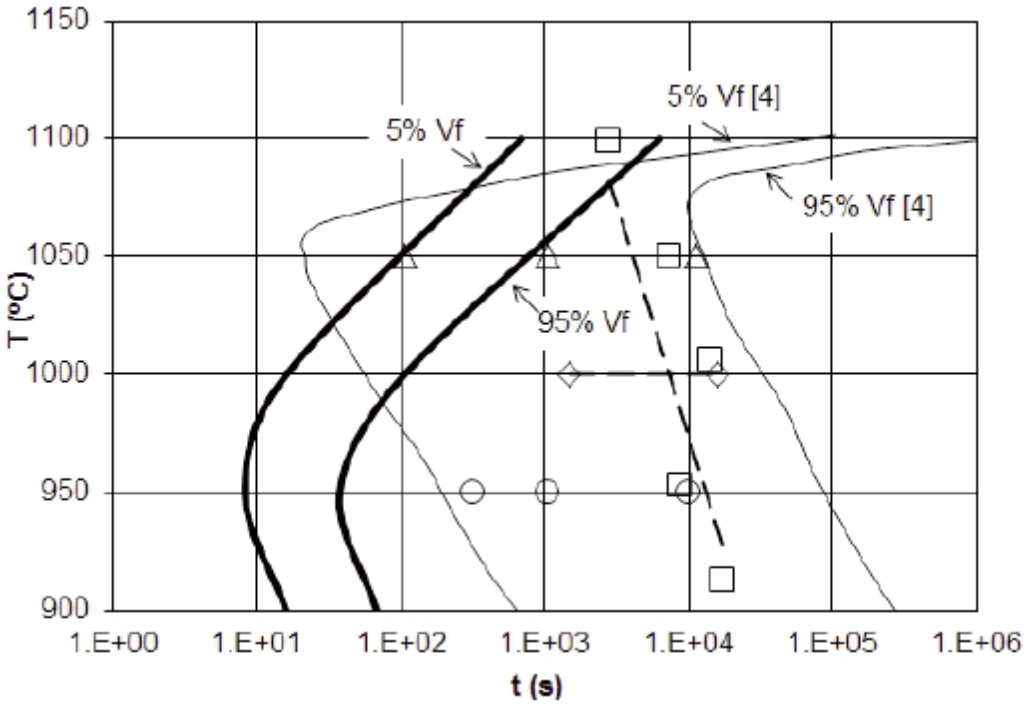

Figure 80: TTT diagram for AlN from [122], light and dark lines from different models

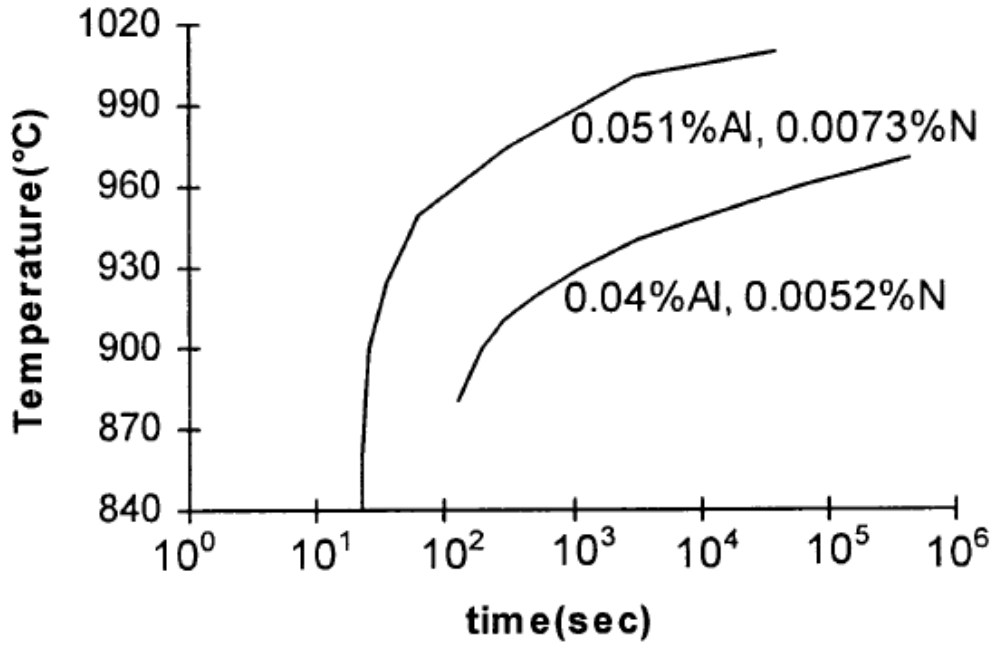

Figure 81: TTT diagram for AlN from [123]

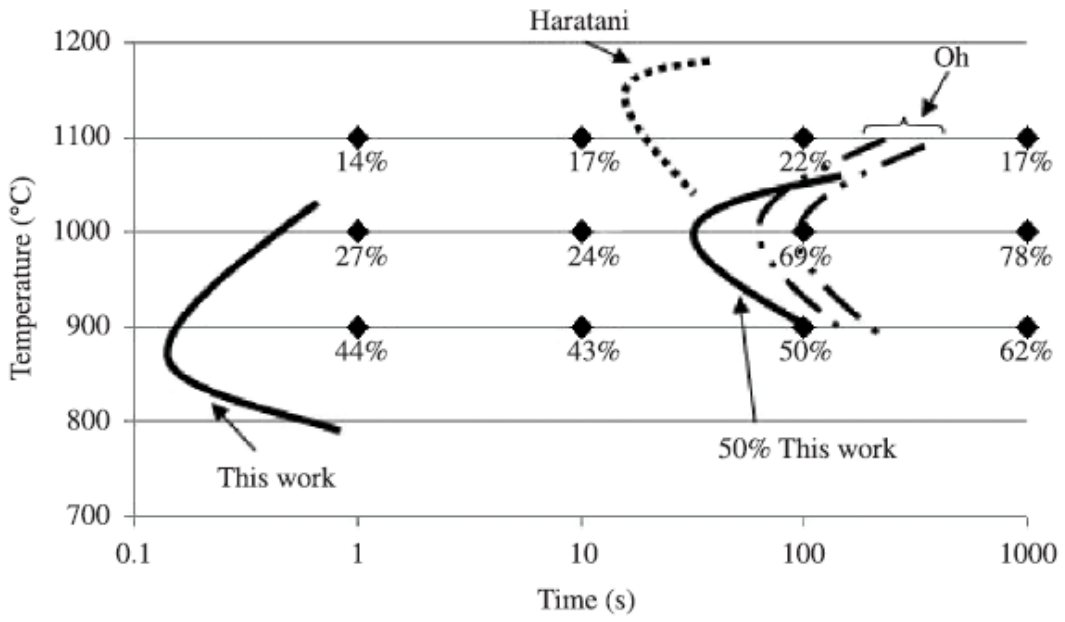

Figure 82: TTT diagram for AlN from [124] including comparison to other works

8.2 PRECIPITATION MODEL

The precipitation model described in this work accounts for both AlN and VN precipitation in austenite. No assumptions were made without some reasonable metallurgical justification. The model predicts that AlN with the stable hexagonal structure is not able to precipitate in austenite at the compositions of P20 steel examined in this work. The primary reason for this is the volumetric misfit and associated strain energy term, ΔG_s, of precipitating the HCP structure within the FCC austenite. As noted previously, AlN has been suggested to precipitate in a metastable FCC structure and then later transform in to the stable HCP structure. When the precipitation is allowed to occur in this manner within the precipitation model of this work, there can be significant AlN volume fraction precipitated at the temperatures where low ductility was

identified from the empirical results. However, the FCC AlN grows very rapidly due to the high diffusion coefficient of Al in iron (aluminum being the rate limiting element) to sizes which would rapidly saturate the prior austenite grain boundaries with an aluminum nitride film. Based on the results of the metallurgical analyses in the present work, this is not occurring. In thin films of AlN deposited on an FCC substrate of VN, other research[126] has shown that the AlN layers initially take an FCC structure at thicknesses < 4 nm, and then further from the substrate the HCP AlN structure is present. It is possible that there is AlN formation as FCC precipitates of < 4 nm in size in this material which would be at or beyond the detection limits of the equipment being used in this work. Some energy barrier must be present at the AlN_{FCC} → AlN_{HCP} transition but there is no information available in the literature regarding this transformation.

VN precipitation for the P20 compositions is shown to be possible in austenite by the precipitation model. Precipitation starts at a temperature of approximately 870°C when the nitrogen content of 130 ppm is used. The MX-type precipitates were found to be a minor constituent of the carbide film that was formed on austenite grain boundaries in the present work.

8.3 CARBIDE PRECIPITATION

The identification of (Cr, Mo, V, Fe) carbides at the prior austenite grain boundaries of low ductility samples was not anticipated. These carbides would not be expected to form until much lower temperatures or higher alloy contents than those of the P20 steels in this work as shown in the solubility curves in Figure 83.

According to Figure 83 the solubility of chromium and molybdenum carbides at approximately 1000°C would require minimum 1 $(at\%)^2$ of (Mo x C) content and approximately 5 $(at\%)^2$ of (Cr x C), which is higher than the bulk composition of the P20 steels examined. However, Hartshorne et al.[127] have shown similar carbide formation in a high-strength alloy steel after direct quenching from temperatures in the austenite range. Their work using Atom Probe Tomography gave clear evidence of carbon and molybdenum segregation to the austenite grain boundaries and carbide precipitation at temperatures higher than would typically be expected. Nachtrab and Chou[34] demonstrated carbon segregation at deformed austenite grain boundaries up to 6.5 times the bulk carbon content. Lim et al.[128] showed carbon segregation at prior austenite grain boundaries of over 4.5 times the bulk concentration in samples quenched from 1100°C to room temperature; phosphorus segregation was also present in their work.

The segregated compositions from the EPMA analysis were used as input to the thermo-physical modeling software JMatPro for analysis of the anticipated phase transformations. Figures 84 – 88 show the results of the JMatPro equilibrium phase wt% analysis for the following EPMA results:

- Steel B matrix – undeformed
- Steel B segregation band – undeformed
- Steel C matrix – undeformed
- Steel C segregation band – undeformed
- Steel C segregation band – deformed

The segregation band compositions used were those with the maximum content of alloying elements (minimum iron content) rather than the average. This was done to so that the maximum potential for carbide formation would be shown. The onset of ferrite formation from

the JMatPro analysis occurs 30°C - 40°C lower than was observed in the dilatometry experiments, but is very close to the value predicted by Andrews' equation[38] from section 2.3.1. The JMatPro analysis of the segregation band composition from deformed sample C-03 shows that M_7C_3 precipitation on cooling will begin at approximately 1067°C. This temperature agrees well with the initial loss in ductility at 1050°C on direct cooling of steel C. The M_7C_3 precipitate is predicted to be stable down to a temperature of 914°C at which point the $M_{23}C_6$ carbide becomes more stable. This agrees with the recovery in hot ductility that is found on cooling to temperatures below 950°C.

Relatively small (<200 nm) carbides with similar composition to the M_7C_3 film were also found in various samples below the fracture surface. Figures 89 and 90 show a TEM bright field image of the carbide particles and the associated EDS analysis found in sample C-04 below the fracture surface.

The very high level of phosphorus segregation from the as-solidified segregation band examined by EPMA is of quite some importance. The phosphorus content of 0.26 wt% within the segregated interdendritic region is over 20 times the bulk phosphorus content of steel C. According to the calculation for determining Ae_3 temperature presented in section 2.3.1, this phosphorus difference would lead to a change in the Ae_3 temperature of approximately 175°C. In the work of Ando and Krauss[129] they show that segregation of phosphorus to austenite grain boundaries accelerates the formation of cementite. Ando and Krauss also suggest in the same work that the earliest cementite that forms may contain phosphorus.

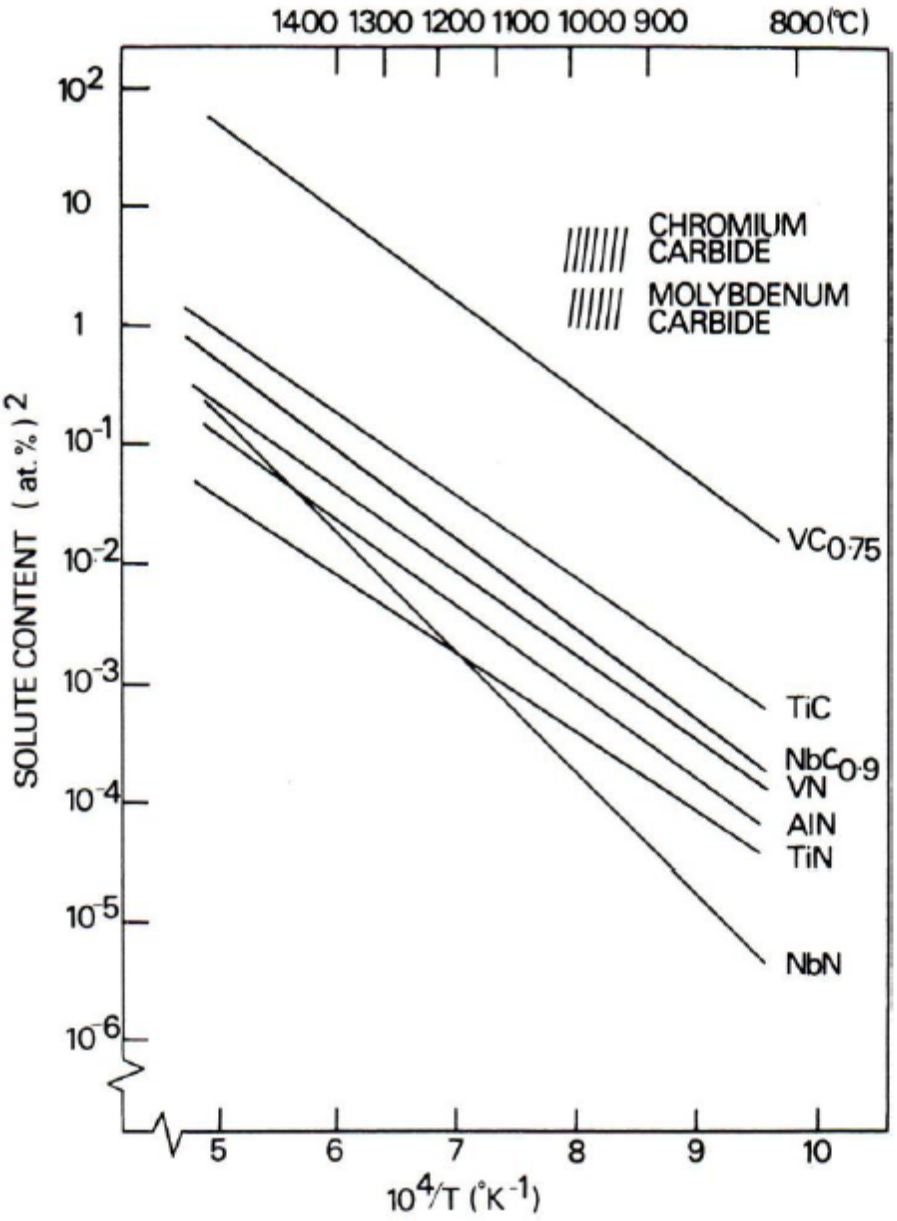

Figure 83: Solubility products of various carbides and nitrides from [130]

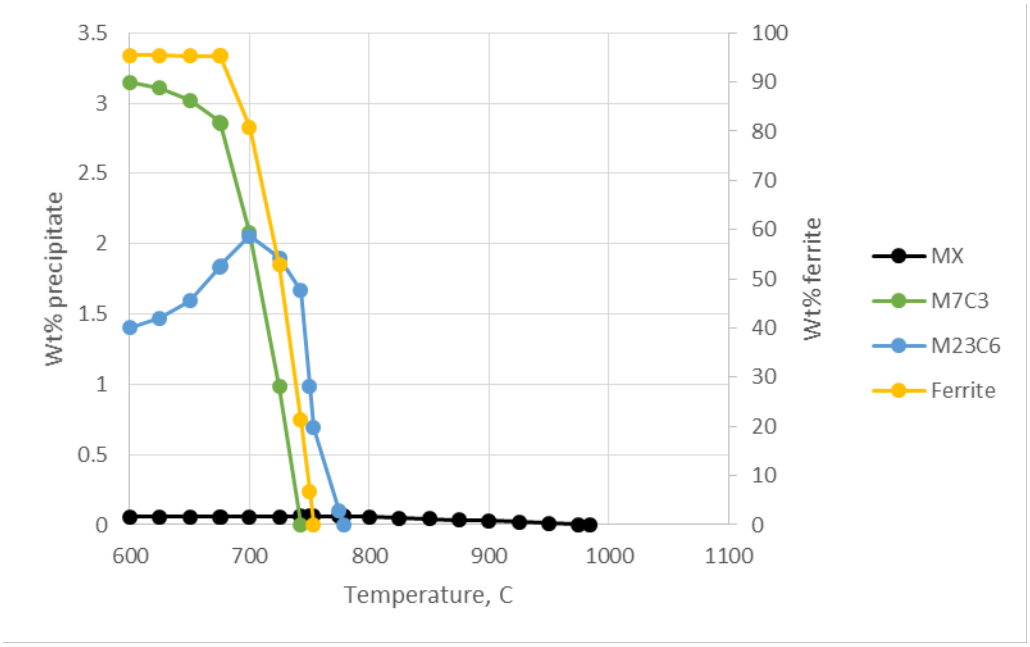

Figure 84: Calculated equilibrium phase forming in undeformed Steel B matrix

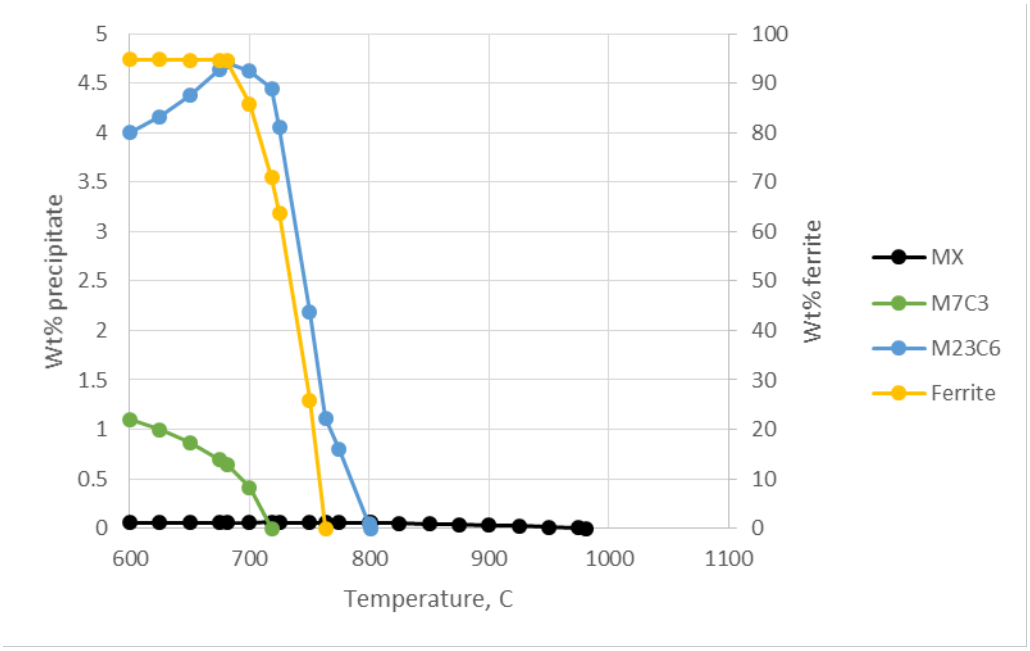

Figure 85: Calculated equilibrium phase forming in undeformed Steel B segregation band

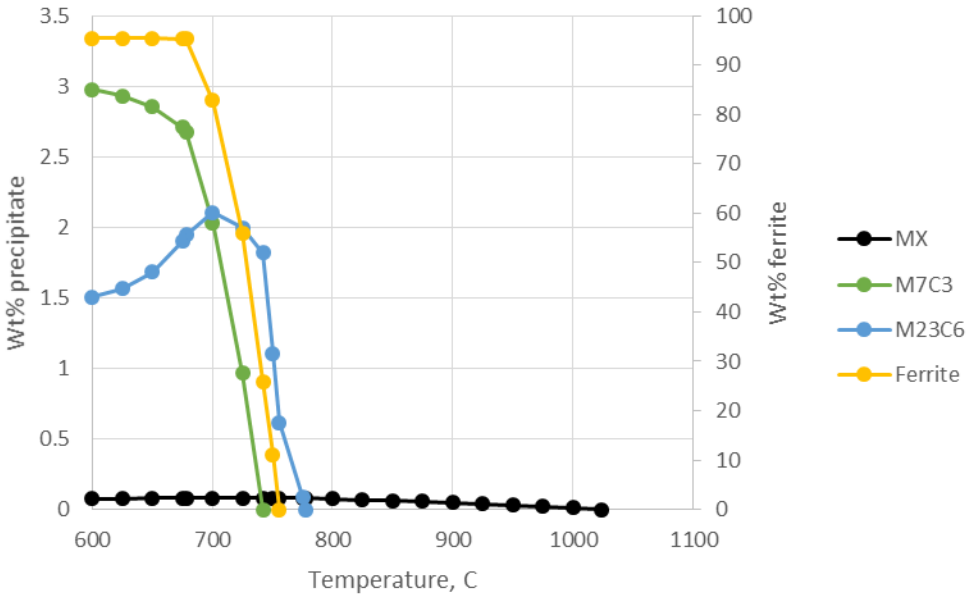

Figure 86: Calculated equilibrium phase forming in undeformed Steel C matrix

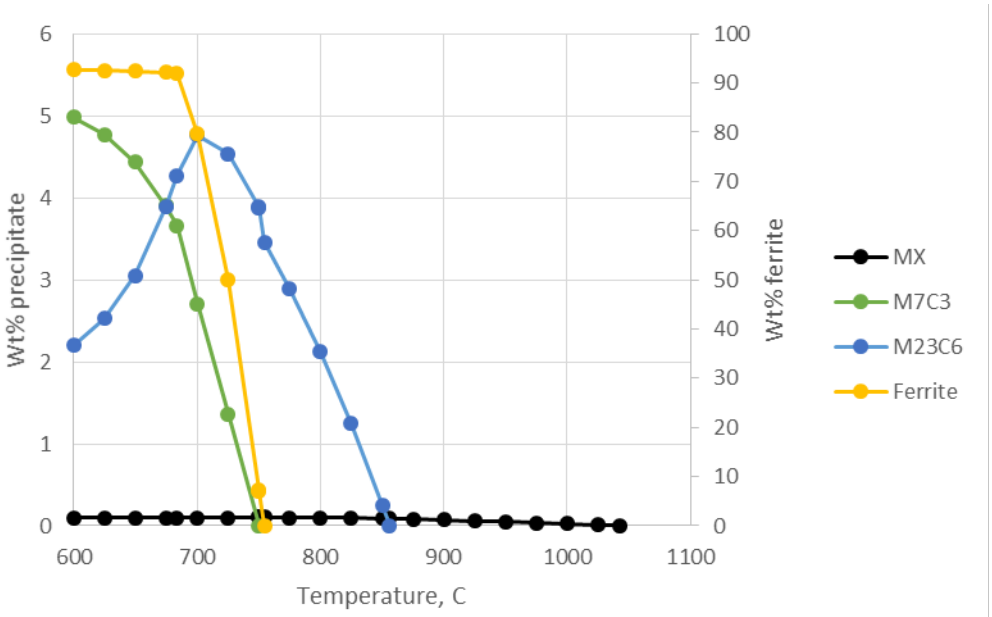

Figure 87: Calculated equilibrium phase forming in undeformed Steel C segregation band

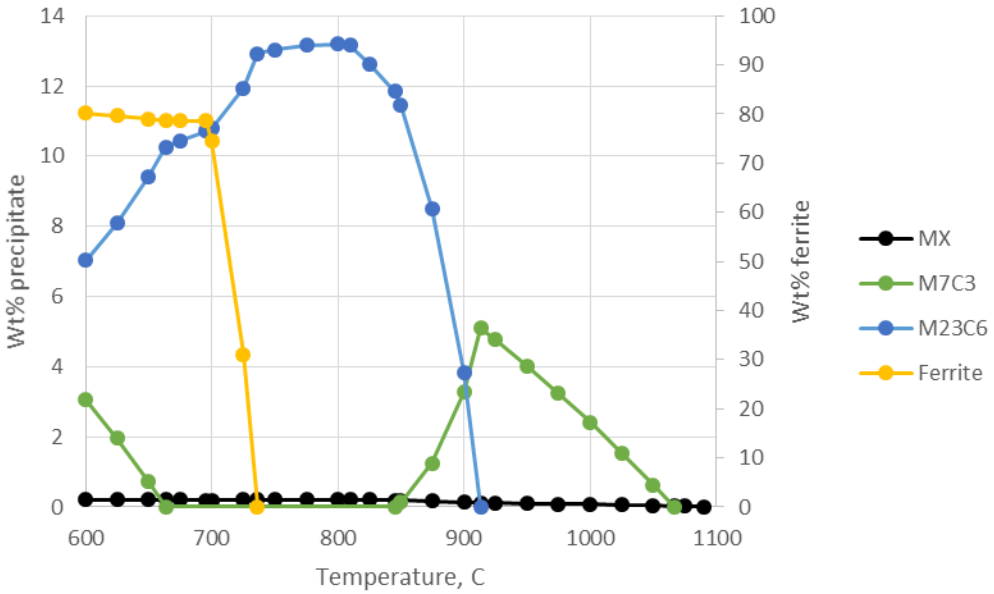

Figure 88: Calculated equilibrium phase forming in deformed Steel C segregation band

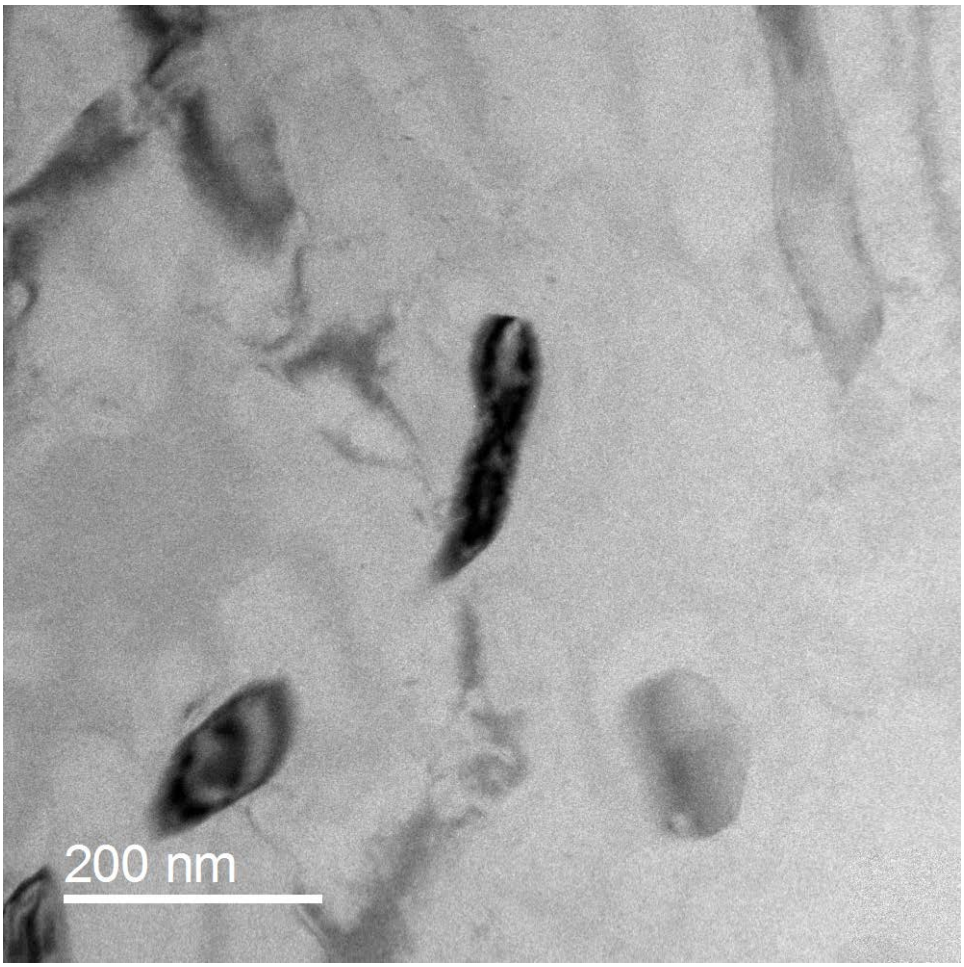

Figure 89: TEM bright-field image of carbide precipitates, sample C-04

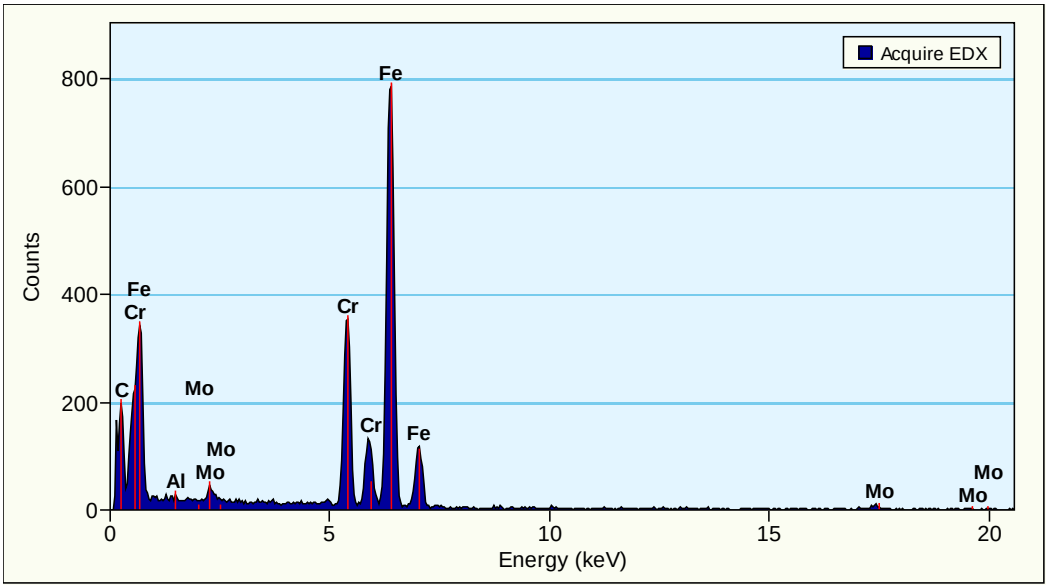

Figure 90: EDS analysis of carbide precipitates, sample C-04

8.4 EFFECT OF AL AND N ON CARBIDE FORMATION

The alloy carbide and V(C,N) film was only present at the intergranular fracture surfaces. No evidence of this precipitation was found in the samples that failed by microvoid coalescence. In the direct cooling from solidification experiments, only steel C exhibited the intergranular type of failure. The empirical evidence in the present work very clearly showed that increased aluminum and nitrogen content can lead to significant ductility loss in the temperature range of 950 - 1050°C. Wang et al[131] show that aluminum has a strong effect on the activity of carbon; ε^{Al}_{C} of 5.3 – 7.76 in liquid iron-based alloys. Although the data from Wang et al. are for liquid iron-based alloy, there is other research[132] showing that the effects of aluminum on carbon in austenite are:

- Increase diffusivity
- Reduce solubility
- Increase activity

There are two possible causes for the effect of increased aluminum and nitrogen on hot ductility of steels in this work. The first is that very fine AlN precipitates are forming and pinning the prior austenite grain boundaries. The pinned boundaries accumulate carbide-forming elements during the deformation process. The combination of immobile austenite grain boundaries and formation of a carbide-film leads to rapid brittle failure along the boundaries. However, no aluminum nitride precipitates were able to be identified in the present work.

The second case would be that AlN is not forming. The effect of aluminum on carbon in austenite increases the solution temperature of alloy carbides. The effect of aluminum additions to coarsen the as-cast structure increases the segregation that occurs during solidification. The reduced solubility of carbides in a heavily segregated austenite grain boundary could lead to

precipitation at a much higher temperature than would be expected from the bulk chemical composition. Ericson[104] identified thin films highly enriched in sulfur, chromium and phosphorus in the interdendritic regions of steel quenched from 1440°C. The chromium and molybdenum contents in Ericson's sample are nearly identical to that of the P20 steels examined in this work. His analysis of the interdendritic thin film was performed on a scanning electron microscope equipped with EDS, and without special care it is very easy to mistake sulfur for molybdenum when making chemical analyses with this equipment. The sulfur K_α energy overlaps with the Mo L_α energy, and the Mo K_α is at a much higher energy that is not visible in the standard energy scale for some instruments. It is likely that the same segregated P, Mo and Cr film was present in Ericson's work as was found in the present work.

8.5 INDUSTRIAL RESULTS

Two industrial trials were performed in order to verify the applicability of this work to large cross-section ingots.

8.5.1 Trial #1: Verification of Crack Network Prior to Forging

It is clear from the results of the hot ductility testing in this work that no loss in ductility should be expected at temperatures above 1100°C. Therefore, low alloy steel ingots at typical temperatures for the start of forging, approximately 1230°C, would not be expected to tear during the initial forging operations due to low ductility of the austenite. Several researchers[48,98,104] have stated that such tears are pre-existing conditions of the ingot while

others[82,86,133] have suggested that the tearing is a result of poor ductility during the forging operation itself. The present work suggests that there must be a pre-existing condition within the ingot and this condition is only exposed during the forging operation.

It was not practical to pre-arrange a set of conditions where cracking would appear during the initial forging operations. Instead, material was selected once cracking during initial forging operations occurred and the following conditions were met:

- Minimum two ingots from the same heat of steel
- One ingot exhibits forge tears during initial forging operations
- Remaining ingot(s) not forged
- Identical thermal handling for all ingots

Such conditions were met on a heat of 3Cr-1.5Mo steel produced at Ellwood Quality Steels as two ingots of 1.3 meter diameter. When tearing of the -01 ingot occurred during the initial forging operations, the -02 ingot was removed from the forging furnace and cooled to room temperature. No cracks were visible on the ingot surface.

The ingot was surface was ground and sprayed with dye penetrant in order to identify if any cracking was present. As shown in Figure 91 there was a large intergranular crack network just below the surface of this ingot. The results indicate clearly that the austenite grain boundary separation occurs prior to the actual forging operation which agrees well with the empirical results presented in this work. A transverse slice of this ingot was taken at 0.5 m from the bottom. The grain boundary crack network was present around the entire circumference, with cracks extending as far as 150 mm below the surface.

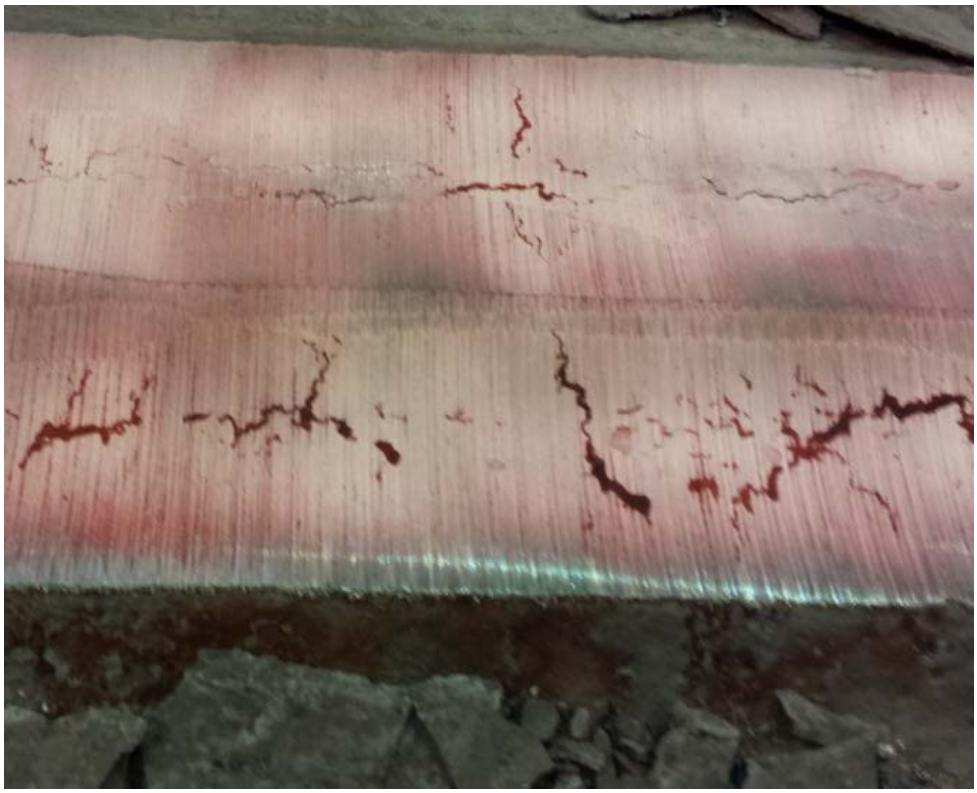

Figure 91: Dye-penetrated intergranular cracking in commercial ingot

8.5.2 Trial #2: Verification of Combined Role of Aluminum and Nitrogen

Nitrogen is becoming a more commonly used alloying element in low-alloy steels. The use of nitrogen for increased yield strength in combination with aluminum for deoxidation can be detrimental to the hot ductility. This trial focused on verification that changing only the nitrogen content in a grade with relatively high aluminum content can cause severe issues with respect to surface cracking. This was an aspect not explicitly examined in the present work.

ASTM A350 LF2 is a common low-alloy steel used for forged flanges, valves and fittings in low-temperature service. The grade is routinely produced by steel ingot suppliers in various cross-sections with no special thermal handling practices. Multiple ingots of 850 x 1200

mm ingots of this material were produced with nitrogen added as an alloying element ([Al][N] = $5x10^{-4}$). Various thermal handling paths were employed as a trial:

A. Strip from mold after solidification / Air cool 2.5 hours / Immediately on forging furnace 1230°C / Begin forging process – Result: **SEVERE TEARS**
B. Strip from mold after solidification / Air cool 2.5 hours / Immediately on tempering furnace 650°C / Air cool / Surface grind – Result: **SHALLOW SURFACE CRACKS**
C. Strip from mold / Air cool 7 hours / On forging furnace 1230°C / Forged – **OK**
D. Strip from mold / Air cool 7 hours / On tempering furnace 650°C / Surface ground (no cracks found) / Heated to forging temperature and forged – **OK**

TEM examination of a sample from ingot B revealed AlN precipitation, see Figure 64 from section 6.4. The TEM sample preparation method was identical to that described previously in this work. The results of this trial indicate that the ingots are in a low ductility state when the short air cooling time of 2.5 hours is employed after stripping from the mold. Longer cooling time leads to improved ductility. The more severe cracking of ingot A implies that the cracking is a result of the thermal stresses which occur during reheating of the ingots. This trial also provided verification of an adequate TEM thin foil sample preparation method for AlN precipitates in steel.

9.0 CONCLUSIONS

- High aluminum and nitrogen content causes a significant ductility loss between 950°C and 1050°C in as-cast P20 steel on cooling slowly from the liquid state. The loss in ductility is shown to be due to the formation of a M_7C_3 film along the austenite grain boundaries. The M_7C_3 film precipitates as a result of microsegregation during solidification and rapid diffusion of substitutional elements during deformation. The effect of increased aluminum and nitrogen content promoting the formation of the M_7C_3 film and the resulting decrease in hot ductility was demonstrated empirically and supporting evidence was identified in the literature.
- The carbide film associated with loss of hot ductility has a significant but inhomogeneous phosphorus content. Phosphorus is known to segregate to austenite grain boundaries and is deleterious to ductility. Furthermore, phosphorus has been found in previous research to accelerate the formation of carbide, increase the Ae_3 temperature and can become incorporated into the first carbides that form. These findings agree well with the results of this work.
- The precise mechanism by which increased aluminum and nitrogen content enhance precipitation of M_7C_3 remains unclear, but may be due to one or a combination of the following factors:

- Aluminum was shown to coarsen the solidification structure and thereby increase the segregation of carbide-forming and tramp elements
- Aluminum increases activity of carbon in austenite
- Aluminum increases diffusivity of carbon in austenite
- Aluminum and nitrogen reduce the solubility of carbon in austenite

- The hot ductility of all P20 steels decreased with decreasing temperature between 700°C and 900°C after slow cooling from solidification temperature due to a reduction in the extent of dynamic recovery. Recovery is a thermally activated process and is well-documented as a softening mechanism necessary for hot ductility of polycrystalline materials. Below 700°C the hot ductility begins to recover due to formation of ferrite.
- Hot ductility is severely reduced when P20 steel is undercooled to 800°C - 900°C after solidification then reheated to 1000°C. The undercooling temperatures showing reduced ductility are shifted to lower values for lower aluminum and nitrogen content. No aluminum nitride precipitates were found in the samples, which implies that the austenite grain size and extent of microsegregation at prior austenite grain boundaries as a result of the aluminum and nitrogen content has a significant effect on the precipitation temperature, morphology and volume fraction of the M_7C_3 carbide. This may be due to pinning of the boundaries by MX precipitation during the undercooling step.
- Increased holding time at 900°C undercooling temperature improves hot ductility. The rate of hot ductility recovery is increased for higher aluminum and nitrogen contents. It is possible that when holding at 900°C there is precipitation of fine AlN particles, removing the aluminum and nitrogen from solution and thereby negating the effects of soluble aluminum on the carbon activity, diffusivity and solubility in austenite. Another possibility is that the MX precipitation is occurring during the undercooling step and

these precipitates coarsen during extended hold times until they are no longer effective to pin the grain boundaries at the start of straining.

- Crack formation during the initial forging operations of low-alloy steels is likely propagating from grain boundary separations that occurred in the low ductility temperature regime during ingot cooling or heating to forging temperature. The range of P20 compositions examined in this work did not exhibit poor ductility at forging temperature (>1100°C) when tested directly after cooling from solidification temperatures or after reheating to forging temperature when the undercooling thermal cycle was employed. Therefore, it should be expected that the steel is in a high ductility state when at forging temperature as long as there are no pre-existing conditions such as grain boundary separation in the material.
- AlN should not be expected to precipitate with the HCP crystal structure in austenite during slow cooling after solidification. The volumetric strain term is too large unless the metastable FCC crystal structure or very high aluminum and nitrogen contents are considered.
- The hypothesis of aluminum nitride precipitation on austenite grain boundaries being the cause of hot ductility loss was not supported by the results of this work for the compositions and thermal paths examined.
- The hypothesis of hot ductility tears forming prior to the forging process then propagating to the surface and becoming visible during forging is supported by the results of this work.

10.0 FUTURE WORK

The results of this work raise several interesting questions related to precipitation of aluminum nitride, the effect of deformation on segregation and the effect of aluminum on the as-solidified grain size. It is recommended that the following subjects are studied in greater detail in order to better understand their combined effects on hot ductility of steel:

- The crystal structure of aluminum nitride during the nucleation process in austenite should be investigated. There are several researchers who have suggested nucleation of cubic aluminum nitride in order to reduce the overall Gibb's Free Energy, and cubic aluminum nitride has been identified in previous works. However, there is little information available regarding the details of the crystal structure upon nucleation and the transformation to a hexagonal structure at some later time.
- There is a significant amount of research regarding the segregation of phosphorus, boron and other tramp or interstitial elements to grain boundaries during hot deformation of steel. Conversely there are far fewer data on the segregation of substitutional alloying elements during hot deformation processes. This is an interesting subject with various theories such as uphill diffusion due to variations in the activity coefficients during straining and vacancy-solute complexes in deformation-induced non-equilibrium segregation. A more detailed understanding of this phenomenon for specific cases of

substitutional elements in austenite could allow for predictive methods to estimate local compositions during hot deformation.

- As noted in this work, the effect of aluminum to coarsen the as-solidified structure has been identified in previous research. However, it would be valuable to study the relationship between aluminum content, solidification rate, as-solidified grain size and microsegregation at both the interdendritic regions and grain boundaries. This analysis could also include solidification through the delta ferrite phase field in comparison to solidification as austenite.
- The effect of grain size and composition on precipitation of MX carbonitrides during the undercooling step should be examined in greater detail to examine the pinning effect of different distributions of these particles and the relation to deformation-induced segregation.

BIBLIOGRAPHY

1. M.D. Fenton, "Mineral Resource of the Month: Iron and Steel", *Earth*, American Geosciences Institute, February 2014.

2. T. Revaux, J.P. Bricout and J. Oudin, "A New Tensile Testing Procedure for Predicting Transverse Cracking Susceptibility of Continuous Casting Slabs", *Journal of Materials Engineering and Performance*, April 1996, Vol. 5(2), 260 – 268.

3. W.T. Nachtrab, W.T. and Y.T. Chou, "The Effect of Sn, Al, and N on the Hot Ductility of a Carbon-Manganese Steel between 700˚ and 1200˚C", *Metallurgical Transactions A*, May 1988, Vol. 19A, 1305 – 1309.

4. F. Martin, "Effect of Copper Content on the Hot Ductility Loss of Low Carbon Steels", *Journal of Metals, Materials and Minerals*, 2003, Vol. 12, No. 2, 27 – 31.

5. G.D. Funnelland R.J. Davies, "Effect of aluminum nitride particles on hot ductility of steel", *Metals Technology*, May 1978, 150 – 153.

6. T. Revaux, J.D. Guerin and J.P.Bricout, "Hot Ductility Study of Continuous Casting Steels", *J. Mater. Sci. Technol.*, 2004, Vol. 20, Suppl. 1, 19 – 22.

7. M. Vedani, D. Dellasega and A. Mannuccii,"Characterization of Grain-boundary Precipitates after Hot-ductility Test of Microalloyed Steels", *ISIJ International*, 2009, Vol. 49, No. 3, 446 – 452.

8. T. Kato, Y. Ito, M. Kawamoto, A. Yamanaka and T. Watanabe, "Prevention of Slab Surface Transverse Cracking by Microstructure Control", *ISIJ International*, 2003, Vol. 43, No. 11, 1742 – 1750.

9. D.N. Crowther, "The Effects of Mircoalloying Elements on Cracking During Continuous Casting", *The Use of Vanadium in Steel – Proceedings of the Vanitec Symposium*, Beijing, China, October 2001, 99 – 131.

10. U.H. Lee, T.E. Park, K.S. Son, M.S Kang, Y.M. Won, C.H. Yim, S.K Lee, I. Kim, and D. Kim, "Assessment of Hot Ductility with Various Thermal Histories as an Alternative Method of *in situ* Solidification", *ISIJ International*, 2010, Vol. 50, No. 4, 540 – 545.43.

11. G. Walmag, A. Schmitz and C. Marique, "A new secondary cooling concept for avoiding surface cracks during casting of peritectic and micro-alloyed steels", 4th European Continuous Casting Conference, Birmingham, October 14 – 16, 2002, Vol. 2, 840 – 848.

12. Z. Mohamed, "Hot Ductility of Directly Cast Steels with Different Carbon Contents", *Engineering Journal of University of Qatar*, 1995, Vol. 8, 167 – 181.

13. G.A. Wilber, R. Batra, W.F. Savage and W.J Childs, "The Effects of Thermal History and Composition on the Hot Ductility of Low Carbon Steels", *Metallurgical Transactions A*, September 1975, Vol. 6A, 1727 – 1735.

14. N.H. Croft, "Solubility model to predict effects of aluminum and nitrogen contents on susceptibility of steel castings to intergranular embrittlement", *Metals Technology*, August 1983, Vol. 10, 285 – 290.

15. B. Mintz, R. Abushosha and M. Shaker, "Influence of deformation induced ferrite, grain boundary sliding, and dynamic recrystallisation on hot ductility of 0.1-0.75%C steels", *Materials Science Technology*, October 1993, Vol. 9, 907 – 914.

16. B. Mintz and A. Cowley, "Deformation induced ferrite and its influence on the elevated temperature tensile flow stress-elongation curves of plain C-Mn and Nb containing steels", *Materials Science and Technology*, 2006, Vol. 22, No. 3, 279 – 292.

17. B. Mintz, A. Cowley and R. Abushosha, "Importance of columnar grains in dictating hot ductility of steels", *Materials Science and Technology*, January 2000, Vol. 16, 1 – 5.

18. R.E. Reed-Hill, "Physical Metallurgy Principles", 3rd Edition, *PWS Publishing Company*, Boston, 233 – 893.

19. A. Cowley, R. Abushosha and B. Mintz, "Influence of Ar_3 and Ae_3 temperatures on hot ductility of steels", *Materials Science and Technology*, November 1998, Vol. 14, 1145 – 1153.

20. V.V. Basabe, J.J. Jonas and H. Mahjoubi, "Dynamic Transformation of a Low Carbon Steel at Temperatures above the Ae_3", *ISIJ International*, 2011, Vol. 51, No. 4, 612 – 618.

21. B. Mintz, J. Lewis and J.J. Jonas, "Importance of deformation induced ferrite and factors which control its formation", *Materials Science and Technology*, May 1997, Vol. 13, 379 – 388.

22. R. Radis and E. Kozeschnik, "Kinetics of AlN precipitation in microalloyed steel", *Modelling and Simulation in Materials Science and Engineering*, Vol. 18, 2010.

23. M. Vedani, D. Ripamonti, A. Mannucci and D. Dellasega, "Hot Ductility of Microalloyed Steels", *La Metallurrgia Italiana*, May 2008, 19 – 24.

24. A. Rezaeian, “The Effect of Very High Temperature Deformation on the Hot Ductility of a V-Microalloyed Steel”, *McGill University*, 2008 Doctoral thesis.

25. B. Mintz, “Influence of nitrogen on hot ductility of steels and its relationship to problem of transverse cracking”, *Iron and Steelmaking*, 2000, Vol. 27, No. 5, 343 – 347.

26. R. Harris and L. Barnard, “Experiences of Hot Shortness in the Forging of Certain Low-Alloy Steels” *Publisher information not available*.

27. C. Ernst and B. Wewers, “Influence of residual resulting from scrap use in the electric arc furnace process on the properties of hot-work tool steels”, *Journal of Material Science*, 2004, 39, 637 – 640.

28. A.M. Guo, Y.H. Wang, D.D. Shen, Z.X. Yaun and S.H. Song, “Influence of phosphorus on the hot ductility of 2.25Cr1Mo steel”, *Materials Science and Technology*, November 2003, Vol. 19, 1553 – 1556.

29. L.E. Cepeda, J.M. Rodriguez-Ibabe, J.J. Urcola and M. Fuentes, “Influence of dynamic recrystallisation on hot ductility of aluminum killed mild steel”, *Materials Science and Technology*, December 1989, Vol. 5, 1191 – 1199.

30. J. Calvo, J.M. Carbrera and J.M. Prado, “Fracture mechanisms and ductility at high temperatures of a carbon steel”, *11th International Conference on Fracture*, 2005.

31. S.H. Song, Z.X. Yuan, J. Jia, A.M. Guo and D.D. Shen, “The Role of Tin in the Hot-Ductility Deterioration of a Low-Carbon Steel”, *Metallurgical and Materials Transactions A*, August 2003, Vol. 34A, 1611 –1616.

32. R.P. Messmer and C.L. Briant, “The role of chemical bonding in grain boundary embrittlement”, *Acta Metallurgica*, Vol. 30, 1982, 457 – 467.

33. ICF International 2007 Final Report on “Energy Trends in Selected Manufacturing Sectors: Opportunities and Challenges for Environmentally Preferable Energy Outcomes”, *U.S. Environmental Protection Agency*, March 2007, p. 3-53.

34. W.T. Nachtrab and Y.T. Chou, “High Temperature Ductility Loss in Carbon-Manganese and Niobium-Treated Steels”, *Metallurgical Transactions A*, November 1986, Vol. 17A, 1995 – 2006.

35. J. Pavliska, Z. Jonsta, K. Mazanec and E. Mazancova, “The Metallography Evaluation of the Relationship between the Hot Ductility Shortness and the Susceptibility to Transverse Cracking in CC Products”, *Metal*, 2001, Ostrava, Czech Republic, 15 – 17.5.

36. C.W. Siyasiya, “Effect of sulphur content on the recrystallisation behavior of cold worked low carbon Aluminum-killed strip steels”, *University of Pretoria*, 2007 Doctoral Thesis.

37. L. Backe, “Modeling the Microstructural Evolution during Hot Deformation of Microalloyed Steels”, *Royal Institute of Technology*, 2009 Doctoral Thesis.

38. K.W. Andrews, “Empirical Formulae for the Calculation of Some Transformation Temperatures”, *Journal of the Iron and Steel Institute*, 203, Part 7, July 1965, 721 – 727.

39. J.S. Kirkaldy and E.A. Baganis, “Thermodynamic Prediction of the Ae_3 Temperature of Steels with Additions of Mn, Si, Ni, Cr, Mo, Cu”, *Metallurgical Transactions A*, April 1978, Vol. 9A, 495 – 501.

40. F.J Humphreys and M. Hatherly, “Recrystallization and Related Annealing Phenomena”, Elsevier Science Inc., New York, 1996.

41. B.G. Thomas, J.K. Brimacombe and I.V. Samarasekera, “The Formation of Panel Cracks in Steel Ingots: A State-of-the-Art Review”, *ISS Transactions*, 1986, Vol. 7, 7 – 20.

42. E.T. Turkdogan, “Fundamentals of Steelmaking”, *The Institute of Materials*, London, 1996, 297 – 318.

43. B. Mintz, Z. Mohamed and R. Abu-shosha, “Influence of calcium on hot ductility of steels”, *Materials Science and Technology*, July 1989, Vol. 5, 682 – 688.

44. W. Kim, J. Kang, C. Park, J. Lee and J. Pak, “Thermodynamics of Aluminum, Nitrogen and AlN formation in Liquid Iron”, *ISIJ International*, 2007, Vol. 47, No. 7, 945 – 954.

45. L.M. Cheng, E.B. Hawbolt and T.R. Meadowcroft, “Dissolution and Coarsening of Aluminum Nitride Precipitates in Low Carbon Steel – Distribution, Size and Morphology”, *Canadian Metallurgy Quarterly*, 2000, Vol. 39, No. 1, 73 – 86.

46. M. Hillert and S. Jonsson, “An Assessment of the Al-Fe-N System”, *Metallurgical Transactions A*, November 1992, Vol. 23A, 3141 – 3149.

47. H. Yu, Y.L. Kang, H.B. Dong, D.L. Liu and J. Fu, “Analysis on the behavior of precipitates in ultra-thin hot strip of plain low carbon steel produced by compact strip production”, *Acta Metallurgica Sinica*, August 2002, Vol. 15, No. 4, 375 – 379.

48. F.G. Wilson and T. Gladman, “Aluminum nitride in steel”, *International Materials Reviews*, 1988, Vol. 33, No. 5, 221 – 283.

49. L.S. Darken, R.P. Smith and E.W. Filer, “Solubility of Gaseous Nitrogen in Gamma Iron and the Effect Of Alloying Constituents – Aluminum Nitride Precipitation”, *Journal of Metals*, December 1951, 1174 – 1179.

50. T. Shimose and K. Narita, *Tetsu-to-Hagane* (Journal of the Iron Steel Institute of Japan), 1954, Vol. 40, 242 – 243.

51. W.C. Leslie, R.L. Rickett, C.L. Dotson and C.S. Walton, “Solution and Precipitation of Aluminum Nitride in Relation to the Structure of Low Carbon Steels”, *Transactions of ASM*, 1954, Vol. 46, 1470 – 1499.

52. L.A. Erasmus, “Effect of aluminum additions on forgeability, austenite grain coarsening temperature, and impact properties of steel”, *Journal of the Iron and Steel Institute*, January 1964, 32 – 41. [correspondence from Dec 1964 included].

53. P. Konig, W. Scholz, and H. Ulmer, *Archs Eisenhutt*, 1961, Vol. 32, 541.

54. T. Gladman and F.B. Pickering, *Journal of the Iron and Steel Institute*, 1967, Vol. 205, 653 – 664.

55. K.E. Honer and S. Baliktay, *Proceedings of the 44th International Foundry Congress*, Florence, Sept. 1977, Paper 11, (BISI 26033).

56. H. Ushioda, H.G. Suzuki, H. Komatsu and K. Esaka, “Influence of sulphur on AlN precipitation during cooling after solidification and resulting hot shortness in low carbon steel”, *Nihon Kinzoku Gakkaishi* (Journal of the Japan Institute of Metals), 1995, Vol. 59, No. 4, 373 – 380.

57. O.N. Dogan, “Interactions between austenite grain boundaries and aluminum nitride precipitates”, *Case Western Reserve University*, 1990, doctoral thesis.

58. M. Mayrhofer, *Berg. Huttenmann Monatsh.*, 1975, Vol. 120, No. 7, 312 – 321.

59. T. Gladman, “The effect of aluminum nitride on the grain coarsening behaviour of austenite”, *ISI Special Report*, No. 81, 1963, 68 – 70.

60. M.E. Glicksman and A. Lupulescu, “Diffusion in Solids, Module 9: Spherical Bodies”, *Rensselaer Polytechnic Institute*, course presentation.

61. E.L. Brown, L.J. Cuddy and A.J. DeArdo, "Aluminum Nitride Precipitation in Microalloyed Steels", *The Thermomechanical Processing of Microalloyed Austenite*, A.J. DeArdo, G.A. Ratz and P.J. Wray, Editors, (Warrendale, PA, TMS-AIME: 1982), 319 – 341.

62. F. Limalia, “Comparison of Aluminum Grain Refined and Vanadium Grain Refined Spring Steels for the Manufacture of Highly Stressed Automotive Coil Springs”, *University of Witwatersrand*, 2005 Masters Thesis.

63. B. Mintz and R. Abushosha, “Influence of vanadium on hot ductility of steel”, *Iron and Steelmaking*, 1993, Vol. 20, No. 6, 445 – 452.

64. S. Jiaxiang, Z. Dongliang and W. Chongyu, “The preferred-site tendency of alloying element Nb in Fe γ phase and its effect on grain boundary cohesion”, *Science in China*, February 2002, Vol. 45, No. 1, 90 – 96.

65. C. Spradbery and B. Mintz, “Influence of undercooling thermal cycle on hot ductility of C-Mn-Al-Ti and C-Mn-Al-Nb-Ti steels”, *Iron and Steelmaking*, 2005, Vol. 32, No. 4, 319 – 324.

66. S.F. Medina, L. Rancel, M. Gomex, R. Ishak and M. DeSanctis, “Intragranular Nucleation of Ferrite on Precipitates and Grain Refinement in a Hot Deformed V-microalloyed Steel”, *ISIJ International*, 2008, Vol. 48, No. 11, 1603 – 1608.

67. Z. Yongtao, M. Lede, W. Xiaojun, Z. Hanqian and L. Jinfu, “Evolution Behavior of Carbides in 2.25Cr-1Mo-0.25V Steel”, *Materials Transactions*, Vol. 50, No. 11, 2009, 2507 – 2511.

68. A. Akbarzadeh, S. Naghdy, “Hot Workability of a High Carbon High Chromium Tool Steel”, *Materials and Design*, Vol. 46, 2013, 654 – 659.

69. C. Imbert, N.D. Ryan and H.J. McQueen, “Hot Workability of Three Grades of Tool Steel”, *Metallurgical Transactions A*, Vol. 15A, October 1984, 1855 – 1864.

70. D. Bombac, M. Fazarinc, A. Saha Podder and G Kugler, “Study of Carbide Evolution During Thermo-Mechanical Processing of AISI D2 Tool Steel”, *Journal of Materials Engineering and Performance*, Vol. 22, No. 3, 2013, 742 – 747.

71. N. Angang, G. Hanjie, C. Xichun and W. Mingbo, “Precipitation Behaviors and Strengthening of Carbides in H13 Steel during Annealing”, *Materials Transactions*, Vol. 56, No. 4, 2015, 581 – 586.

72. M. Basirat and H. Fredriksson, “An Insight into the Effect of Deformation on Carbide Dissolution in the Band Structure of Bearing Steel”, *Defect and Diffusion Forum*, Vols. 334 – 335, 2013, 171 – 176.

73. E.J. Pickering and H.K.D.H. Bhadeshia, “Macrosegregation and Microstructural Evolution in a Pressure-Vessel Steel”, *Metallurgical and Materials Transactions A*, Vol. 45, No. 7, 2983 – 2997.

74. J.D. Lee and W.J. Kim, “Compressive behavior capable of predicting hot tensile ductility behavior in a 0.1%C-Mn steel”, *Materials Science and Technology*, April 2001, Vol. 17, 409 – 414.

75. B. Mintz and J.J. Jonas, “Influence of strain rate on production of deformation induced ferrite and hot ductility of steels”, *Materials Science and Technology*, August 1994, Vol. 10, 721 –727.

76. S. Moon, “The Influence Of Austenite Grain Size On Hot Ductility Of Steels”, *University of Woolong*, Department of Materials Engineering, 2003.

77. E. Hurtado-Delgado and R.D. Morales, “Hot Ductility and Fracture Mechanisms of a C-Mn-Nb-Al Steel”, *Metallurgical and Materials Transactions B*, October 2001, Vol. 32B, 919 – 927.

78. L.J. Cuddy and J.C. Raley, “Austenite Coarsening in Microalloyed Steels”, *Metallurgical Transactions A*, October 1983. Volume 14A, 1989 – 1995.

79. N. Gao and T.N. Baker, "Austenite Grain Growth Behaviour of Microalloyed Al-V-N and Al-V-Ti-N steels", *ISIJ International*, 1998, Vol. 38, 744 – 751.

80. F.B. Pickering, "Titanium Nitride Technology", *35th MWSP Conf. Proc*., *ISS-AIME*, Vol. XXXI, 1994, 477 – 491.

81. P. Perrot, "Iron-Nitrogen-Nickel", *MSIT*, Springer Material Database, 2008.

82. F.K. Naumann and F. Spies, "Cast Ingot Cracked During Forging", *Pract. Metall*., 1974.

83. J.I. Komi and L.P. Karjalainen, "Effect of restoration on hot ductility of high alloy and duplex stainless steels", *Materials Science and Technology*, May 2002, Vol. 18, 563 – 570.

84. G.G. Brown and K.G. Wold, "High-Temperature Oxidation of a 0.14%C-3%Ni Steel", *Journal of the Iron and Steel Institute*, November 1969, 1457 – 1462.

85. A. Tremaine, "Characterization of Internal Defects in Open Die Forgings", *Colorado School of Mines Department of Metallurgical and Materials Engineering*, 2005, FIERF Grant Project for Undergraduate Research, 1 – 13.

86. B.G. Thomas, I.V. Samarasekera and J.K. Brimacombe, "Investigation of Panel Crack Formation in Steel Ingots: Part II. Off-center Panel Cracks", *Metallurgical Transactions B*, April 1988, Vol. 19B, 289 – 301.

87. B.G. Thomas, I.V. Samarasekera and J.K. Brimacombe, "Investigation of Panel Crack Formation in Steel Ingots: Part I. Mathematical Analysis and Mid-Face Panel Cracks", *Metallurgical Transactions B*, Vol. 19B, April 1988, 277 – 287.

88. K.E. Blazek, O. Lanzi, P.L. Gano and D.L. Kellogg, "Calculation of the Peritectic Range for Steel Alloys", *AISTech2007 Proc.*, AIST, Indianapolis, 2007, Vol. II, 81 - 87.

89. N.E. Hannerz, "Influence of Cooling Rate and Composition on Intergranular Fracture of Cast Steel", *The Metals and Metallurgy Trust*, 1968, 148 – 152.

90. A. Ghosh, "Segregation in Cast Products", *Sadhana*, February – April 2001, Vol. 26, Parts 1&2, 5 – 24.

91. G. Krauss, "Solidification, Segregation and Banding in Carbon and Alloy Steels", *Iron and Steel Technology*, March, 2004, 145 – 157.

92. R.G. Faulkner, "Non-equilibrium grain-boundary segregation in austenitic alloys", *Journal of Materials Science*, 1981, Vol. 16, 373 – 383.

93. S. Park, K. Lee, M. Kim and B. Lee, "Effects of boundary characteristics on resistance to temper embrittlement and segregation behavior of Ni-Cr-Mo low alloy steel", *Materials Science & Engineering A*, 2013, 277 – 284.

94. Y.J. Li, D. Ponge, P. Choi and D. Raabe, “Segregation of boron at prior austenite grain boundaries in a quenched martensitic steel studied by atom probe tomography”, *Scripta Materialia*, Vol. 96, 2015, 13 – 16.

95. A.J. Papworth and D.B. Williams, “Segregation to Prior Austenite Grain Boundaries in Low-Alloy Steels”, *Scripta Materialia*, Vol. 42, 2000, 1107 – 1112.

96. J. Janovec, V. Magula and P. Sevc, “Some Aspects of Impurity Grain Boundary Segregation in Low Alloy Cr-Mo-V Steels”, *Kovine, zlitine tehnologije*, Vol. 30, No. 6, 1996, 551 – 555.

97. T.P. Battle and R.D. Pehlke, “Equilibrium Partition Coefficients in Iron-Based Alloys”, *Metallurgical Transactions B*, Vol. 20B, April 1989, 149 – 160.

98. R. Sussman, D. Kelley, J. Cordea, “Occurrence and Control of Panel Cracking in Aluminum Containing Steel Heats”, *21st Mechnical Working and Steel Processing Conference*, October 24 – 25 1979, Cleveland, Ohio.

99. C.M. Sellars and W.J. McG. Tegart, “Hot Workability”, *International Metallurgical Reviews*, 1972, Vol. 17, Review 158, 1 – 23.

100. A. Nicholson, “Hot Workability Testing of Steels”, *Iron & Steel*, June - July 1964, 290 – 294, 363 – 380.

101. R. Abushosha, O. Comineli and B. Mintz, “Influence of Ti on hot ductility of C-Mn-Al steels”, *Materials Science and Technology*, March 1999, Vol. 15, 278 – 286.

102. H.F. Beeghly, “Determination of Aluminum Nitride Nitrogen in Steel”, *Analytical Chemistry*, December 1949, Vol. 21, 1513 – 1519.

103. L. M. Rothleutner, “Influence of Reheat Temperature and Holding Time on the Interaction of V, Al and N in Air-cooled Forging Steels”, MS Thesis, Colorado School of Mines, 2012.

104. L. Ericson, “Cracking in Low Alloy Aluminum Grain Refined Steels”, *Scandinavian Journal of Metallurgy*, Vol. 6, 1977, 116 - 124.

105. M. Torkar, “Effect of Trace and Residual Elements on the Hot Brittleness, Hot Shortness and Properties of 0.15 – 0.3% C Al-killed Steels with a Solidification Microstructure”, *Materials and Technology*, Vol. 44, No. 6, 2010, 327 – 333.

106. S. Holmberg, “The Effects of Hot Top Insulation on the Solidification Profile of Large Diameter, Bottom Poured Big End Up Ingots”¸ *Pennsylvania State University*.

107. T. Epicier, D. Acevedo and M. Perez, “Crystallographic structure of vanadium carbide precipitates in a model Fe-C-V steel”, *Philosophical Magazine*, Vol. 88, No. 1, January 2008, 31 – 45.

108. T. Lee, C. Oh, S. Ryu and J. Kim, "Crystallography and Morphology of Carbides in a Low-Cycle Fatigued 1Cr-1Mo-0.25V Steel", *Metallurgical and Materials Transactions A*, Vol. 42A, January 2011, 147 – 157.

109. J.P. Morniroli, M. Khachfi, A. Courtois, M. Gantois, J. Mahy, D. Van Dyck, J. Van Landuyt and S. Amelinckx, "Observations of non-periodic and periodic defect structures in M_7C_3 carbides", *Philosophical Magazine A*, Vol. 56, No. 1, 1987, 93 – 113.

110. B. Kaplan, A. Blomqvist, C. Arhammar, M. Selleby and S. Norgren, "Structural Determination of $(Cr, Co)_7C_3$", *18th Plansee Seminar*.

111. K.W. Andrews, D.J. Dyson and S.R. Keown, "Interpretation of Electron Diffraction Patterns", *Plenum Press*, New York, 1967.

112. L. Cheng, "Study of the kinetics of precipitation, dissolution and coarsening of aluminum nitride in low carbon steels", *University of British Columbia*, April 1999, doctoral thesis.

113. R.J. Bruls, H.T. Hintzen, G. DeWith, R. Metselaar and J.C. Van Miltenburg, "The temperature dependence of the Gruneisen parameters of $MgSiN_2$, AlN and β-Si_3N_4", *Journal of Physics and Chemistry of Solids*, Vol. 62, 2001, 783 – 792.

114. K.C. Russell, "Nucleation in Solids: The Induction and Steady State Effects", *Advances in Colloid and Interface Science*, Vol. 13, 1980, 205 – 318.

115. W.J. Liu and J.J. Jonas, "Characterisation of critical nucleus/matrix interface: application to Cu-Co alloys and microalloyed austenite", *Materials Science and Technology*, January 1989, Vol. 5, 8 – 12.

116. H.S. Zurob, C.R. Hutchinson, Y. Brechet and G. Purdy, "Modeling recrystallization of microalloyed austenite: effect of coupling recovery, precipitation and recrystallization", *Acta Materialia*, 2002, Vol. 50, 3075 – 3092.

117. E. Kozeschnik, "Modeling Solid-State Precipitation", *Momentum Press*, New York, 2013.

118. W.C. Johnson, C.L. White, P.E. Marth, P.K. Ruf, S.M Tuominen, K.D. Wade, K.C. Russell and H.I. Aaronson, "Influence of Crystallography on Aspects of Solid-Solid Nucleation Theory", *Metallurgical Transactions A*, Vol. 6A, April 1975, 911 – 919.

119. P. Maugis and M. Goune, "Kinetics of vanadium carbonitride precipitation in steel: A computer model", *Arcelor Research SA*, May 2005.

120. C. Zener, "Theory of Growth of Spherical Precipitates from Solid Solution", *Journal of Applied Physics*, October 1949, Vol. 20, 950 – 953.

121. M. Perez, M. Dumont and D. Acevedo-Reyes, "Implementation of classical nucleation and growth theories for precipitation", *Acta Materialia*, Vol. 56, 2008, 2119 – 2132.

122. A. Costa e Silva, L. Nakamura and F. Rizzo, “Application of Computational Modeling to the Kinetics of Precipitation of Aluminum Nitride in Steels”, *Journal of Mining and Metallurgy*, Section B: Metallurgy, Vol, 48, 2012, 471 – 476.

123. L.M. Cheng, E.B. Hawbolt and T. R. Meadowcroft, “Modeling of AlN Precipitation in Low Carbon Steels”, *Scripta Materialia*, Vol. 41, No. 6, 673 – 678.

124. F.L. Alcantara, R. Barbosa and M.A. Cunha, “Study of Aluminum Nitride Precipitation in Fe-3%Si Steel”, *Materials Research*, Vol, 16, No. 5, 1039 – 1044.

125. H. Djebaili, H. Zedira, A. Djelloul and A. Boumaza, “Characterization of precipitates in a 7.9Cr-1.65Mo-1.25Si-1.2V steel during tempering”, *Materials Characterization*, Vol. 60, 2009, 946 – 952.

126. Q. Li, I.W. Kim, S.A. Barnett and L.D Marks, “Structures of AlN/VN Superlattices with Different AlN Layer Thicknesses”, *Journal of Material Research*, Vol. 17, No. 5, May 2002, 1224 – 1231.

127. M.I. Hartshorne, C. McCormick, M. Schmidt, et al. “Analysis of a New High-Toughness Ultra-high Strength Martensitic Steel by Transmission Electron Microscopy and Atom Probe Tomography”, *Metallurgical and Materials Transactions A*, Vol. 47, 2016.

128. N.S. Lim, C.W Bang, S. Das, H.W. Jin, R. Ayer and C.G. Park, “Influence of Tempering Temperature on Both the Microstructural Evolution and Elemental Distribution in AISI 4340 Steels”, *Met. Mater. Int.*, Vol. 18, No. 1, 2012, 87 – 94.

129. T. Ando and G. Krauss, “The Effect of Phosphorus Content on Grain Boundary Cementite Formation in AISI 52100 Steel”, *Metallurgical Transactions A*, Vol. 12A, July, 1981, 1283 – 1290.

130. M. Maalekian, “The Effects of Alloying Elements on Steels (I)”, *Christian Doppler Laboratory for Early Stages of Precipitation*, October, 2007.

131. F.M. Wang, X.P. Li, Q.Y. Han, N.X. Zhang, “A Model for Calculating the Interaction Coefficients Between Elements in Liquid and Iron-Base Alloy”, *Metallurgical and Materials Transactions B*, Vol. 28B, February 1997, 109 – 113.

132. Y.J. Li, Q.C. Jiang, Y.G. Zhao and Z.M. He, “Behavior of Aluminum in M2 Steel”, *Scripta Materialia*, Vol. 37, No. 2, 1997, 173 – 177.

133. H. Kakimoto and T. Arikawa, “Prediction of surface crack in hot forging by numerical simulation”, *Procedia Engineering*, Vol. 81, 2014, 474 – 479.